

Nuclear methods for real-time range verification in proton therapy based on prompt gamma-ray imaging

D i s s e r t a t i o n s s c h r i f t

zur Erlangung des akademischen Grades

Doktor der Medizintechnologie

Doctor rerum medicinalium (Dr. rer. medic.)

vorgelegt

der Medizinischen Fakultät Carl Gustav Carus

der Technischen Universität Dresden

von

M. Sc. Fernando Hueso González

aus Valencia

Dresden 2015

1. Gutachter: Prof. Dr. Wolfgang Enhardt

2. Gutachter: Prof. Dr. Magdalena Rafecas

Tag der mündlichen Prüfung: 7. Juni 2016

gez.: Prof. Dr. Mechthild Krause
Vorsitzende der Promotionskommission

Contents

1	Introduction	1
1.1	Proton therapy	1
1.1.1	The beginnings	1
1.1.2	Essential features	2
1.1.3	Advantages and drawbacks	3
1.2	Range uncertainties and their consequences	4
1.3	Range verification methods	6
1.4	Prompt gamma-ray imaging	8
1.4.1	Passive collimation	10
1.4.2	Active collimation	11
1.4.3	Correlation to dose	13
1.5	Aim of this work	13
2	Compton camera	15
2.1	Theoretical background	15
2.1.1	Compton formula and Klein-Nishina cross section	16
2.1.2	Detection principle	20
2.1.3	Intersection of cone surface and plane	20
2.1.4	Practical considerations	24
2.2	Motivation	28
2.3	Goals	30
2.4	Materials	31
2.4.1	Scintillator properties	31
2.4.2	Block detector properties	35
2.4.3	Electronics and data acquisition	39
2.4.4	High efficiency Compton camera setup	40
2.5	Experimental setup	41
2.5.1	Accelerators	41
2.5.2	Detector setup	43
2.5.3	Trigger regime	43
2.6	Methods	45
2.6.1	Energy calibration	45
2.6.2	Spatial calibration	48
2.6.3	Time calibration	49
2.6.4	Error analysis	50
2.6.5	Systematic measurement program	50

Contents

2.7	Results – absorber choice	51
2.7.1	Energy resolution	51
2.7.2	Spatial resolution	53
2.7.3	Time resolution	56
2.8	Discussion – absorber choice	58
2.9	Results – BbCc setup	59
2.10	Discussion – BbCc setup	65
3	Prompt gamma-ray timing	69
3.1	Theoretical background	69
3.1.1	Detection principle	69
3.1.2	Kinematics	69
3.1.3	Detector model	71
3.1.4	Quantitative assessment	74
3.2	Goals	76
3.3	Materials	77
3.3.1	Detectors	77
3.3.2	Electronics	78
3.3.3	Accelerators	78
3.4	Methods	80
3.4.1	Detector and module settings	80
3.4.2	Proton bunch phase stability	80
3.4.3	Proton bunch time structure	81
3.4.4	Systematic measurement program	82
3.4.5	Data acquisition rate	83
3.4.6	Data analysis	83
3.4.7	Modelling of PGT spectra	84
3.5	Results	85
3.5.1	Intrinsic detector time resolution	85
3.5.2	Illustrative energy over time spectra	85
3.5.3	Proton bunch phase stability	87
3.5.4	Proton bunch time structure	88
3.5.5	Systematic measurement program	90
3.6	Discussion	99
3.7	Conclusions	108
4	Discussion	109
4.1	Detector load, event throughput and spot duration	109
4.2	Comparison of PGI systems	113
4.3	Summary	115
4.4	Zusammenfassung	117
	Bibliography	119

List of acronyms and abbreviations

1D	one-dimensional
2D	two-dimensional
3D	three-dimensional
ADC	Analog to Digital Converter
AGOR	Accélérateur Groningen ORsay
BbCc	BGO block Compton camera
BGO	Bismuth Germanium Oxide - $\text{Bi}_4\text{Ge}_3\text{O}_{12}$
BP	Back Projection
C230	Cyclone [®] 230
Cc	Compton camera
CERN	Conseil Européen pour la Recherche Nucléaire
CFD	Constant Fraction Discriminator
CTR	Coincidence Time Resolution
CSDA	Continuous Slowing Down Approximation
ELBE	Electron Linear accelerator for beams with high Brilliance and low Emittance
EPT	Electron-Positron Tracking
FPGA	Field Programmable Gate Array
FWHM	Full Width at Half Maximum
GEVI	Gamma Electron Vertex Imaging
HZDR	Helmholtz-Zentrum Dresden-Rossendorf
KVI-CART	Kernfysisch Versneller Instituut - Center for Advanced Radiation Technology
LLUMC	Loma Linda University Medical Center
LSO	Cerium-doped lutetium oxyorthosilicate - $\text{Lu}_2\text{SiO}_5:\text{Ce}$
MC	Monte Carlo

Contents

MGH	Massachusetts General Hospital
MLEM	Maximum-Likelihood Expectation-Maximisation
MRI	Magnetic Resonance Imaging
NIM	Nuclear Instrumentation Module
NPDF	Normalised Probability Density Function
OAR	Organ At Risk
PA	Preamplifier
PBS	Pencil Beam Scanning
PET	Positron Emission Tomography
PGI	Prompt Gamma-ray Imaging
PGT	Prompt Gamma-ray Timing
PMMA	Polymethyl Methacrylate - $[C_5O_2H_8]_n$
PMT	Photomultiplier Tube
QDC	Charge to Digital Converter
RF	Radio Frequency
SDEP	Single and Double Escape Peaks
simBox	simple Box
SOBP	Spread Out Bragg Peak
TDC	Time to Digital Converter
UFH	University of Florida Health Proton Therapy Institute
USA	United States of America
UPTD	Universitäts Protonen Therapie Dresden
VME	VERSAmodule Eurocard
WPE	Westdeutsches Protonentherapiezentrum Essen

1 Introduction

1.1 Proton therapy

1.1.1 The beginnings

In the first decades of the 20th century, during the rise of particle accelerators, physicists studied the interaction of fast charged particles with matter. The energy loss of *heavy* ions (as opposed to *light* electrons) within a target medium was described by Bethe's stopping power formula (Bethe, 1930). The ionisation, namely the Coulomb collisions (inelastic electromagnetic interactions) where the accelerated ions strip out electrons of the atoms of the target, is the predominant stopping mechanism for non-relativistic ion beams (Newhauser and Zhang, 2015).

The engineering race towards high energy accelerators endowed heavy charged particles a penetration depth in tissue comparable to the body dimensions. This opened up the possibility of using protons for medical applications, as neutrons, electrons, γ -rays or X-rays had been applied before in the field of radiotherapy, which emerged after Röntgen's discovery in 1895 (Röntgen, 1896).

In 1946, Wilson predicted the physical, in particular, dosimetric properties of a proton beam (Wilson, 1946) for a therapeutic scenario and founded the field of proton therapy. The straight beam trajectory, the finite particle range as well as the increase of the ionisation density close to the stopping point aroused the interest of the medical community. In the context of cancer treatment, this ionising radiation was expected to damage the cells of the target tumour and eventually cause their death, while sparing efficiently surrounding normal tissue.

The first patient treatments were performed during the 1950s at Berkeley Radiation Laboratory, United States of America (USA), and in Uppsala, Sweden (PTCOG, 2014; Newhauser and Zhang, 2015). However, it was not until 1990 that the first hospital-based proton facility in Loma Linda University, USA, was created. Since then, the number of therapy centers has increased steadily (Jermann, 2015), and carbon or other ions have been also introduced. Nowadays, 15 000 patients are treated per year in around 50 facilities worldwide (Jermann, 2015); 87 % with protons, 11 % with carbon ions and 2 % with other ions.

It should be emphasised that most cancers are treated successfully with surgery, electron or photon therapy, gamma knife, chemotherapy, brachytherapy, whereas ion beam therapy

1 Introduction

covers just a residual percentage (below 1 %). Still, the improvement in the accelerator technology, delivery systems, and the trend towards personalised medicine make proton beams an attractive alternative for certain patient ages and types of tumours. It is estimated that $\sim 10\%$ of cancer patients, particularly children, would benefit from proton therapy (reduction of late side effects) compared to conventional techniques (Amaldi and Kraft, 2005). Hence, proton therapy is still in the headlines, the number of facilities is increasing from year to year, and several questions arise concerning clinical evidence, improvement of the technique and quality assurance. The current dissertation fits in this context and investigates various methods for monitoring the dose delivery of proton beams in real-time.

1.1.2 Essential features

Several distinguishing features of accelerated charged particles such as protons, helium or carbon ions are listed below.

- *The particle range*: the ions stop at a defined penetration depth, which depends on their initial velocity and the traversed material.
- *Range straggling*: there are statistical fluctuations in the energy loss process, so that the stopping point distribution is not perfectly sharp.
- *The Bragg peak*: the ionisation cross section increases for low ion velocities, so that the dose deposition density is maximum close to the particle range (Newhauser and Zhang, 2015). Conversely, the dose at the entrance point is minimum.
- *The distal penumbra*: beyond the particle range, the dose deposition falls steeply to zero for protons. For heavier ions, the fragmentation process leads to lighter charged particles with a longer range (Bethe, 1930), which results in a moderate dose tail beyond the range of the primary ions (Schardt et al., 2010).
- *The lateral penumbra*: the beam trajectory is straight, but there is a spread in the transversal dimension due to multiple Coulomb scattering (elastic collisions on target nuclei). This spread is small, specially for the heavier nuclei, but increases steadily with the penetration depth (Fiedler, 2008, p. 15), (Abril et al., 2015, fig. 1).
- *The relative biological effectiveness*: heavy ions like carbons have a significantly higher radiation effect than photons. For protons, the relative effectiveness is just ~ 1.1 (Paganetti, 2014).
- *Tissue composition*: the dose deposition curve and ion range is strongly dependent on the stopping power of the traversed tissue (on its density and composition).
- *Secondary products*: neutrons, annihilation photons, prompt γ -rays and charged fragments are produced throughout the ion track. The respective yield depends on the accelerated ion type. These secondary by-products release a small dose compared to the incident ions (Newhauser and Zhang, 2015), and they can exit the patient. The

emission of charged fragments and neutrons is focused in forward direction (Robert et al., 2013).

At present, accepted indications for treatment with protons or other ions are restricted to certain stages and types of cancers like head and neck malignancies, chordoma and chondrosarcoma, ocular tumours as well as paediatric primary tumours (Testa, 2010; ASTRO, 2014), where there is clinical evidence of less late side effects.

1.1.3 Advantages and drawbacks

In principle, ion beam therapy has several advantages over conventional photon therapy:

- *The distal edge*: the steep dose gradient at the stopping point is promising for sparing critical organs close to the irradiated tumour. In contrast, the slowly falling depth-dose curve of photons impedes that strategy.
- *The integral dose*: thanks to the Bragg peak, the dose can be focused on the tumour volume and the damage on normal tissue before and beyond is minimised. For photons, the dose in healthy tissue can only be distributed on a larger volume by irradiating from several directions, but its integral is higher than for protons.
- *The relative biological effectiveness*: heavy ions are especially indicated for radio-resistant or paediatric tumours (Schardt et al., 2010).

The main drawbacks compared to photons are:

- The large capital expenditure on the facility construction and the much higher clinical operating costs (Goitein and Jermann, 2003; Peeters et al., 2010).
- The lack of large clinical trials and evidence about the superiority of ion beam therapy for the majority of tumour entities (Freeman, 2015). Does the lower integral dose translate to better clinical outcome (Freeman, 2012), e.g. less normal tissue toxicity?
- Range uncertainties of the ion beam (Deasy, 1994). Intrinsic factors like patient or organ motion, as well as restricted knowledge about the tissue composition, are prone to yield severe differences with respect to the planned dose, specially at the distal edge. Instead, photon plans are much less sensitive in this regard, cf. fig. 1.1. To circumvent the risk, safety margins are applied and robust treatment plans are designed, at the price of an increase of the dose in the normal tissue compared to the dose-optimum (but more risky) plan.

These disadvantages cast doubts on the cost effectiveness of ion beam therapy and fuel the controversy about the clinical superiority (Orton and Hendee, 2008, chapters 2.11-2.13), (Bekelman and Hahn, 2014; Mitin and Zietman, 2014) over photon therapy.

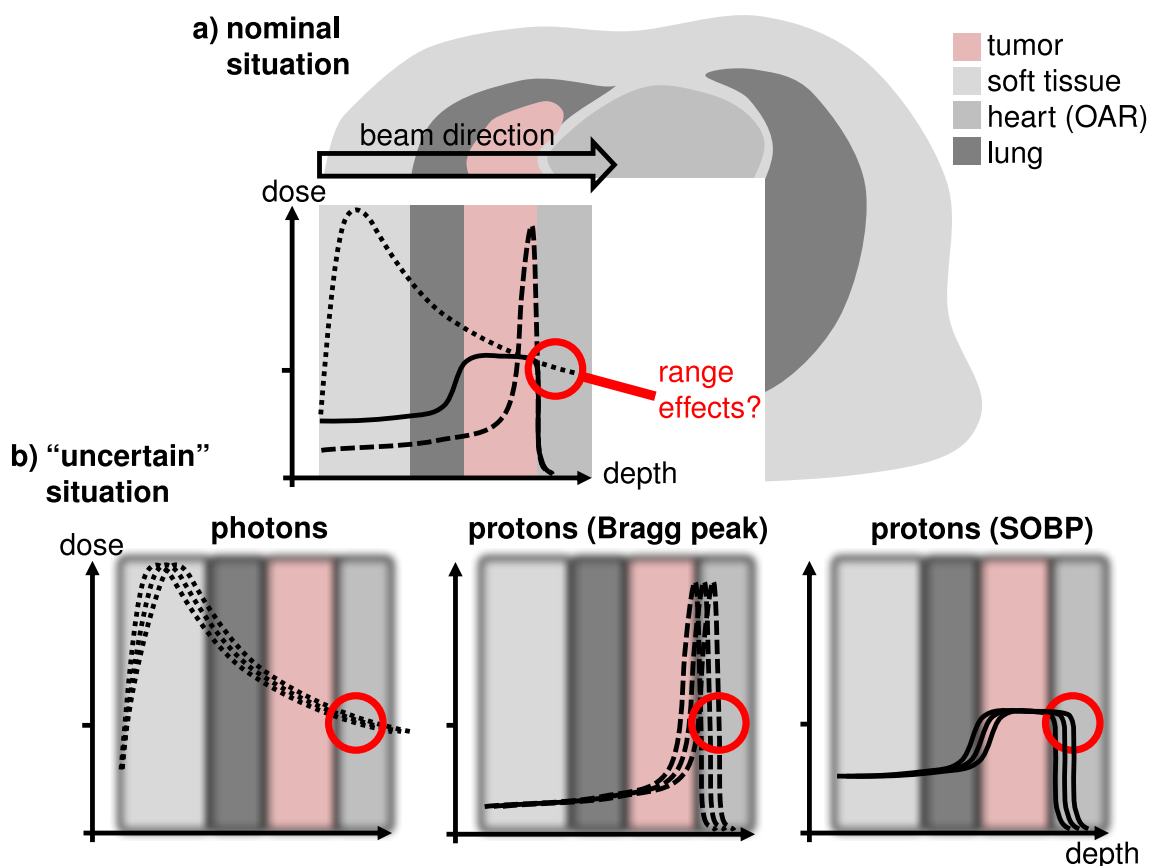


Figure 1.1: Schematic comparison of photon and proton treatment plans. (a) Ideal case, which shows the potential dose benefit of a proton treatment compared to a photon treatment. Dotted line: photon depth-dose curve; dashed line: monoenergetic proton dose profile, exhibiting the Bragg peak; solid line: combination of different proton energies to form a Spread Out Bragg Peak (SOBP) in order to cover the whole tumour. (b) Influence of range uncertainties to the respective depth-dose curves. Reproduced with permission from (Knopf and Lomax, 2013).

1.2 Range uncertainties and their consequences

There is an imperative need for techniques that tackle one of the major weaknesses of ion beam therapy: the range uncertainties, which limit the precision with which particle beams can be safely delivered. What are the common sources of range (and dosimetry) errors?

- Stopping power ambiguity due to degeneracy of Hounsfield values depending on tissue composition (Andreo, 2009).
- Patient misalignment.
- Anatomy changes between or during treatment fractions, as cavity filling, change of weight, tissue swelling or tumour shrinkage.
- Organ motion in the thoracic and abdominal region.
- Biological factors affecting the effective dose in tissue (Grün et al., 2013).

Why are these factors much more important in ion beam therapy than in conventional radiotherapy? The ion range, close to which the ionisation density is maximum, is strongly dependent on the composition of the traversed tissue. The dose distribution of photons is less dependent on these factors and the absence of a sharp edge constrains the maximum dose deviations due to target shifts or path composition variations.

Hence, the distal edge of ions is a double-edged sword: if they mislead the target, they can be more harmful than helpful. As treatment plan calculations are affected by these inherent and mostly unavoidable uncertainties, in vivo measurements seem the most promising workaround to detect and balance them, and improve the accuracy of the irradiation.

Safety margins Nowadays, the absence of tools in clinical routine for measuring in vivo and in real-time the actual distal fall-off edge, together with the high sensitivity of the ion range to tissue composition, force medical physicists to add safety margins and apply field patching techniques in order to obtain a robust treatment plan (Albertini et al., 2011).

Safety margins represent an increase of the prescribed ion range for ensuring a full target coverage even in the case of an *undershoot* (range smaller than prescribed). Field patching refers to the substitution of a single irradiation field stopping in front of an Organ At Risk (OAR) with several lateral fields, so that a potential *overshoot* (range larger than prescribed) does not reach the critical structure in any case. This increases the overall treatment duration. In other words, one favours a smooth lateral penumbra to the detriment of a sharper but much too risky distal fall-off (Lu, 2008). Often, shorter path lengths through normal tissues are avoided because of the lack of confidence about the outcome (Knopf and Lomax, 2013), at the price of a higher dose to normal tissue, cf. fig. 1.2.

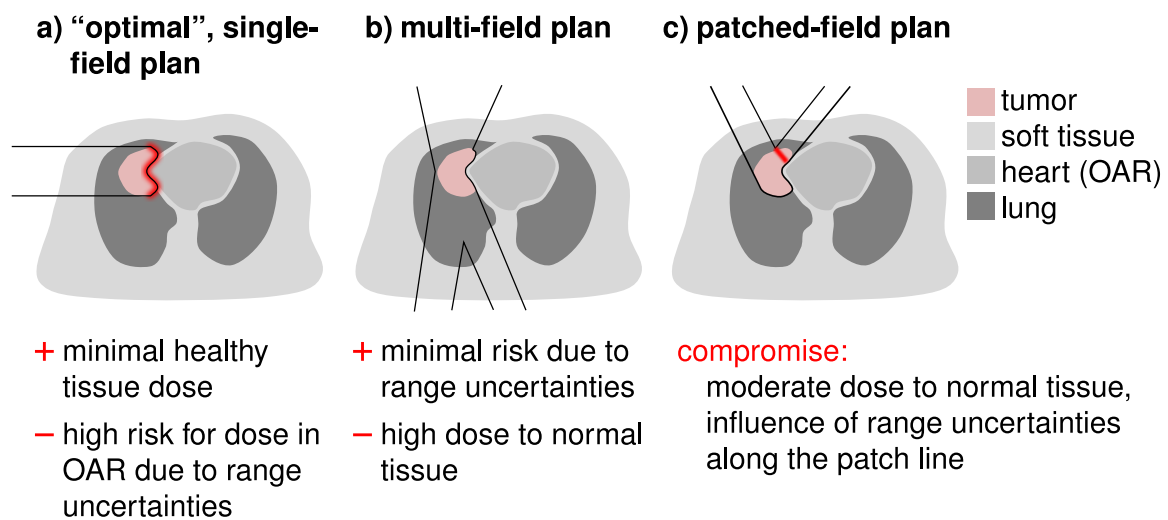


Figure 1.2: In order to avoid the risk of stopping in front of an OAR with a proton beam (a), different strategies like a multi-field plan (b) or field patching (c) are applied. The respective potential sensitivity towards range uncertainties is summarised. Reproduced with permission from (Knopf and Lomax, 2013).

Notwithstanding the theoretically superior dose profile of ions, broad safety margins and field patching waste substantially the outstanding traits of ion over photon beam therapy. An experimental apparatus that measures the range with two millimetre accuracy in real-time could challenge the clinically applied safety margins (fig. 1.3) and counteract most sources of range uncertainties. Thus, more accurate and still safe treatment plans could be designed and verified. Whether or not this improvement would translate into clinical gain and lead to higher evidence of superiority over radiotherapy with photons is still a speculation.

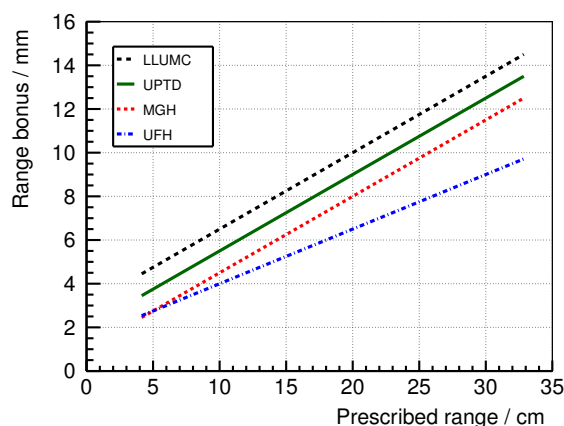


Figure 1.3: Safety margins applied at different clinical proton therapy facilities: (3.5% + 3 mm) at Loma Linda University Medical Center (LLUMC), (3.5% + 2 mm) at Universitäts Protonen Therapie Dresden (UPTD), (3.5% + 1 mm) at Massachusetts General Hospital (MGH) and (2.5% + 1.5 mm) at University of Florida Health Proton Therapy Institute (UFH). *Range bonus* refers to the margin added to the prescribed range to ensure full tumour coverage even in the case of an under-shoot. These centres may apply bigger margins in specific treatment scenarios (Paganetti, 2012).

1.3 Range verification methods

In this context, several groups across the world race towards an experimental device that measures the particle range and even the dose profile, preferably in real-time (Knopf and Lomax, 2013; Kraan, 2015). Numerous techniques have been proposed in the last two decades. Few of them have been implemented in individual clinical treatments, many others are still in research phase.

Why are the already existing methods not yet applied in clinical routine widespread? Each of them has some advantages and weaknesses, and no ultimate or combined solution is yet commercially available. Rather, different methods are expected to be useful according to the ion type or even cancer location. The available methods reviewed in (Smeets, 2012; Knopf and Lomax, 2013) are summarised below.

- *Diode arrays*: it is a direct but invasive measurement method. By implanting a limited number of micro dosimeters with wireless readout in the treated area, one can verify

in real-time if the beam is delivered as planned (Lu et al., 2010). The main concern is the limitation of this technique to few cancer locations where such markers can be implanted.

- *Beam probe*: it requires the irradiation with a short but very energetic proton beam that crosses the patient (Mumot et al., 2010). By comparing expected and measured residual range, patient misalignment or anatomy changes can be detected indirectly. Nevertheless, the maximum range provided by current clinical accelerators may not be sufficient in some cases to cross the patient.
- *Positron Emission Tomography (PET)*: positron emitting isotopes are generated in nuclear interactions between the accelerated particles and nuclei of the tissue. The activity can be reconstructed with conventional PET scanners after the treatment and compared with the expected one (Parodi et al., 2002). It is one of the most promising approaches and has been implemented in several clinical treatments, but a quantitative dosimetry seems not feasible. Online PET scanning during treatment delivery is technically challenging, whereas offline scanning degrades the original distribution due to metabolic washout (long half life of isotopes) and slows down slightly the clinical workflow.
- *Magnetic Resonance Imaging (MRI)*: the effect of the irradiation on the tissue can be analysed thanks to the high spatial resolution of MRI scans after the treatment (Gensheimer et al., 2010). However, the particle range can only be inferred indirectly and a posteriori, and suffers from large uncertainties.
- *Ionoacoustics*: by detecting with a high frequency transducer the thermoacoustic signals produced as a by-product of the ion energy deposition, one can recover the Bragg peak position of a single pencil beam with high accuracy (Assmann et al., 2015). This approach seems promising for tumour locations for which ultrasound imaging is feasible. On the other side, it is questionable or needs still to be explored if the concept is also applicable to heterogeneous tissue.
- *Interaction vertex imaging*: in the case of carbon therapy, nuclear interactions can originate secondary charged fragments like protons, which may have enough energy to exit the patient. The measurement of the spatial emission and angular distribution of these fragments can provide information about the particle range (Henriquet et al., 2012). This approach is however not applicable for proton therapy.
- *Bremsstrahlung imaging*: for carbon ions, secondary electrons produce a significant amount of bremsstrahlung photons, which can be correlated to the particle range (Yamaguchi et al., 2012). However, this method seems not feasible for deep-seated tumours due to photon attenuation and its applicability to protons is not yet proven.
- *Prompt Gamma-ray Imaging (PGI)*: γ -rays are emitted promptly by nuclei of the tissue excited by the incident projectile. The emission distribution is correlated to the dose

deposition, especially for protons (Smeets, 2012, fig. 1.9), provided that the proton, γ -ray energy and target composition are known. This inherently real-time measurement concept faces technical challenges due to high γ -ray rates (detector load and data acquisition throughput), neutron background, polychromatic energy spectrum and high γ -ray energies. Several PGI solutions based on active as well as passive collimation have been proposed and some camera prototypes are on the way to clinical translation.

Other complementary methods try to reduce the sources of uncertainties. For example, a proton radiography or dual-energy X-ray tomography is expected to provide a more accurate map of the patient stopping power, on which the treatment plan relies. The tracking, gating and repainting techniques intend to compensate for organ motion within a treatment fraction, which is critical for irradiating lung or abdominal tumours.

1.4 Prompt gamma-ray imaging

Prompt γ -rays, a by-product emitted in nuclear reactions along the ion track, cf. fig. 1.4, are a very active research subject in the field of range verification. Their energy spectrum covers high energies and shows a quasi-continuous distribution as well as prominent characteristic lines, cf. fig. 1.5 (left). The high γ -ray energy ensures that they can be detected outside the patient without severe attenuation. The spatial emission distribution correlates to the dose deposition map of the incident ions (Min et al., 2006), cf. fig. 1.5 (right), and provides an indirect measurement of the particle range. Such correlation is dependent on prompt γ -ray energy and tissue composition (Moteabbed et al., 2011; Gueth et al., 2013; Polf et al., 2013; Janssen et al., 2014), and stems from the maximum of the nuclear cross section at low (~ 10 MeV) proton energies (Kozlovsky et al., 2002).

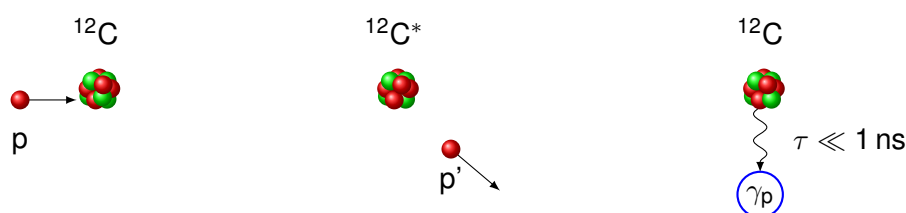


Figure 1.4: Schematic of a typical prompt γ -ray production process $^{12}\text{C}(p,p')^{12}\text{C}^*$ (Kozlovsky et al., 2002). Left: nuclear collision of a proton (p) with a ^{12}C nucleus of the target. Center: the proton is scattered (p') and the nucleus is left in an excited state $^{12}\text{C}^*$. Right: the relaxation to the ground state ^{12}C is accompanied by a 4.4 MeV prompt γ -ray emission γ_p .

These γ -rays are *prompt*, i.e. they are emitted almost instantaneously after the collision. The decay time of most excited nuclei is far below 1 ns (Kozlovsky et al., 2002). This implies that the detection is only possible during the treatment. Hence, this method does not suffer from the metabolic washout effect of offline PET.

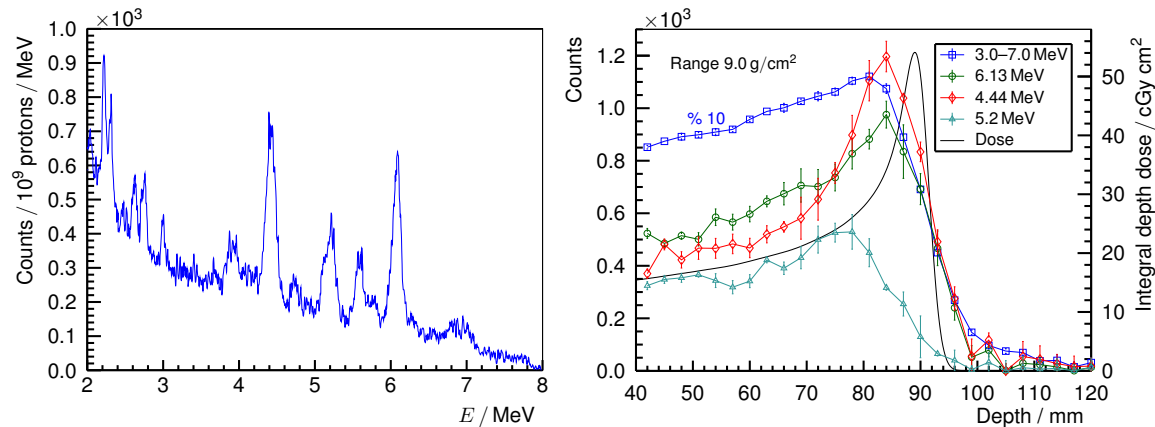


Figure 1.5: Left: energy spectrum of the prompt γ -rays emitted by a proton pencil beam irradiating water (9.0 g/cm^2 range), measured with a LaBr_3 detector and a slit collimator (facing the Bragg peak). Right: measurement of the prompt γ -ray emission with a slit collimator and comparison to the delivered dose profile along the path of a proton pencil beam in water. Different characteristic γ -ray lines are selected. Both: graphs are extracted from (Verburg et al., 2013).

On the other hand, the average γ -ray production is considerable, around one prompt γ -ray per ten protons (Smeets, 2012). The γ -ray emission rate depends on the beam current, duty cycle and micro time structure of the considered accelerator. Taking as an example the Cyclone[®] 230 (C230) isochronous cyclotron of IBA (Louvain-la-Neuve, Belgium), during beam delivery, the typical beam current is $\approx 2 \text{ nA}$, there are about 10^9 γ -ray emissions per second, and 10^6 events are registered per second in a $\varnothing 2'' \times 2''$ LaBr_3 scintillator at 30 cm distance (Hueso González et al., 2015b). This large γ -ray rate, as well as the inherent neutron background, pose a serious challenge on the detector and electronics design. Note that the so called neutron background is mainly indirect, due to the detection of γ -rays following neutron interactions or neutron captures in surrounding materials, rather than from the interactions of neutrons in the detector itself.

In the field of nuclear medicine, commercial gamma cameras are used in clinical routine to obtain images of γ -ray distributions. Hence, one may think that the imaging of prompt γ -rays is not an issue, since the technology is already established. Where are then the difficulties? Together with the detection rate and background, the high γ -ray energies and polychromatic energy spectrum (up to 8 MeV with pronounced characteristic lines at 4.4 and 6.1 MeV) prevent the direct use of the gamma camera as PGI device. In comparison, the γ -ray energies in nuclear medicine range between 80 and 511 keV. This significant difference is outlined in fig. 1.6: larger collimators and detectors are needed to absorb high energy prompt γ -rays, normally after multiple interaction processes. For example, a 2 mm layer of lead has a 99% attenuation power for 140 keV photons, but only 9% for 4.4 MeV γ -rays; a 1 cm thick CsI crystal has a detection efficiency of 98% for the first, and just 15% for the latter. Thick collimators reduce the system efficiency and deteriorate the image quality, whereas large detectors increase critically the system price and enlarge the footprint. Hence, alternative concepts are needed: dedicated PGI detector systems have been designed and tested

during the last decade based on passive or active collimation.

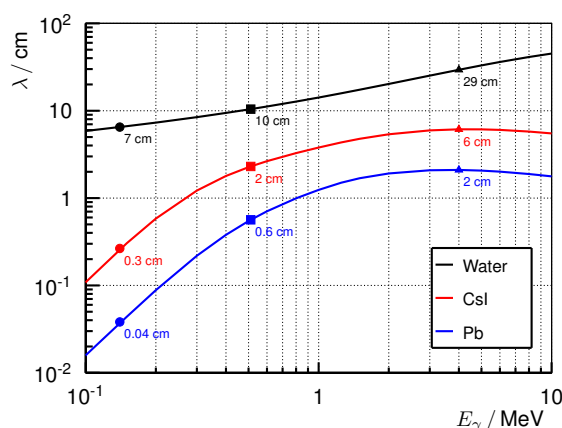


Figure 1.6: Mean free path λ of photons of energy E_γ in different representative materials: water (body), CsI (detector) and Pb (collimator). λ is calculated as the inverse of the total attenuation factor μ , that is extracted from (Hubbell and Seltzer, 2004). Explicit points at three typical energies are drawn: 140 keV for ^{99}Tc (nuclear medicine), 511 keV for PET and 4 MeV for PGI.

1.4.1 Passive collimation

A pinhole camera (Seo et al., 2006), namely a detector enclosed in a thick shielding block with a narrow hole, is the pioneer approach to scan the prompt γ -ray emission distribution in a right angle to the beam track. The measured distributions are sensitive to 1 mm variations of the proton range (Kim et al., 2009), but the low statistics collected in the clinical scenario limit this approach.

The slit camera is based on the extension of the pin-hole to a straight slit perpendicular to the ion track for increasing the sensitivity, at the price of having one-dimensional (1D) profiles instead of two-dimensional (2D) images. Various research groups have performed experiments at proton or carbon beams (Testa et al., 2008). An established design variant uses a knife-edge shape of the aperture (Smeets et al., 2012), that has demonstrated the feasibility of millimetre range verification at clinical current intensities (Perali et al., 2014) in real-time and spot by spot with realistic treatment plans and heterogeneous phantoms (Priegnitz et al., 2015). The energy spectroscopy approach with a slit collimator and a single detector (Verburg and Seco, 2014; Verburg et al., 2015) as well as the prompt γ -ray time pattern method for passively scattered beams (Testa et al., 2014) seem also promising.

The multi-hole (Lee et al., 2012), multi-parallel slit (Pinto et al., 2014) or multi-slat (Cambracia Lopes et al., 2012) concepts are also appropriate candidates for PGI clinical systems. The main advantage is the increased field of view and sensitivity, which allows the imaging of the whole ion path and not just the distal edge.

1.4.2 Active collimation

Electronic or active collimation refers to the recovery of the incidence angle of photons without a mechanical collimator shield. For example, in PET scanners, the *electronic* condition of coincident detection of the two back-to-back annihilation decodes implicitly the incidence direction of each 511 keV photon, namely the virtual line connecting the two opposite detectors of the PET ring that registered this coincidence (in time and energy). In contrast, for passive collimation, the directional information is gained by blocking photons that are not parallel to the hole or slit (do not cross the aperture).

In the PGI scenario, with single γ -rays instead of back-to-back photons, the Gamma Electron Vertex Imaging (GEVI) method, the Electron-Positron Tracking (EPT) or the Compton camera (Cc) may also recover partially the directionality without the need of a passive collimator, and can monitor the whole ion track and not only the distal edge. These approaches reduce the device footprint, which is important for clinical integration, maximise the sensitivity, uniformity and field of view (as no γ -rays are blocked), and minimise the generation of other secondary γ -rays close to the patient due to neutron capture in the collimator shielding. The price to pay is a more complex image reconstruction, higher detector requirements and much higher electronics expense compared to the passive approach.

The GEVI method is based on the incoherent scattering of γ -rays with a scatterer foil. The trajectory of the Compton electron is tracked, and a calorimeter is used to measure its energy. Despite the fact that incoherent scattering implies a change of direction (and energy), one assumes for simplicity that the scattered electron is collinear to the original γ -ray. This approximation is motivated by the forward-peaked probability distribution of the velocity of the electrons, especially for high energy incident photons. Simulations predict a sub-centimetre precision for several proton energies in homogeneous phantoms (Kim et al., 2012).

The EPT concept relies on the pair production process of high energy γ -rays. An electron-positron pair is created due to the interaction of the γ -ray with the electric field of a nucleus. A pair production camera comprises a thin detector layer, where the pair is created, and a thicker one, where the leptons are absorbed. The measurement of the trajectory and energy of these leptons can be used to reconstruct the incidence direction of the prompt γ -ray. In practice, the low efficiency and insufficient angular resolution are major drawbacks at the PGI energy range (Rohling, 2015, section 4.3). In fact, pair production cameras were designed in the field of astronomy, where the γ -ray energy is over 30 MeV, in contrast to few MeV in the case of PGI. The smaller the γ -ray energy, the lower the pair production cross section and the larger the angle between electron and positron propagation directions. Due to multiple scattering and restricted solid angle, not all electron-positron pairs produced in the first layer reach the absorber. Also, the positrons stopped in the absorber produce two annihilation photons (511 keV each), which may escape the layer with moderate probability. Anyway, the efficiency and angular resolution are affected by the camera granularity, size and geometry rather than by the uncertainty on the kinetic energy of the leptons. Only for

1 Introduction

γ -ray energies over 8 MeV, the pair production camera provides a significant number of valid events with respect to a Cc (Rohling, 2015, fig. 4.24).

The Cc (Everett et al., 1977) comprises multiple position sensitive γ -ray detectors arranged in one scatterer and one absorber, or in several scatterer planes. The energy deposited by the prompt γ -rays in each plane as well as the point of interaction are measured. Based on the well-known Compton formula (Compton, 1923), an iterative imaging algorithm reconstructs the prompt γ -ray emission density map. In contrast to a slit camera, no collimation is needed in order to reconstruct the incidence direction of the γ -ray, and 2D or even three-dimensional (3D) images instead of 1D profiles may be obtained. More single γ -rays and incidence directions can be detected.

On the other hand, the condition of simultaneous interaction in the different camera stages limits the overall efficiency. In addition, the instrumentation requirements in terms of spatial, time and energy resolution for the detectors of a Cc are especially high. And the reconstruction algorithm is complex and computationally intensive, as the incident direction cannot be recovered univocally for each event. Nowadays, a PGI Cc prototype demonstrating range verification in a clinical scenario is still a challenge several institutes aim at (Kormoll et al., 2011; Seo et al., 2011; Llosá et al., 2013; Krimmer et al., 2015; Thirolf et al., 2014; McCleskey et al., 2015), and the only published experimental results at a proton beam are constrained to < 2 MeV γ -rays (Kabuki et al., 2009; Kurosawa et al., 2012) or to low proton beam currents (Polf et al., 2015). Technical complexity, electronic expense, low coincident efficiency, high γ -ray flux (detector load), radiation background and the elevated percentage of random coincidences are intrinsic hurdles that cast doubts on the applicability of this concept (Smeets, 2012).

In the recent years, one can identify a trend towards less complicated PGI systems, at least concerning hardware. They may have a faster translation into clinical practice due to their lower price (Testa et al., 2014; Verburg and Seco, 2014; Assmann et al., 2015). The Prompt Gamma-ray Timing (PGT) method (Golnik et al., 2014) is one among them, which relies on a single monolithic detector with excellent timing resolution and no collimation. As a consequence of the measurable transit time of ions through matter, the detection times of prompt γ -rays encode essential information about the spatial emission profile. Its low cost and small footprint make this concept very tempting. A major limitation is that the time spectra are blurred not only by the resolution of the detector, but also by the time width of the accelerated bunches. This implies that the PGT method is not applicable at all clinical accelerators, but only at those with a specific micro time structure. For the widespread accelerator C230 (PTCOG, 2014), the micro bunch time spread can reach up to 2 ns for clinical beam energies (Hueso González et al., 2015b). Here, range shifts can be identified based on distribution momenta. It is under exploration whether PGT is only applicable to pencil beams or also to passively scattered ones. In order to know if other types of clinical accelerators are compatible with the PGT approach, the specific micro pulse structure has to be measured.

1.4.3 Correlation to dose

It should be emphasised that, even with ideal detectors and gamma cameras, the correlation of prompt γ -ray emission distribution to particle range or dose profile is not a trivial task, as it depends on the knowledge about:

- The tissue composition.
- The prompt γ -ray yield for each tissue and characteristic line (Verburg and Seco, 2014).
- The attenuation of γ -rays inside the target.
- The emission anisotropy (Shute and Baxter, 1966, p. 8). This is not yet reliably modelled in Monte Carlo (MC) simulations (Styczynski, 2009, p. 36) and the validation measurements are scarce or have large error bars (Lee et al., 2014; Mattei et al., 2015).

Whereas the correlation has been shown experimentally in controlled environments and predefined target configurations (Min et al., 2006), it remains an open question if PGI will ever be able to provide a quantitative and precise dosimetry (one of the main claims over PET imaging) in a clinical scenario, where the patient composition is not perfectly known and may vary between treatment fractions (Janssen et al., 2014).

1.5 Aim of this work

This dissertation focuses on one of the major weaknesses of ion beam therapy: the range uncertainties. They force the application of conservative safety margins and prevent taking full profit from the outstanding ion depth-dose profile. As most sources of these uncertainties cannot be eliminated, methods are designed to monitor the treatment delivery in real-time, account for potential deviations and challenge the current safety margins. In principle, a range verification device could improve the accuracy of the treatment plan and, presumably, the clinical outcome of the therapy concerning late side effects.

PGI is one monitoring technique, among others enumerated in this chapter, providing an indirect measurement of the particle range. Prompt γ -rays are adequate signatures produced in a high amount, in real-time (no washout effect), correlated to the dose and which exit the patient, so that even a quantitative in vivo dosimetry might be feasible. Specifically, this thesis concentrates on two PGI methods of the active collimation branch: the Cc and the PGT.

The theoretical background, experimental detector characterisation and tests at clinical proton beams with phantoms are reviewed in both cases (in separate chapters). The goal of the work is to prove or question the feasibility at all of these methods in a clinical scenario; or

1 Introduction

what steps need to be addressed towards it, rather than providing already applicable prototypes. Both approaches are compared then in the discussion chapter in terms of precision, efficiency and cost.

Focus is on experimental characterisation and results as well as simple reconstruction analysis and models, whereas the needful comparison with MC simulations or the use of sophisticated reconstruction algorithms exceed the scope of this dissertation.

2 Compton camera

2.1 Theoretical background

The three main interaction mechanisms of a photon of energy E_γ with matter (a detector with atomic number Z , mass number A and density ρ) are:

- Photoelectric absorption: the photon is completely absorbed by an inner shell electron, that is then ejected from the atom. Its kinetic energy equals the γ -ray energy minus the electron binding energy. This missing energy (several up to hundred keV) is released as characteristic X-rays. For large detectors, they are absorbed locally, so that the *photopeak* E_γ is visible. For thin detectors, an X-ray with energy E_X , usually stemming from the K shell, may not be absorbed and lead to the X-ray escape peak ($E_\gamma - E_X$). The photoelectric effect dominates at low photon energies (under 100 keV), cf. fig. 2.1, and the attenuation coefficient τ depends on $\rho \frac{Z^{4.6}}{A} \frac{1}{E_\gamma^3}$ (Krieger, 1998, chapter 4).
- Incoherent (Compton) scattering: the photon interacts with an electron. As a result, the photon changes its direction of propagation by an angle θ and transfers part of its energy to the recoiling electron. The electron is usually stopped inside the detector, and a continuous distribution left from the photopeak is visible in the energy spectrum, cf. fig. 2.5. This process dominates at medium photon energies (about 1 MeV), cf. fig. 2.1, and the attenuation coefficient σ is proportional to $\rho \frac{Z}{A} \frac{1}{E_\gamma}$ (Krieger, 1998, chapter 4).
- Pair production: in the presence of a Coulomb field (from an electron of the atomic shell or the nucleus), the photon is transformed into an electron-positron pair. The first case (electron) is referred to as triplet production because the electron is ejected from the atom. The energy threshold for this process to take place is higher (2044 keV) and the cross section lower (Berger et al., 2010) than for the second case, so that the first one can be neglected in the following. In the second case (nucleus), the energy threshold is the mass of the two leptons (1022 keV), a special situation in which the pair is created at rest. For larger energies, the pair is produced with a certain kinetic energy. The leptons are likely to be stopped within dense detectors and to deposit completely their kinetic energy $E_k = E_\gamma - 2 \times 511$ keV. Where are the missing 1022 keV? The positron (normally when at rest) annihilates with an electron and two 511 keV photons are produced. If these are fully absorbed, the full-energy peak E_γ is recovered. If one or both of these photons escape the detector, the Single and Double Escape Peaks (SDEP) appear at ($E_\gamma - 511$ keV) and ($E_\gamma - 1022$ keV), respectively. It is the dominant mechanism at high photon energies (over 10 MeV), cf. fig. 2.1, and the coefficient κ scales with $\rho \frac{Z^2}{A} \ln E_\gamma$ (Krieger, 1998, chapter 4).

2 Compton camera

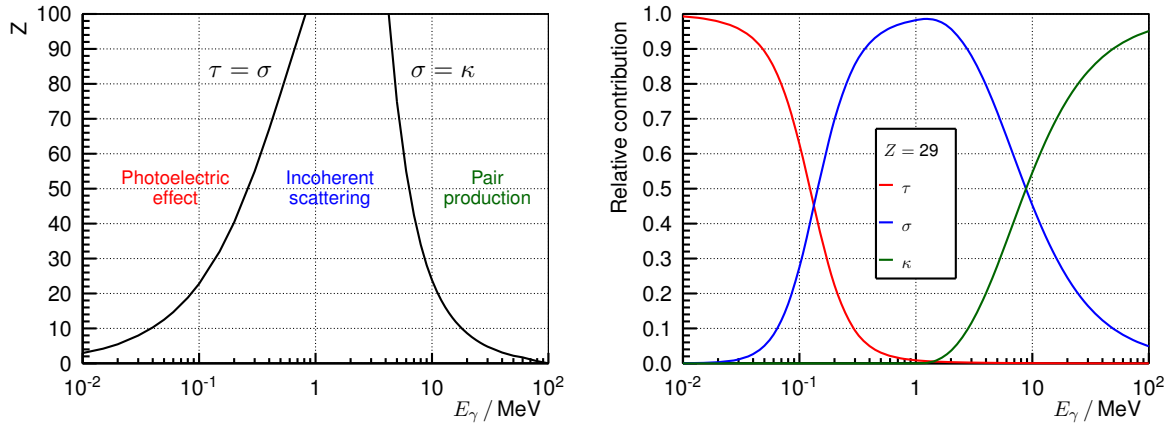


Figure 2.1: Left: regions of predominance of photoelectric effect (τ), incoherent scattering (σ) and pair production (κ) depending on atomic mass number Z of the target and the photon energy E_γ . The solid lines mark the borders where two processes have the same attenuation coefficient. Right: relative contribution to the total attenuation coefficient of the photoelectric (τ), incoherent scattering (σ) and pair production (κ) processes as a function of the photon energy E_γ for a copper target ($Z = 29$). Both: data are taken from (Berger et al., 2010).

For light materials, the approximation $Z/A \approx 1/2$ can be applied and the dependencies of the attenuation coefficients can be summarised as $\tau \propto \rho Z^{3.6}/E_\gamma^3$, $\sigma \propto \rho/E_\gamma$ and $\kappa \propto \rho Z \ln E_\gamma$.

2.1.1 Compton formula and Klein-Nishina cross section

A Cc is a detector system for reconstructing the angle of incidence of a photon based on the second process: the incoherent scattering with an electron (fig. 2.2). This electron is assumed to be at rest (free), as its kinetic and binding energy are usually much lower than the energy transferred by the γ -ray. Based on this approximation, the Compton equation (Compton, 1923) relates the scattering angle θ with the initial (E_γ) and final (E_γ') photon energies:

$$\frac{1 - \cos \theta}{m_e} = \frac{1}{E_\gamma'} - \frac{1}{E_\gamma} \quad (2.1)$$

where $m_e = 511$ keV is the electron mass in natural units, i.e. the speed of light in vacuum $c \equiv 1$.

The derivation of the Compton formula is straightforward using the relativistic formalism of four-vectors. The four-momentum of the photon (γ) and electron (e) before (p) and after (p') the interaction is:

$$p_\gamma = (E_\gamma, \mathbf{p}_\gamma) \quad ; \quad p_\gamma' = (E_\gamma', \mathbf{p}_\gamma') \quad ; \quad p_e = (E_e, \mathbf{p}_e) = (m_e, \mathbf{0}) \quad ; \quad p_e' = (E_e', \mathbf{p}_e') \quad (2.2)$$

where \mathbf{p} refers to the relativistic three-momentum.

According to the law of energy-momentum conservation and the properties of the scalar product in the Minkowski space:

$$\begin{array}{ll}
 p_\gamma + p_e = p_{\gamma'} + p_{e'} & | - p_{\gamma'} - p_e \\
 p_\gamma - p_{\gamma'} = p_{e'} - p_e & | ()^2 \\
 p_\gamma^2 + p_{\gamma'}^2 - 2p_\gamma p_{\gamma'} = p_e^2 + p_{e'}^2 - 2p_e p_{e'} & | p_\gamma^2 = p_{\gamma'}^2 = m_\gamma^2 = 0 \\
 -2p_\gamma p_{\gamma'} = p_e^2 + p_{e'}^2 - 2p_e p_{e'} & | p_e^2 = p_{e'}^2 = m_e^2 \quad | \div (-2) \\
 p_\gamma p_{\gamma'} = -m_e^2 + p_e p_{e'} & | p_e p_{e'} = E_e' E_e - \mathbf{p}_e' \mathbf{p}_e = E_e' m_e \\
 E_\gamma E_{\gamma'} - |\mathbf{p}_\gamma| |\mathbf{p}_{\gamma'}| \cos \theta = m_e (E_e' - m_e) & | E_e' = E_\gamma + m_e - E_{\gamma'} \\
 E_\gamma E_{\gamma'} (1 - \cos \theta) = m_e (E_\gamma - E_{\gamma'}) & | \div E_\gamma E_{\gamma'} m_e \\
 \frac{1 - \cos \theta}{m_e} = \frac{1}{E_{\gamma'}} - \frac{1}{E_\gamma} &
 \end{array}$$

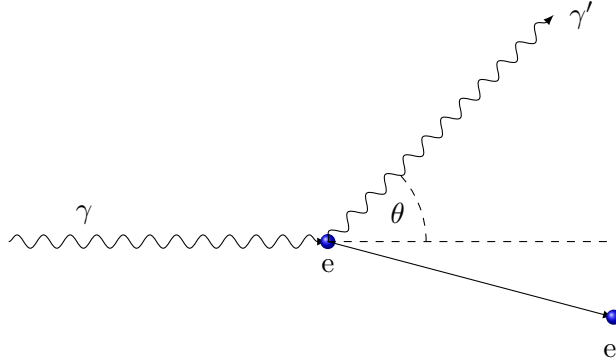


Figure 2.2: Incoherent (Compton) scattering of a photon (γ) with a free electron (e). The electron recoils (e') and the scattered photon (γ') propagates at an angle θ with respect to the original incidence direction.

The energy $E_{\gamma'}$ of the scattered photon as a function of the angle θ is then:

$$E_{\gamma'}(\theta) = \frac{E_\gamma}{1 + E_\gamma(1 - \cos \theta)/m_e} \quad (2.3)$$

And the kinetic energy $T_{e'}$ of the recoiling electron is $T_{e'} = E_{e'} - m_e = E_\gamma - E_{\gamma'}$:

$$T_{e'}(\theta) = E_\gamma \left(1 - \frac{1}{1 + E_\gamma(1 - \cos \theta)/m_e} \right) \quad (2.4)$$

The maximum energy released by a photon in the Compton effect (transferred to the recoil electron) associates to the maximum scattering angle $\theta = \pi$:

$$T_{e'}(\pi)_{\max} = \frac{E_\gamma}{1 + m_e/(2E_\gamma)} \longleftrightarrow E_{\gamma'}(\pi)_{\min} = \frac{1}{2/m_e + 1/E_\gamma} \quad (2.5)$$

The minimum energy deposit is zero for the dispersion angle $\theta = 0$ (no interaction):

$$T_{e'}(0)_{\min} = 0 \longleftrightarrow E_{\gamma'}(0)_{\max} = E_\gamma \quad (2.6)$$

2 Compton camera

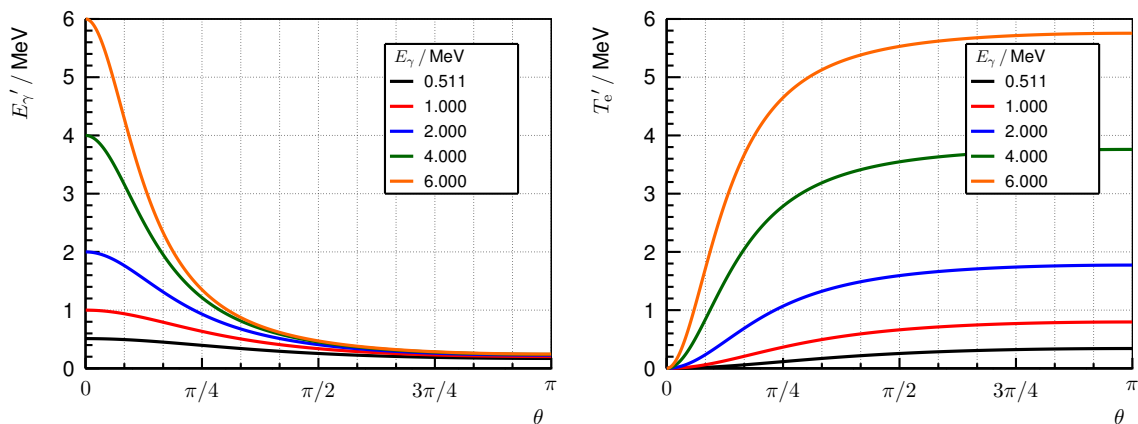


Figure 2.3: Energy of the scattered photon (γ' , left) and recoiling electron (e' , right) as a function of the Compton dispersion angle θ for different energies E_γ of the incident photon.

The derived equations provide the energy of the scattered photon and recoiling electron as a function of the scattering angle $0 \leq \theta \leq \pi$. Fig. 2.3 shows this relationship for several incidence energies E_γ . But does the scattering angle of the original photon take a random value between 0 and π or are some directions more likely? The Klein-Nishina formula describes the differential cross section of photons scattered with a free unpolarised electron (Klein and Nishina, 1929):

$$\begin{aligned} \frac{d\sigma}{d\Omega}(E_\gamma, \theta) &= \frac{\alpha^2 r_c^2}{2} [P(E_\gamma, \theta)^3 + P(E_\gamma, \theta) - P(E_\gamma, \theta)^2 \sin^2(\theta)] \\ P(E_\gamma, \theta) &\equiv \frac{E_\gamma'}{E_\gamma} = \frac{1}{1 + E_\gamma(1 - \cos \theta)/m_e} \end{aligned} \quad (2.7)$$

where α is the fine structure constant, $r_c = 2\pi/m_e$ is the Compton wavelength of the electron (in natural units) and $d\Omega = \sin \theta d\theta d\varphi$. The total cross section σ_T (integrated over the whole solid angle) is:

$$\sigma_T(\eta) = \int_{\theta=0}^{\pi} \int_{\varphi=0}^{2\pi} \frac{d\sigma}{d\Omega} d\Omega = \frac{\pi \alpha^2 r_c^2}{\eta^3} \left[\frac{2\eta[2 + \eta(1 + \eta)(8 + \eta)]}{(1 + 2\eta)^2} + [\eta(\eta - 2) - 2] \log(1 + 2\eta) \right] \quad (2.8)$$

where $\eta \equiv E_\gamma/m_e$.

The Normalised Probability Density Function (NPDF) $f_\theta(\eta)$ of a scattering event of angle θ (the whole azimuthal cone ring is considered) for a given incident energy (or η factor) is:

$$f_\theta(\eta) = \frac{2\pi}{\sigma_T(\eta)} \frac{d\sigma}{d\Omega}(\eta, \theta) \sin \theta \quad (2.9)$$

so that $\int_0^\pi f_\theta(\eta) d\theta = 1$. This density function is depicted in fig. 2.4. It can be observed that forward scattering is more likely than backscattering, specially for high incident photon energies.

An analogous NPDF depending on the scattered photon energy E_γ' can be obtained with the

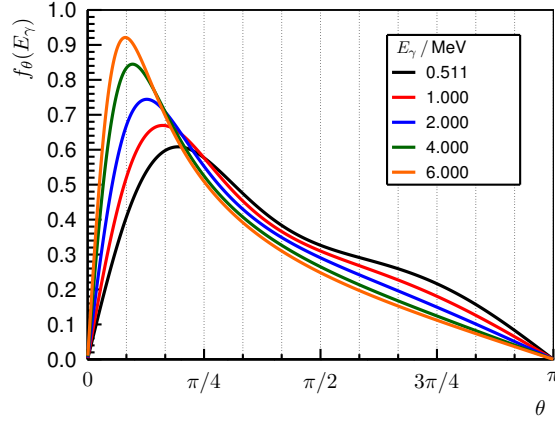


Figure 2.4: Normalised differential Klein-Nishina cross section as a function of the scattering angle θ for different incident photon energies E_γ , cf. eq. 2.9.

change of variable $\theta(E_\gamma') = \arccos[1 + m_e(1/E_\gamma - 1/E_\gamma')]$, $d\theta = -|\operatorname{cosec} \theta| m_e E_\gamma'^{-2} dE_\gamma'$:

$$f_{E_\gamma'}(\eta) = \frac{2\pi}{\sigma_T(\eta)} \frac{d\sigma}{d\Omega}(\eta, \theta) \frac{m_e}{E_\gamma'^2} \quad (2.10)$$

where the condition $\int_{E_\gamma'(\pi)_{\min}}^{E_\gamma'(0)_{\max}} f_{E_\gamma'}(\eta) dE_\gamma' = 1$ is fulfilled. The NPDF as a function of the kinetic energy of the recoiling electron T_e' is achieved with the trivial change $E_\gamma' = E_\gamma - T_e'$.

Fig. 2.5 shows the resulting probability distributions for different incident γ -ray energies.

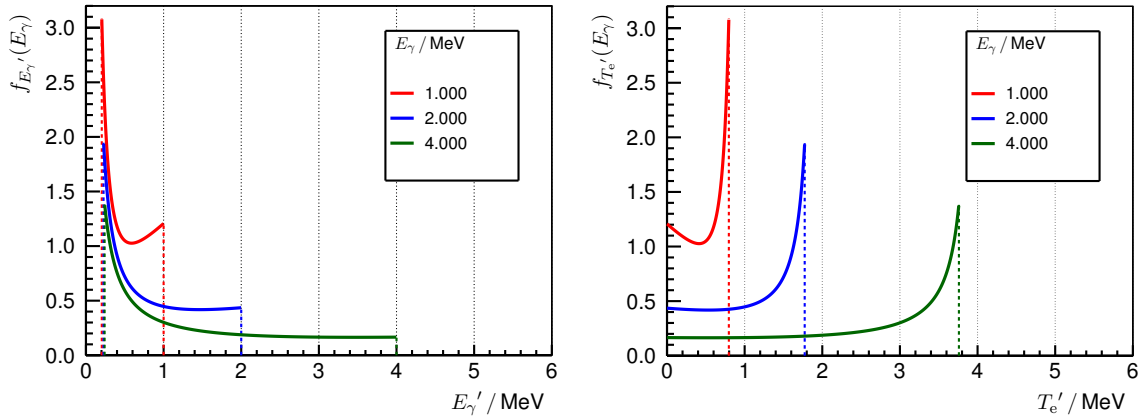


Figure 2.5: Normalised differential Klein-Nishina cross section as a function of the scattered γ -ray energy E_γ' (left) or the kinetic energy of the recoiling electron T_e' (right) for different incident photon energies E_γ , cf. eq. 2.10. The peak in the right plot is called the Compton edge, which is located left from the photopeak, at $T_e'(\pi)_{\max} = \frac{E_\gamma}{1+m_e/(2E_\gamma)} = E_\gamma - \frac{1}{1/E_\gamma+2/m_e}$.

The peak in the NPDF of fig. 2.5 (right) is the so called Compton edge, which is usually visible (after convolution with the detector resolution) in detector response energy spectra together with the photopeak, and SDEP (if pair production is possible).

2.1.2 Detection principle

A camera based on two detector planes, which measure (each) the energy loss and interaction position of photons, is assumed. An incident γ -ray of unknown propagation direction scatters at the first plane and is fully absorbed in the second plane. This *Compton event* is registered by the camera. Assuming this ideal process and perfect detectors, the energy deposit in the *scatterer plane* (L_s) and in the *absorber plane* (L_a) are related to the energies of the incident and scattered photons:

$$\begin{aligned} E_\gamma &= L_s + L_a \\ E_{\gamma'} &= L_a \end{aligned} \quad (2.11)$$

Substituting in eq. 2.1, the scattering angle θ can be reconstructed. The conditions $E_\gamma > 0$, $E_{\gamma'} > 0$ and $[2/m_e + 1/E_\gamma]^{-1} \leq E_{\gamma'} < E_\gamma$ (so that the cosine is between -1 and 1) have to be fulfilled. However, as only the propagation direction of the scattered photon is known, the incident direction cannot be recovered univocally. Rather, the possible incident trajectories define a cone surface of infinite solutions: the *Compton cone*. As seen in fig. 2.6, the apex of the cone corresponds to the interaction point in the scatterer, while the propagation direction of the scattered γ -ray defines the cone directrix. The half-opening angle is the scattering angle θ , calculated with eqs. 2.1 and 2.11, and the original γ -ray incidence direction could be any generatrix contained in the cone surface.

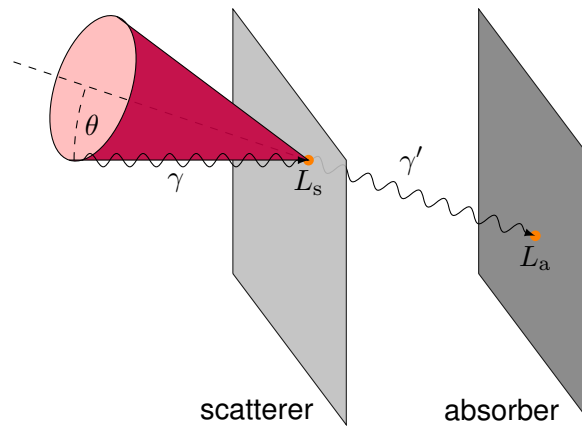


Figure 2.6: Incoherent scattering event in a two-plane Cc. The cone surface contains the possible incidence directions (any generatrix) of the initial photon (γ). It interacts with the scatterer plane and deposits an energy L_s . The scattered photon (γ') releases the rest of the energy L_a in the absorber. The line connecting both interaction points (in orange) is the propagation direction of γ' . This defines the axis (directrix) of the aforementioned cone, with half-opening angle θ and vertex at the scatter point.

2.1.3 Intersection of cone surface and plane

For reducing to some extent the number of possible solutions, the following condition is added: the source of γ -rays is contained within an *imaging plane* at a known distance and

orientation with respect to the Cc camera. This is a realistic assumption for the prompt γ -ray distribution of single pencil beams. Indeed, the imaging volume could even be constrained to a 1D straight line, but the plane generality will be kept. In order to obtain the possible photon emission points within this imaging plane, its intersection with the Compton cone shell is calculated.

Fig. 2.7 defines a laboratory coordinate system S , in which the Cc camera and the imaging plane are fixed, and a local coordinate system S^* , that is specific for each Compton event. Each system has different origins and the respective orthonormal vectors of the base are $(\hat{i}, \hat{j}, \hat{k})$ and $(\hat{i}^*, \hat{j}^*, \hat{k}^*)$, namely the unit vectors of the coordinate axes.

The imaging plane does not intersect with the detector volume and is in front of the camera (faces the scatterer plane). It is described (in S) in the point-normal form by a vector \vec{r}_0 to a point within it and a unit vector \hat{n}_I (pointing in opposite direction to the detectors). The Compton cone is defined by its vertex \vec{v}_s (the scatter point), the cone axis \hat{n}_c (unit vector anti-parallel to the propagation direction of γ') and the half-opening angle θ .

The local event-based coordinate system (S^*) has its origin at \vec{v}_s with the z^* axis parallel to \hat{n}_c and the y^* axis parallel to the projection of \hat{n}_c onto the xy -plane (of S).

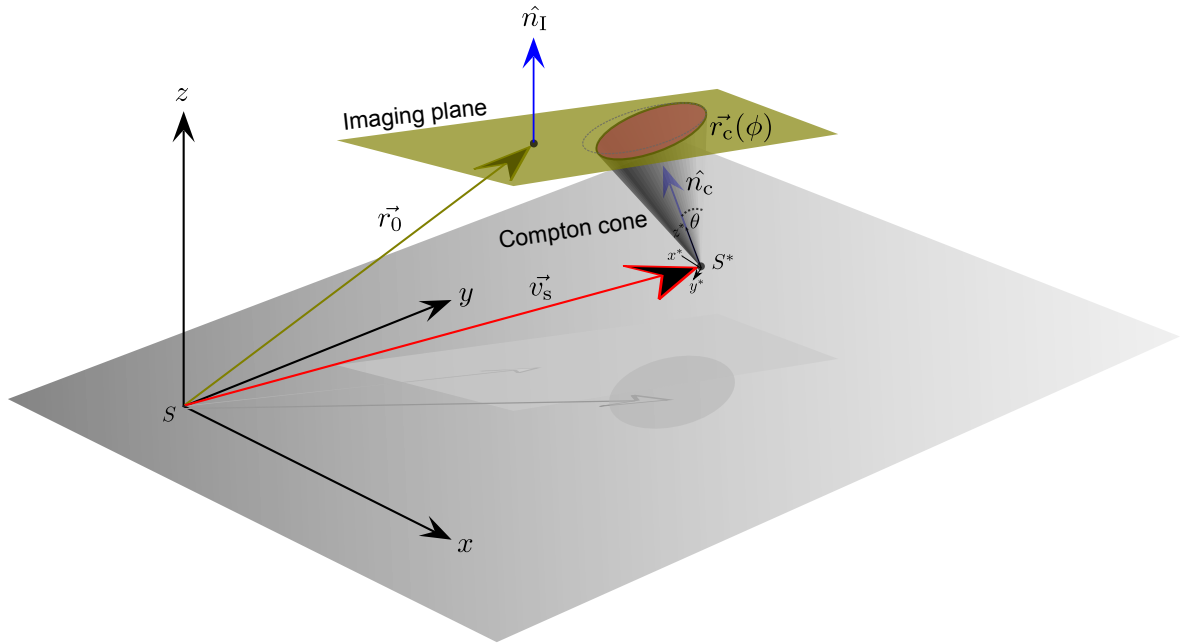


Figure 2.7: Scheme of the coordinate system convention for a typical Compton event. The reference frame is the laboratory coordinate system S . The vector \vec{v}_s points to the location where γ is scattered. At this position, a local coordinate system S^* is defined, with the z^* axis parallel to the cone axis \hat{n}_c (unit vector antiparallel to the propagation of γ'). The cone half-opening angle is θ . \vec{r}_0 is the position vector of the imaging plane and \hat{n}_I the normal vector (pointing in opposite direction to the scatter point). The parametric vector equation $\vec{r}_c(\phi)$ denotes the conic section (dashed ellipse) resulting from the intersection of Compton cone and imaging plane, cf. eq. 2.19.

2 Compton camera

The euclidean transformation $T(\vec{v})$ from S to S^* is defined by a translation \vec{t} between the origins and an Euler rotation $R(\alpha, \beta, \Gamma)$ of the axes.

$$T(\vec{v}) = R\vec{v} + \vec{t} \quad (2.12)$$

The translation is $\vec{t} = -\vec{v}_s$. The Euler rotation angles (following the classic convention) are:

$$\begin{cases} \alpha &= \cos^{-1}(\hat{n}_c \cdot \hat{i}) - \pi/2 \\ \beta &= -\cos^{-1}(\hat{n}_c \cdot \hat{k}) \\ \Gamma &= 0 \end{cases} \quad (2.13)$$

Any displacement vector in S can be expressed in terms of the base of S^* by applying the Euler rotation R . For positional vectors, the expression in S^* is calculated with the full transformation T . For example, $\hat{n}_{c|S^*} = R \cdot \hat{n}_{c|S}$ (same vector in different bases) and $\vec{r}_0^* = T(\vec{r}_0)$ (different vectors).

The point-normal equation of the imaging plane I in S^* is:

$$\hat{n}_{I|S^*} \cdot (\vec{r}^* - \vec{r}_0^*) = 0 \quad (2.14)$$

Or the implicit standard form:

$$A^*x^* + B^*y^* + C^*z^* + D^* = 0 \quad (2.15)$$

where $A^* = \hat{n}_{I|S^*} \cdot \hat{i}^*$, $B^* = \hat{n}_{I|S^*} \cdot \hat{j}^*$, $C^* = \hat{n}_{I|S^*} \cdot \hat{k}^*$ and $D^* = -\hat{n}_{I|S^*} \cdot \vec{r}_0^*$.

The cone surface is described in cylindrical coordinates in S^* (fig. 2.8) as:

$$\vec{r}_c^* = \rho \cdot \begin{pmatrix} \cos \phi \\ \sin \phi \\ \cot \theta \end{pmatrix} \quad (2.16)$$

For a fixed azimuthal coordinate ϕ and free ρ , the equation of a generatrix is obtained. In order to restrict the solutions to just one of the two cone leaves, z^* must be positive for $\theta \in (0, \pi/2)$, zero for $\theta = \pi/2$ and negative for $\theta \in (\pi/2, \pi)$, i.e. the constraint $\rho > 0$ has to be fulfilled. It is also assumed that the origin of S^* is not contained within the imaging plane.

For calculating the intersection of cone shell and imaging plane, eq. 2.15 is evaluated for $\vec{r}^* = \vec{r}_c^*$:

$$A^*\rho \cos \phi + B^*\rho \sin \phi + C^*\rho \cot \theta + D^* = 0 \quad (2.17)$$

Hence, the following parametric equation $\rho(\phi)$ for the intersection is found:

$$\rho(\phi) = \frac{-D^*}{A^* \cos \phi + B^* \sin \phi + C^* \cot \theta} \quad (2.18)$$

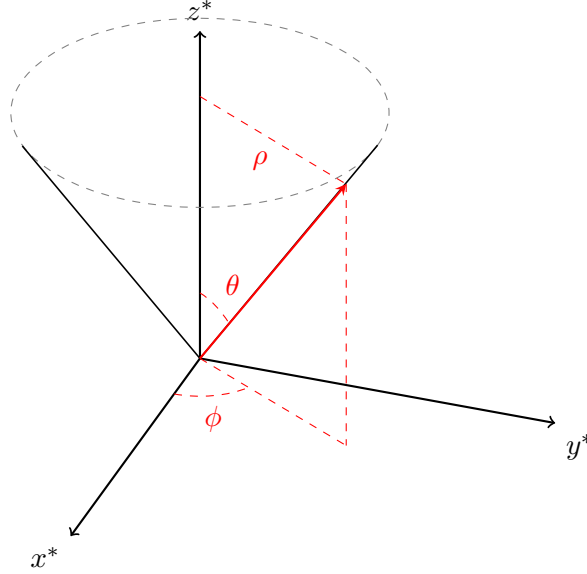


Figure 2.8: Description of the cone surface in cylindrical coordinates $(\rho, \phi, z^* = \rho \cot \theta)$ in the local frame S^* . The red vector is directed at a generic point of the surface. The half-opening angle of the cone is θ , the apex is in the origin of the coordinate system and the directrix is the z^* axis.

The intersection $\vec{r}_c(\phi)$ in the Cartesian coordinate system S is obtained by substituting eq. 2.18 in eq. 2.16 and applying the inverse Euclidean transformation $T^{-1}(\vec{v}) = R^{-1}\vec{v} - \vec{t}$:

$$\vec{r}_c(\phi) = \vec{v}_s + \frac{-D^*}{A^* \cos \phi + B^* \sin \phi + C^* \cot \theta} \cdot R^{-1}(\alpha, \beta, \Gamma) \cdot \begin{pmatrix} \cos \phi \\ \sin \phi \\ \cot \theta \end{pmatrix} \quad (2.19)$$

where $\phi \in [0, 2\pi)$ and $\rho > 0$.

The intersection of a plane with a cone surface is a conic section: either an ellipse, a parabola or an one-arm hyperbola. The parabola is obtained for a critical half-opening angle θ_p where the farthest cone generatrix, cf. fig. 2.9, is parallel to (does not intersect with) the imaging plane. For lower θ , the intersection is an ellipse, for higher a hyperbola. There is no intersection at all if the critical angle θ_h is reached, where the closest generatrix is parallel to the plane. Mathematically, assuming that the cone axis points towards the imaging plane, i.e. $\delta = \cos^{-1}(\hat{n}_c \cdot \hat{n}_1) \leq \pi/2$, it is obtained that $\theta_p = \pi/2 - \delta$ and $\theta_h = \pi/2 + \delta$, cf. fig. 2.9.

Ellipse	if $0 < \theta < \theta_p$	(2.20)
Parabola	if $\theta = \theta_p$	
Hyperbola	if $\theta_p < \theta < \theta_h$	
/	if $\theta_h \leq \theta < \pi$	

$\theta = 0$ and $\theta = \pi$ are special cases where eq. 2.18 is not well defined. Assuming that the cone axis is not parallel to the imaging plane (i.e. $C^* \neq 0$ or $\delta \neq \pi/2$), and that the cone axis (unit vector \hat{n}_c) is inverted for $\theta = \pi$, the equation of the intersection (a point instead of a

2 Compton camera

curve) is just:

$$\vec{r}_c = \vec{v}_s - \frac{D^*}{C^*} \cdot R^{-1}(\alpha, \beta, \Gamma) \cdot \begin{pmatrix} 0 \\ 0 \\ 1 \end{pmatrix} \quad (2.21)$$

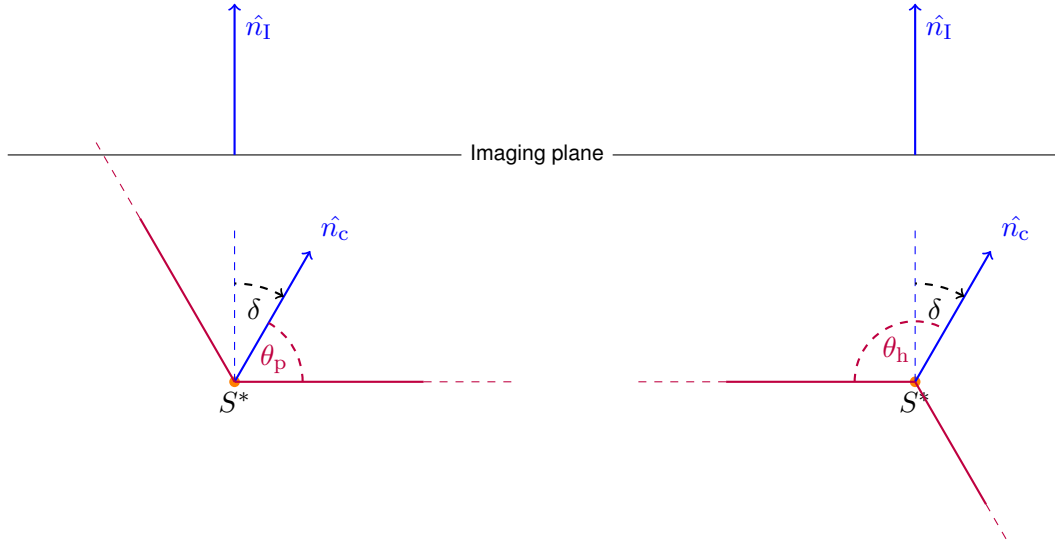


Figure 2.9: Section of the 3D space defined by the Compton cone apex (origin of S^*), the cone axis (\hat{n}_c) and the normal vector of the imaging plane (\hat{n}_I). The cone axis is directed to the imaging plane ($0 \leq \delta \leq \pi/2$). The cone generatrices are depicted in purple. Left: critical half-opening angle θ_p for which the right generatrix of the cone is parallel to the imaging plane (just the left generatrix intersects). Right: critical half-opening angle θ_h for which the left cone generatrix is parallel to the plane (Compton cone does not intersect any more).

A rigorous derivation and extension of this analytical approach is given in (Lojacono, 2013). In theory, assuming ideal and infinite planar detectors, a single stationary Cc is able to reconstruct \mathbb{R}^3 activity distributions, instead of just \mathbb{R}^2 (Cree and Bones, 1994).

2.1.4 Practical considerations

The intersection equation of a single Compton event is not enough to localise the origin of a point-like photon source (a priori information is only that it is contained within the imaging plane). The true azimuthal angle ϕ_c or generatrix through which the original γ -ray has propagated is an unknown. Nonetheless, if further Compton events are registered by an ideal camera, all conic sections are expected to intersect at a single point: the photon source.

The Back Projection (BP) is a simple method to reconstruct the γ -ray emission distribution based on the accumulation of events in a spatial 2D histogram of the imaging plane. For each Compton event, $\vec{r}_c(\phi)$ is sampled uniformly (equal weights for all values of ϕ). The $[0, 2\pi)$ range is divided in a finite number of steps. For each angle (intersection point), an entry in the histogram is added. In other words, a finite set of equally spaced generatrices of

the cone shell is chosen and their respective intersection bin in the imaging plane histogram is calculated (filled).

This equal-weight approach, with just kinematic and geometrical derivation, seems reasonable in an ideal camera with a monochromatic point-like photon source. How does this scenario change in the case of an extended source or realistic detectors? How are the probabilities of the respective Compton cones affected? Several weight factors can be taken into account in the reconstruction process:

- *Solid angle*: given a finite area of the C_c , the solid angle covered by the scatterer detector is different for each bin of the imaging plane. A point source located at the minimum distance between plane and detector will generate much more events in the camera than a twin source at a point of the imaging plane much farther away from the detectors. Thus, the fewer events of the farther source should have a higher weight to compensate for the ones from the closer one and reconstruct reliably the same photon activity in both points.
- *Effective thickness*: for realistic detector dimensions, the effective thickness (detection efficiency) depends on the incidence direction of the γ -ray. For sources far away from the center of the field of view, the γ -rays may enter the scatterer detector from the side face rather than from the front face, so that the effective thickness is the actual crystal width, which is normally larger than its thickness. Hence, the detection efficiency is bigger than for a source at equal distance but located perpendicularly to the front face. Within the imaging plane, this effect plays in the opposite direction to the solid angle (previous bullet point).
- *Klein-Nishina formula*: it provides the differential cross section per solid angle of photons scattered at a free electron, cf. eq. 2.7. For example, 6 MeV photons are scattered more likely in forward than in backward direction, whereas the angular distribution of lower energy photons is more symmetric, cf. fig. 2.4. Given a point-like source, the mean photon incidence angle affects the probability of coincident detection in the scatterer and absorber. If the propagation of the original photon is straight towards the camera and forward scattering is favoured, the parallel absorber plane will detect most of the scattered rays. If the initial incidence direction is too oblique, many scattered rays will not even cross the area of the absorber.
- *Attenuation*: if there is a dense material between the imaging plane and the C_c , γ -rays can be attenuated before reaching it. The strength of the attenuation depends on the material composition as well as the distance between photon emission point and scatter point. Attenuation inside the scatterer plane (multiple scattering) before reaching the absorber is also possible and plays a significant role if the first one is not very thin.
- *Threshold*: real detectors have an energy threshold below which γ -rays cannot be detected. For Compton events where the scattering angle is small, the energy loss

2 Compton camera

in the scatterer is low, cf. fig. 2.3 (right). If a time coincidence filter is set, only events above a critical scattering angle deposit energy enough to be detected. In other words, a Cc with parallel (and small) detector planes has a blind spot or is less sensitive to point sources in the center of the field of view than those slightly off the axes.

- *Doppler broadening*: the incoherent scattering with a bound electron which is not at rest blurs the energy of the scattered photon and the scattering angle (Kormoll, 2012) with respect to the one derived by means of the Compton formula.
- *Resolution*: the limited energy resolution of γ -ray detectors affects the precision of the calculated cone angle. As a result, the true conic section is blurred in the real experiments. The spatial resolution influences the apex of the cone and the orientation of the axis, which contributes also to the degradation of the reconstructed image. The time resolution has also an impact on the electronic coincidence condition (absorption is almost simultaneous to scattering, about 0.1 ns separation). Insufficient time resolution (several nanoseconds) can lead to *random coincidences*, i.e. the erroneous association of single uncorrelated events in each plane, and add noise to the image.
- *Escape energy*: the assumption of incoherent scattering in the first plane and full absorption in the second plane is ideal. Actually, a second incoherent scattering instead of photoabsorption, or pair production with the escape of one or two annihilation photons, are feasible (Rohling, 2015) and lead to an underestimation of the initial γ -ray energy, which biases ultimately the cone half-opening angle. Moreover, pair production can occur already in the scatterer, an annihilation photon may leave it and be then detected in the absorber. This leads to a false coincidence that cannot be filtered out even with good timing resolution. Another effect if the scatterer is very thin and the energy deposit is high is that the recoiling electron can escape the detector before releasing its full kinetic energy, so that the reconstructed cone angle is biased.
- *Backscattering*: events where the photon scatters in the absorber plane and is absorbed in scatterer are also possible (Rohling, 2015). Several identification techniques are used e.g. in axial PET (Hueso González, 2012) to discriminate and even take profit from this reverse interaction order.

One can clearly see how sophisticated a reconstruction algorithm can or should be in order to take into account all these factors. A review of the available methods, mainly based on Maximum-Likelihood Expectation-Maximisation (MLEM), is given in (Lojacono, 2013).

For the PET imaging field, the MLEM method is an established algorithm to reconstruct 3D activity distributions (Shepp and Vardi, 1982) with millimetre precision. The iteration process recovers the most likely activity distribution that matches with the measurement set. There are certain concerns on noise regularisation and iteration stopping criterion (Ben Bouallègue et al., 2013), but the overall performance is excellent. For the Compton imaging field, measurement uncertainties and background are much higher and may challenge the MLEM reconstruction algorithms.

The basic problem is one dimension higher: a cone of response instead of a line of response. In any case, one should not expect *miracles* from the reconstruction algorithms, to compensate for all uncertainties, noise, background and even obtain an accurate 3D activity distribution. Such inverse problems are not well conditioned and one may want to focus on reducing the experimental errors instead of developing very sophisticated models and simulations to counteract these in the reconstruction process. The reduction of the imaging volume to a single line (approaching the ~ 1 cm wide pencil beam track) may be a good strategy to reduce the number of dimensions and balance the higher uncertainties than for PET.

This dissertation is restricted to the analytical BP method. More complex reconstruction algorithms, as mentioned above, are a science themselves and exceed the scope of this work, which focuses on experimental measurements and simple analytical models.

One big concern for the PGI energy range, where the incoherent and pair production cross sections are significant, cf. fig. 2.1 (right), is the escape energy. Instead of a photoelectric effect, a second incoherent scattering is likely to happen in the absorber and leads to an underestimated value of the γ -ray energy. The true value cannot be estimated in the PGI scenario as the γ -ray source is not monoenergetic, cf. fig. 1.5 (left). All the more, a pair production event instead of a photoelectric absorption involves the creation of an electron-positron pair. The leptons are likely to be stopped within few millimetres in high density materials, so that their kinetic energy is released in the detector. However, the full γ -ray energy is only recovered if the two annihilation photons (due to the positron) are also fully absorbed. However, in contrast to the leptons, one or both of these photons may escape even high density materials with moderate probability and bias negatively the energy deposit in the crystal, leading to the SDEP left from the photopeak.

An interesting workaround is the use of a multi-plane Cc (at least three), for which the Compton cone is correctly opened even in the absence of photoelectric absorption. This requires a coincident detection in three detectors (Peterson et al., 2010). The drawbacks are lower coincident efficiency (if two-layer events are discarded), higher influence of random coincidences and energy threshold, and more interaction order combinations. Another option is to use a two-plane camera, but leave the energy escape as free parameter in the MLEM algorithm (Ortega et al., 2015), the so called spectral reconstruction.

A general comment concerning γ -ray detectors, in contrast to charged particle detectors, is that it is not possible to obtain the energy of the γ -ray E_γ event-wise. Rather, a statistical combination of many interaction processes leads to a full-energy peak, a Compton continuum and edge, and SDEP. The energy released in the detector L , cf. eq. 2.11, is not E_γ . Throughout the dissertation, the experimental energy spectra are not the original distributions of γ -ray energies but the detector response to a given radiation field. For convention, the horizontal axis of the histogram is labelled as energy E , referring to L and not to E_γ .

2.2 Motivation

The imaging of the prompt γ -rays produced by a clinical proton beam represents an experimental challenge due to several factors mentioned in section 1.4 and summarised here:

- The broad and polychromatic energy spectrum up to ~ 10 MeV (range of interest lies between 1 and 8 MeV) (Verburg and Seco, 2014).
- The high instantaneous production rate of about 10^9 γ -rays per second (Hueso González et al., 2015b) for the C230 accelerator, emitted within a spatial region on the 20 cm scale and in all directions.
- The large radiation background due to neutrons (generating secondary γ -rays), scattered charged particles and material activation (Newhauser and Zhang, 2015).

Several PGI systems have been proposed and designed in the recent years. Among these, the Cc has probably the highest requirements concerning detectors, electronics and data processing. It is important to choose detector materials that adapt to this specific environment and cope best with the constraints mentioned above. Diverse theoretical studies and simulations about the geometry and material choice of a Cc for PGI have been published in the last years (Robertson et al., 2011; Kormoll, 2012; Richard, 2012). The prerequisites of a camera comprising (for simplicity) two layers are listed below:

- An excellent energy resolution is mandatory to accurately calculate the scattering angle θ of the incident γ -ray by means of the Compton equation, cf. eq. 2.1, which defines the opening angle of the cone of response, as depicted in fig. 2.6. If the incident γ -ray energy is known, it is enough to have a good energy resolution in the scatterer. Otherwise, this requirement applies also to the absorber.
- A high spatial resolution is needed for placing the Compton cone vertex in the 3D space and orientating its axis.
- A good timing resolution is advisable for filtering out false coincidences due to the high rate of (non-prompt) background in the clinical environment, as well as uncorrelated interactions (single events) in scatterer and absorber due to critically high detector load.
- A high absorption efficiency (density as well as effective atomic number) is needed in the absorber to fully stop the prompt γ -rays, which have an energy up to 6 MeV, to minimise the effect of escape energy (incomplete energy deposition) in the reconstruction.
- A trade-off between energy resolution and absorption efficiency. Since the prompt γ -ray spectrum is not monoenergetic, the absorber requires in principle a high energy resolution (see above). However, as the energy range is high, incoherent scattering predominates over photoabsorption and (twice) scattered γ -rays may escape the detector with moderate probability. Hence, it may be of greater importance to use very

dense (or thick) materials, as a high energy resolution is wasted anyway if there is missing energy.

- The material should be radiation hard for sustaining the high rates and damage due to secondary particles (neutrons, charged particles).
- To cope with the high expected radiation rate, scintillation detectors with very long decay times or large afterglow are not advisable.
- Intrinsic radioactivity of the material is a drawback as it can lead to false coincidences.
- Non-hygroscopic materials are preferred in order to avoid scattering in the sealing.
- Concerning clinical implementation, the camera should be placed at ~ 30 cm distance from the beam axis and have a low footprint for minimising the interference with the patient and medical staff. Furthermore, a compromise between camera size (higher sensitivity) and affordable price (commercial applicability) has to be reached.

Taking into account these numerous requirements, block detectors from standard PET scanners (Humm et al., 2003), made of Cerium-doped lutetium oxyorthosilicate - $\text{Lu}_2\text{SiO}_5:\text{Ce}$ (LSO) and Bismuth Germanium Oxide - $\text{Bi}_4\text{Ge}_3\text{O}_{12}$ (BGO), are straightforward candidates for the absorber plane. They are well-known detectors, non-hygroscopic and radiation hard (Mao et al., 2011; Zhang et al., 2012). Furthermore, their absorption efficiency is high due to their density and effective atomic number, and the energy, spatial and timing resolution are good.

Textbook knowledge related to PET scanners (Humm et al., 2003), where the γ -ray energy is limited to 511 keV, is that LSO pixellated detectors have gained importance to the detriment of cheaper BGO due to a better performance concerning energy, spatial and time resolution. The reasons therefore are its four times higher light yield (number of scintillation photons per absorbed energy) and the much shorter decay time. Several studies comparing the different performance of BGO and LSO for PET (Melcher, 2000; Weber et al., 2003; Ramirez et al., 2005; Szczesniak et al., 2013) have been published.

Is this prior experience enough to discard BGO as absorber of a PGI Cc? How does the increased γ -ray energy affect the scintillator performance? Does the four times higher cost of LSO crystals (Gektin et al., 2012, p. 64) match also in the PGI scenario with the boost in performance compared to BGO? Whether or not the higher energies (and thus number of scintillation photons) will suffice for considering BGO as a competitive alternative to LSO is an essential question of this chapter. To answer it, experiments to characterise the two types of block detectors in clinical-like radiation fields are mandatory.

On a different note, a slight scepticism has settled down in the scientific community concerning the applicability of the Cc for medical applications like PGI. Many different projects have run for many years, showing only experimental results in the laboratory (Llosá et al., 2013), in restricted beam environments (Kormoll et al., 2013), or in a clinical center but for a single source position and low energy prompt γ -rays (Kabuki et al., 2009), with lower correlation to

the dose (Verburg and Seco, 2014). Until now, the single experimental proof of principle of range shift identification of a Cc at a clinical ion beam facility based on high energy prompt γ -rays (> 2 MeV) has been published with currents far below the clinical case (Polf et al., 2015). What are such strong difficulties? The technical complexity, high number of electronic channels, the price, the energy, spatial, time resolution requirements of the detectors, the low coincident efficiency, the high γ -ray flux in a clinical scenario, the radiation background and the elevated percentage of random coincidences are the main intrinsic hurdles.

Is it then feasible at all (for clinical beam currents)? Or will they unfortunately be overwhelmed by a constant flow of unwanted events in the different stages? – as raised by (Smeets, 2012). Should the community switch to other techniques? To answer this question, further experimental results on which to build upon are needed, that disclose or confirm the worst expectations. Further results need to complement the existing measurements (Polf et al., 2015), simulation studies, and drive the design of future clinical prototypes. Knowing all difficulties, it is of great importance to approach the problem step by step. First, the feasibility in a clinical environment with realistic rates has to be verified with the simplest methods and minimal efforts necessary. If the proof is successful, further complexity steps can be added to improve the camera efficiency (size) and its precision; the factors degrading the reconstructed images can be identified, and the reconstruction algorithm can be extended or optimised. The other way round, it is difficult to find at which point of the chain something is failing or if it is not working from the very grounds.

Following the *keep it simple* philosophy, a two-plane Cc and the analytic BP method are chosen. In addition, high efficiency detectors are favoured to the detriment of high energy resolution materials. A three-plane camera is discarded. First tests are done with low beam currents and long measurement times, in order to gather enough statistics to draw significant conclusions. One can then analyse the effect on the image when progressively reducing statistics. By renouncing to complex reconstruction algorithms, possible errors in the sensitivity matrix, iterative algorithms or a priori assumptions are avoided. It is expected that, by bypassing this exponentially growing complexity, images of range shifts at a clinical proton beam are shown, at the price of bad resolution, and that the question whether or not the setup is scalable to realistic beam currents can be assessed. The thesis is that, if range shifts can be appreciated with simple means, they should be distinguishable with more complex systems with at least the same precision. Furthermore, these simple tests should be an indispensable precondition, guidance and toehold in the future development of the Cc.

2.3 Goals

Two independent topics, already introduced in the previous section, are addressed throughout chapter 2: the detector choice for the absorber of a Cc (Hueso González et al., 2015a) and the test of a high efficiency camera setup (two planes) at a proton pencil beam.

With regard to the first one, the performance of BGO and LSO scintillators for range verification as part of a PGI clinical system, namely as absorber of a Cc, is compared. Benchmark experiments are conducted at different accelerators, which provide a photon radiation field similar either in the energy range and/or timing structure with the one expected in a clinical pulsed accelerator (Verburg et al., 2013). BGO and LSO detectors are compared specifically in terms of energy, spatial and time resolution. Factors like absorption efficiency, intrinsic activity, and cost-effectiveness ratio are also addressed. The experimental results at these measurement campaigns expand and complement the theoretical predictions and simulations performed already in this field. The suitability of BGO as an alternative to LSO as absorber choice of a Cc aiming at PGI is discussed.

Concerning the second one, a Cc setup assembled at OncoRay¹ and Helmholtz-Zentrum Dresden-Rossendorf (HZDR), which is based on two segmented BGO block detectors, is presented. The rationale is to maximise the incoherent interaction efficiency of the scatterer to the detriment of higher energy resolution but less dense materials. The aim is to prove experimentally the sensitivity of this camera to range shifts of a proton pencil beam for high energy prompt γ -rays. The effect of target shifts, increase of target thickness, and proton energy variation on the reconstructed images is analysed. The applicability of this Cc design in a clinical scenario is discussed based on estimates of realistic beam currents and collected statistics.

2.4 Materials

At OncoRay and HZDR, various Compton imaging detector setups are under evaluation (Kormoll et al., 2013; Hueso González et al., 2014). The absorber comprises PET block detectors (from commercial scanners) based on LSO and/or BGO scintillators. These are tested individually at several research accelerators for comparing their performance as absorber. A combination of two BGO block detectors is also used as high efficiency Cc setup for imaging prompt γ -rays produced by a clinical proton pencil beam at UPTD.

2.4.1 Scintillator properties

Table 2.1 summarises the main properties of LSO and BGO scintillation materials. Fig. 2.10 depicts the attenuation coefficient of photons with the material for the different interaction mechanisms. Based on these literature reference values, one can draw some conclusions concerning the intrinsic potentials of each scintillator:

¹OncoRay – National Center for Radiation Research in Oncology, Faculty of Medicine and University Hospital Carl Gustav Carus, Technische Universität Dresden, Fetscherstr. 74, PF 41, 01307 Dresden, Germany.

Table 2.1: Comparison of basic properties of the LSO and BGO scintillation materials.

	LSO	BGO	Units
Chemical formula	Lu ₂ SiO ₅ :Ce	Bi ₄ Ge ₃ O ₁₂	
Mass density ρ	7.40	7.13	g/cm ³
Melting point MP	2050	1050	°C
Molière radius R_M	2.07	2.23	cm
Radiation length X_0	1.14	1.12	cm
Nuclear interaction length λ_I	20.9	22.8	cm
dE/dx per <i>mip</i>	9.6	9.0	MeV/cm
Effective atomic number Z_{eff}	66 ± 1	74 ± 1	
Effective mass number A_{eff}	162 ± 2	186 ± 2	
$\rho Z_{\text{eff}}^{4.6}/A_{\text{eff}}$	10 ± 1	14 ± 1	g/cm ³ × 10 ⁶
$\rho Z_{\text{eff}}/A_{\text{eff}}$	3.0 ± 0.1	2.8 ± 0.1	g/cm ³
$\rho Z_{\text{eff}}^2/A_{\text{eff}}$	190 ± 10	200 ± 10	g/cm ³
Light yield LY	85	21	% NaI
$d(LY)/dT$	−0.2	−0.9	%/°C
Rise time	~ 30	~ 30	ps
Decay time	40	300	ns
Peak excitation λ_{exc}	358 ± 1	304 ± 1	nm
Maximum emission λ_{max}	402	480	nm
Cut-off transmission	390 ± 5	315 ± 5	nm
Index of refraction n	1.82	2.15	
Photofraction @ 511 keV	34	44	%
Energy resolution R_E @ 662 keV	8	9	%
Afterglow	< 0.1/6	0.005/3	%/ms
Internal activity	~ 280	0	Bq/cm ³
Hygroscopic	No	No	
Radiation hardness	Yes	Yes	
Price in year 2010	40	9	\$/cc

Note: data are extracted from (Derenzo et al., 2000; Humm et al., 2003; Bailey et al., 2005; Crespo, 2006, p. 55; Berger et al., 2010; Mao et al., 2012; PDG, 2012, p. 345). λ_I is the mean distance travelled by high energy hadrons inside the material before an inelastic nuclear reaction takes place. The abbreviation *mip* refers to minimum ionising particle. The terms $\rho Z_{\text{eff}}^{4.6}/A_{\text{eff}}$, $\rho Z_{\text{eff}}/A_{\text{eff}}$ and $\rho Z_{\text{eff}}^2/A_{\text{eff}}$ are proportional to the photoelectric, incoherent and pair production cross section, respectively, cf. section 2.1. Photofraction means the photoabsorption relative to the total attenuation coefficient. The relative energy resolution R_E refers to the Full Width at Half Maximum (FWHM). The prices given for crystals are rough estimates (Gektin et al., 2012, p. 64) based on a comparison of raw material costs. They are of course affected by the actual market situation.

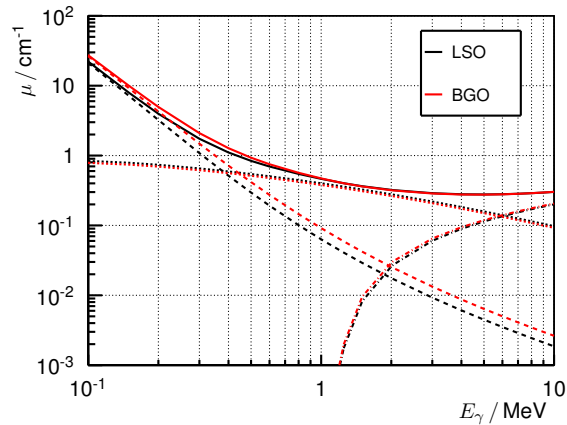


Figure 2.10: Comparison of the photon attenuation coefficients μ (cm^{-1}) of the LSO and BGO scintillation materials as a function of the photon energy E_γ for the three main interaction mechanisms: photoelectric absorption (dashed line), incoherent scattering (dotted line) and pair production (dash-dotted line), and the total attenuation without coherent scattering (solid line). Data are extracted from (Berger et al., 2010) for Lu_2SiO_5 and $\text{Bi}_4\text{Ge}_3\text{O}_{12}$, and multiplied by the respective material density.

- Both LSO and BGO materials are non-hygroscopic, very dense, have a very low Molière radius and a high effective atomic number Z , thanks to lutetium ($Z_{\text{Lu}} = 71$) and bismuth ($Z_{\text{Bi}} = 83$), respectively. Hence, they are suited as absorber. The absorption efficiency of BGO is higher than for LSO at energies below 1 MeV (dominated by the photofraction): its lower density ρ is counterbalanced by its larger Z . For 511 keV photon energy, the total attenuation (without coherent scattering) is 0.82 cm^{-1} for LSO and 0.91 cm^{-1} for BGO; the photoelectric attenuation coefficient is 0.28 cm^{-1} versus 0.40 cm^{-1} , i.e. $\sim 40\%$ larger for BGO. At energies above 1 MeV, where incoherent scattering dominates over the photoelectric effect (one order of magnitude), the total attenuation factors (and also the incoherent scattering and pair production coefficients themselves) are more or less equal for LSO and BGO. At 4 MeV, the pair production is half the Compton attenuation coefficient; above 6 MeV, the first predominates over the latter. The residual photoabsorption efficiency is still $\sim 40\%$ higher for BGO.
- LSO has an internal β^- and γ -ray activity in the energy range below 1 MeV. This does not overlap with the range of interest for PGI, but increases the chance of false coincidences (see next subsection) as well as pile-up with true events. The afterglow of LSO is higher than for BGO (Nassalski et al., 2005). On the other hand, its decay time is much shorter than the BGO one, so that the sustainable detector rate is higher and the overall pile-up probability decreases (assuming common detector sizes).
- The energy resolution of LSO is better, especially for the low energy range, mainly due to the statistical contribution (scales with the number of scintillation photons as $N_{\text{ph}}^{-1/2}$) according to the four times higher light yield (Römer et al., 2015). The lower light self-absorption of BGO (Ramirez et al., 2005) plays a minor role.

2 Compton camera

- The time resolution of a detector made of BGO or LSO is affected by the rise and decay time of the signal, and the light yield. LSO is expected to have a much better time resolution than BGO, at least when coupling the crystal with standard photomultiplier tubes and analogue discriminators. The low afterglow and a relatively small but fast (60 ns) component of the BGO decay time (Moszyński et al., 1981) may notably enhance its performance. Still, LSO is expected to allow a better background suppression for PGI in a clinical pulsed accelerator thanks to its better time resolution. The much shorter decay time compared to that of BGO accounts for lower pile-up probability (better count rate performance), even taking into account larger afterglow and the high internal radioactivity.
- The complex intrinsic radiation background of LSO shows a broad energy spectrum below 1 MeV and stems from the β^- decay of ^{176}Lu (most electrons are stopped inside the material) and subsequent γ -ray cascade of 307, 202 and 88 keV (photons may escape the material with a moderate probability), cf. fig. 2.11 and (Yao et al., 2007).
- The intrinsic spatial resolution, assuming that the interaction is a photoelectric effect, depends on the range of the photoelectron. For the PGI energy range, LSO has a slightly shorter (around 5%) electron range than BGO (Berger et al., 2005). This is almost irrelevant, as it could be balanced e.g. by a 5% larger pixel size in BGO). Note that the Continuous Slowing Down Approximation (CSDA) range of 4 MeV photoelectrons is around 4 mm, which indicates a constraint on the minimum crystal pitch. Anyway, at these energies, the photoelectric absorption is a rather infrequent process (2% absolute photopeak efficiency for 2 cm thick BGO) compared to incoherent scattering (29%) or pair production (8%). In case of a Compton effect, the same conclusions regarding the recoiling electron could apply. If the scattered γ -ray escapes the detector, the intrinsic spatial resolution will not be affected but there will be missing energy affecting the reconstruction algorithm. If the scattered γ -ray is fully absorbed in subsequent processes in the same pixel, there will not be any escape energy, the spatial resolution is not compromised, but the energy resolution can be affected by non-linearities (see next point). The same observations apply in case of pair production, depending on the subsequent absorption of the two annihilation photons.
- Non-linearity effects: a light yield that varies with the energy leads to a non-proportional response spectrum (Dorenbos et al., 1995). This degrades the energy resolution when a photon suffers multiple interactions in the crystal until being fully absorbed. This intrinsic contribution to the energy resolution does not differ too much between LSO and BGO (Ramirez et al., 2005; Zhu, 2012; Römer et al., 2015), in contrast to the statistical one.

In summary, LSO outperforms BGO especially in the light yield and thus on the energy, spatial and time resolution, whereas BGO has much lower price, no internal activity and a better photoabsorption efficiency (a distinguishing feature below 511 keV photon energies, where the photoelectric effect is dominant).

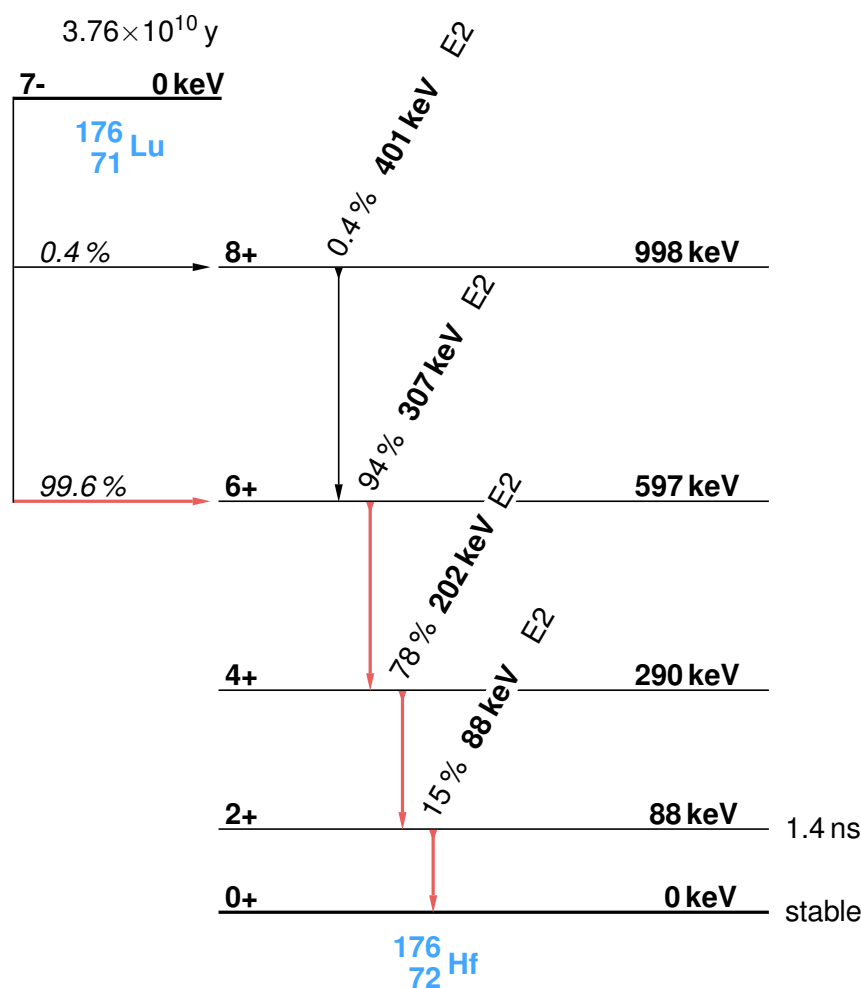


Figure 2.11: Nuclear level scheme of ^{176}Lu . The β^- emission is accompanied by a γ -ray deexcitation cascade. The red arrows mark the predominant decay branch. Adapted from (Nagl et al., 2013).

2.4.2 Block detector properties

The basic detection unit in commercial PET scanners is the block detector. It consists of a square matrix of segmented or pixellated scintillating crystals coupled to four light-sharing Photomultiplier Tubes (PMTs), as depicted in fig. 2.12. The essential feature is the capability to retrieve the pixel where the γ -ray interacts based on the ratio of light collected by each PMT (the modified Anger logic). The block detectors used in this comparative study and their properties² are listed in table 2.2. They are named as LSO2 and BGO1. These names are used when speaking about the concrete detector results, in contrast to LSO and BGO for general features of the scintillation materials.

Are the conclusions drawn in subsection 2.4.1 concerning the expected resolution of the different scintillation materials still valid for segmented or pixellated crystals such as block detectors?

²Thanks to Dr. Hartwig Newiger and Dr. Maciej Kapusta from Siemens Healthcare Molecular Imaging for the information about the block detector construction and geometry (private communication).

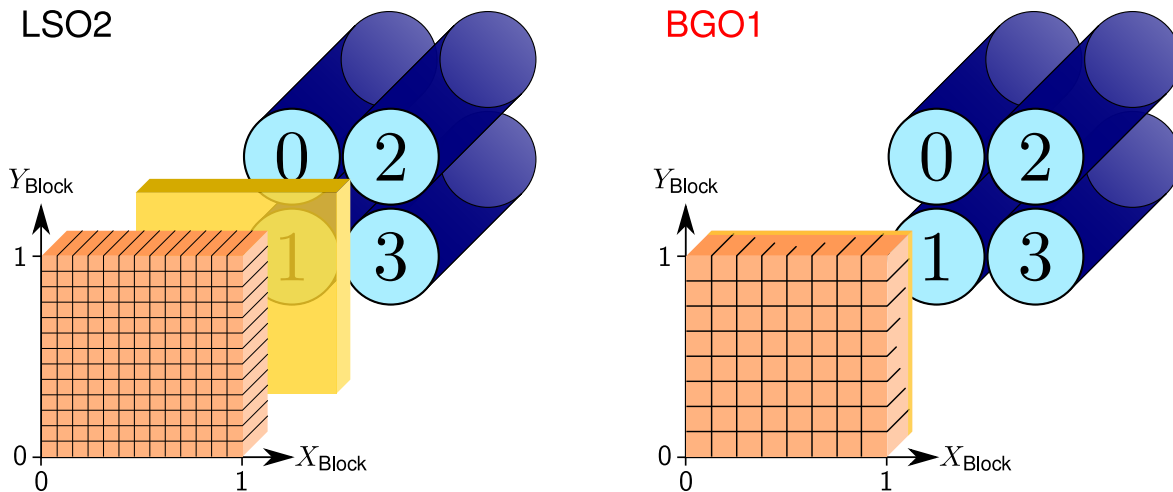


Figure 2.12: Sketch of the LSO2 (left) and BGO1 (right) block detectors with the PMT numbering convention and crystal coordinate system, namely the X_{Block} and Y_{Block} axis (relative position between 0 and 1). Crystals are depicted in orange, PMTs in blue and the light guide in yellow. The actual detector size is given in table 2.2. The labelling convention of the individual pixels of the square matrix $[i, j]$ is: $[0, 0]$ for the pixel at $X_{\text{Block}} = 0, Y_{\text{Block}} = 0$; i and j increase with X_{Block} and Y_{Block} , respectively. Taking BGO1 as example, the edge pixel $[0, 7]$ is at $X_{\text{Block}} = 0, Y_{\text{Block}} = 1$.

- The energy resolution is strongly affected by the spatial resolution. The reason is that different pixels (crystals) have a distinct coupling to the PMTs, reflection loss and scintillation light sharing ratio. Different regions of the photocathode are illuminated depending on the pixel and the response may not be uniform (particularly for edge pixels). In order to obtain a good energy resolution, each pixel has to be calibrated separately to adjust for offset and gain. In other words, the different response (sum signal of the four PMTs) depending on pixel position for the same energy deposit is corrected. Prerequisite is therefore to be able to resolve each pixel. Accordingly, if the pixels are not well separated, an individual energy pixel spectrum will be mixed with neighbour ones and the energy resolution will be degraded.
- The time resolution may also be affected pixel-wise if the PMT high voltages and gains are not close enough to each other. The PMT transit time links to the operating voltage, whereas the energy threshold and time walk depend on the PMT and Preamplifier (PA) gain. A separate trigger on each PMT (instead of a global detector trigger) is needed in order to correct for different PMT transit times or time walk.
- The spatial resolution is mainly affected by the ability of resolving neighbour pixels in the crystal decoding map (flood map), cf. subsection 2.6.2. Assuming a perfect discrimination capability, the lower limit for the spatial resolution is the crystal pitch ($4\text{ mm} \times 4\text{ mm}$ for LSO2). The intrinsic contribution of the photoelectron CSDA range, below 5 mm (Berger et al., 2005), to the spatial resolution is minor compared to the Poisson statistical noise (and the effect of multiple processes, see below). The γ -ray interaction point is recovered from the ratio of scintillation photons collected at

Table 2.2: Comparison of the properties of the LSO2 and BGO1 block detectors.

Detector alias	LSO2	BGO1
Nominal volume (mm×mm×mm)	52.7×52.7×20.0	52.7×52.7×20.0
Granularity	Independent pixels	Segmented crystal
Pixel matrix	13×13	8×8
Pixel dimensions (mm×mm×mm)	4.0×4.0×20.0	6.4×6.4×20.0
Light guide	Coupled to block	Cut into block
Operating voltage	+ 900 V	+ 1350 V
Commercial scanner	Biograph PET/CT	ECAT EXACT 47 PET

Note: the block detectors are from Siemens Medical Solutions USA, Inc. Molecular Imaging Division; a sketch of them is depicted in fig. 2.12. The nominal volume encloses also the small gaps between pixels. The light guide design of BGO1 is as described in (Bailey et al., 2005, fig. 2.22). Spatial dimensions are given as height × width × depth. The acronym CT refers to Computed Tomography.

each separate PMT. As LSO has a higher light yield, the relative statistical noise is lower and the pixels can be resolved better from each other (Humm et al., 2003). In other words, for an equal detector size and acceptable pixel discrimination, LSO based detectors can comprise more pixels per block than BGO, e.g. 169 compared to 64 for standard PET scanners. As the LSO2 crystal pitch is smaller than for BGO1, the spatial resolution is better. Note, however, that one could build a BGO 8×8 block detector with 4×4 mm² crystals, to match the same resolution. Thus, the limitation of BGO is in the number of pixels per block rather than in the crystal pitch (spatial resolution) itself. Indeed, high resolution PET scanners can be also based on BGO, as its higher photofraction reduces the inter-crystal scattering for equal crystal pitch (Chatziioannou et al., 2008).

For these reasons, LSO has gained importance to the detriment of BGO in the PET environment. However, in the PGI environment, where the energy range of interest is above 2 MeV, the number of scintillation photons in a typical event is at least four times higher than in the PET scenario, and the four times lower light yield of BGO might not be a severe drawback concerning the block detector performance.

Furthermore, LSO has a larger afterglow and high intrinsic radioactivity, around 15 kcps for LSO2, cf. table 2.1 and 2.2, with a β^- decay and subsequent γ -ray cascade (see fig. 2.11). This inherent background might have following consequences concerning its use in a Cc:

- Pile-up of true events with intrinsic radiation (minor effect).
- Random coincidences: β^- event in the absorber and interaction of a true prompt γ -ray in the scatterer. This can be minimised if the time resolution of scatterer as well as absorber is excellent, or if the energy threshold of the absorber is set at high energies.
- Trojan coincidences: a β^- interaction in the absorber, a photon of the cascade escaping it and reaching the scatterer. These events are (practically) simultaneous and

2 Compton camera

cannot be rejected with time coincidence filters, only by applying appropriate energy and Compton kinematics filters, or based on timing with respect to the beam bunch.

- The aforementioned problems scale with the size of the Cc. An absorber based on 100 LSO block detectors leads to a global background of 1.5 Mcps and discriminating in real-time false coincidences is challenging. The same applies if one enlarges the detector size instead of increasing the number of detectors, with the additional drawback of higher pile-up probability.

One could argue that, since the range of interest of prompt γ -rays is above 2 MeV, the intrinsic radioactivity of LSO (below 1 MeV, cf. fig. 2.11) can be easily rejected with a high energy threshold on the LSO detector (arming circuit). However, this strategy is misleading and has a huge impact on the efficiency of the Cc. The reason is that the energy filter can only be set on the energy sum (scatterer and absorber) but not on the individual detectors. For example, events with large scattering angles deposit a high energy in the scatterer and low in the absorber. Thus, individual discriminator threshold has to be low on all stages of the camera, and coincident events have to be filtered based on the energy sum. Otherwise, a high individual energy threshold biases the type of events (γ -ray directions) that the camera registers.

A comment should be added regarding the spatial resolution. For 4 MeV prompt γ -rays, direct photoabsorption is unlikely, cf. fig. 2.10. Rather, multiple interaction processes can take place in the same detector until absorbing the whole energy. If incoherent scattering or pair production is followed by photoabsorption (of the scattered γ -ray or annihilation photons) in neighbour pixels, the spatial information of this event is degraded, as neither the detector design nor the modified Anger logic are thought for multiple hits. This has also an effect on the measured energy, which is calibrated independently for each pixel. On the other hand, if the secondary photons escape the detector, the spatial information will not be jeopardised, but the energy of the scattered γ -ray and thus the opening angle of the Compton cone is biased (provided that the incident γ -ray energy is not known in advance).

The complexity and variety of this type of processes can only be covered by MC simulations that include an accurate detector model. However, this exceeds the scope of this thesis. From a qualitative point of view, one can intuit that these multiple interaction processes will be equally common in LSO as well as BGO due to their similar incoherent scattering and pair production attenuation coefficient at 4 MeV, and BGO will absorb better the secondary photons due to its higher photofraction over the whole energy range.

Altogether, multiple interactions in the same pixel until full absorption are acceptable events; if in different pixels, then it leads to false events (to be treated as background); and single interactions with escape energy lead to valid spatial information but energy-biased events. The scientific community is aware about the limitation of a two-layer Cc with photons of unknown and very high energy, where the photoabsorption is rather rare, and has evaluated by means of simulations the noise introduced in the reconstructed images by different types of interactions. It is claimed that the spectral reconstruction (Ortega et al., 2015) is able to

compensate for the missing energy effect. Alternatively, multi-stage (three or more layers) Compton cameras, which do not require a full absorption, have been proposed and are under development (Peterson et al., 2010; Llosá et al., 2013).

Concerning the size of the block detectors, which are optimised for PET energies, one may think of increasing their thickness when applied to PGI. For example, in order to attenuate 70% of the incoming 4.44 MeV γ -rays, the detector thickness should be 4 cm instead of 2 cm.

Another remark is that the difference in the scintillator price (cf. table 2.1) could play only a minor contribution with regard to the overall system costs if these are dominated by e.g. the assembly or electronics.

2.4.3 Electronics and data acquisition

The readout electronics are described in (Hueso González et al., 2014) and vary only slightly among the posterior measurement campaigns. They are based on VERSAmodule Euro-card (VME) and ancillary Nuclear Instrumentation Module (NIM) front-end modules from CAEN (Viareggio, Italy), Canberra (Meriden, USA), iseg (Rossendorf, Germany), Phillips Scientific (Mahwah, USA), Ortec (Oak Ridge, USA) and Wiener (Burscheid, Germany). The operating voltage is controlled via VME with voltage suppliers, model iseg VHQ. The software for data acquisition, called *libCVME2*, is a custom multi-threaded application developed on the ROOT framework of Conseil Européen pour la Recherche Nucléaire (CERN) (Brun and Rademakers, 1997), which provides real-time control of the VME modules and on-the-fly data analysis with graphical feedback. The energy deposit and trigger time stamp is monitored live for each detector.

In detail, the four PMT output signals of each block detector are split actively with a 4-fold transimpedance PA board, cf. fig. 2.13. One branch is fed for trigger generation to a Constant Fraction Discriminator (CFD), model GSI CF8000. The second branch is delayed and fed to a Charge to Digital Converter (QDC), model V965. A Time to Digital Converter (TDC), model V1290A, monitors the trigger signal generated by the CFD as well as the accelerator Radio Frequency (RF), used as time reference of the bunch arrival in the case of pulsed accelerators. A custom logic module is programmed on an Field Programmable Gate Array (FPGA), model V1495. On the one hand, this FPGA generates the event trigger for the TDC as well as the integration gate for the QDC module, provided that no veto signal is present. The veto signal is generated by the busy output of the QDC module. On the other hand, the FPGA has integrated scalers to monitor the trigger rate with and without coincidence of the veto, in order to estimate the system dead time. A controller, model V1718, handles the communication between a desktop computer and the VME bus.

After 32 gates, an interrupt signal is generated by the QDC (almost full buffer signal). Subsequently, the computer reads out the TDC and QDC data via the VME bus. Afterwards,

their buffers are cleared and the module event counter is reset for synchronising all the modules. During data readout, the logic module is blocked with an extra veto signal generated by the controller and no additional gates are generated. This way, potential fake events due to the interference of the VME activity with the detector signals are safely excluded.

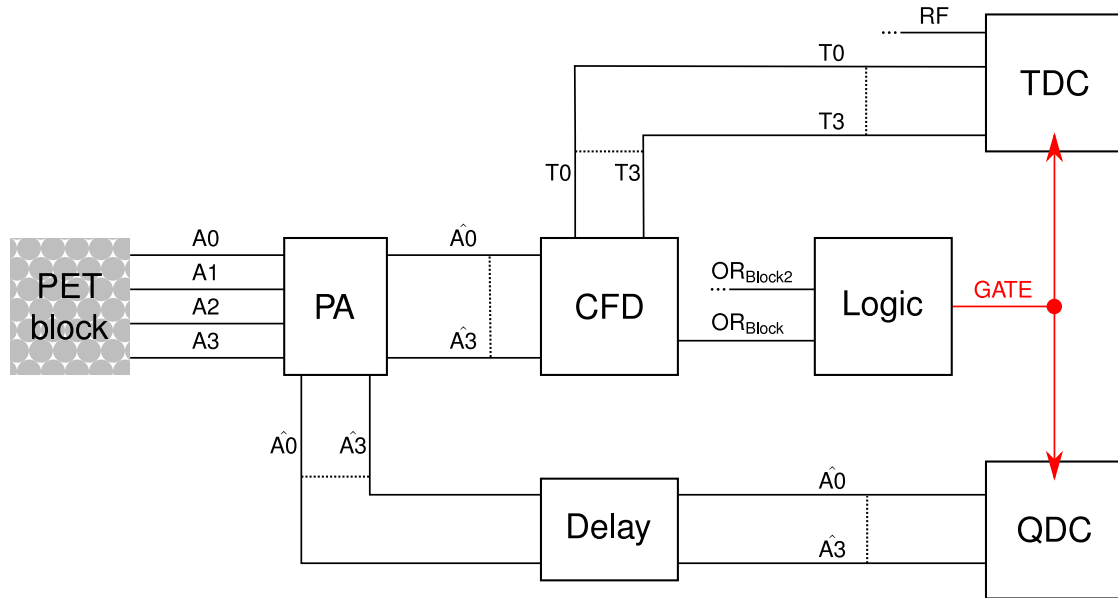


Figure 2.13: Simplified sketch of the front-end readout electronics used for the measurements with PET block detectors. Analogue detector signals (A) are amplified and actively split (\hat{A}) by the PA board. One branch is fed into a CFD, the other is delayed and plugged into a QDC. A TDC monitors the CFD trigger output (T) as well as the accelerator RF. OR_{Block} refers to the logic OR of the four trigger outputs (T). When an OR signal from any block detector is active, the logic module generates an integration gate for the QDC and a trigger for the TDC.

2.4.4 High efficiency Compton camera setup

The BGO block Compton camera (BbCc) is a setup comprising two BGO block detectors from commercial PET scanners. The blocks are arranged face-to-face and the distance between the respective crystal centres is ~ 6.5 cm. The aforementioned BGO1 detector is used as absorber. As scatterer, another BGO block detector, named as BGO4, which has a smaller crystal pitch, is deployed. It comprises a crystal matrix of 8×8 as described in table 2.2 for BGO1, but with a smaller front face. The nominal volume is $35.0 \times 37.5 \times 30.1$ mm³ and the pixel dimensions are $3.8 \times 3.5 \times 30.1$ mm³. It is used in the ECAT Exact HR+ scanner. Whereas the aluminium sealing of LSO2 and BGO1 has the shape of a truncated pyramid, the housing of BGO4 is like a truncated cake slice (up and bottom faces are parallel), cf. fig. 2.16 (left).

The reason behind the relatively high efficiency of this setup, concerning single events, is the dependence of the Compton attenuation coefficient σ on ρ/E_γ , cf. section 2.1. A very dense (and thick) scatterer (BGO has a large ρ) is chosen to balance the high energy E_γ expected

in the PGI field. Compton cameras developed for low energies comprise scatterer planes with low density, which have a poor incoherent scattering efficiency at the high energy field. Increasing just the detector area seems not an acceptable solution to improve the efficiency: alternative materials are needed. To give some numbers, the Compton interaction efficiency $\epsilon_\sigma = 1 - \exp(-\sigma h)$, where h is the scatterer thickness, for BGO4 and 4.4 MeV γ -rays yields 40 % compared to 20 % for each stage of the Cc described in (Polf et al., 2015).

2.5 Experimental setup

2.5.1 Accelerators

The detectors described in table 2.2 are tested at the Electron Linear accelerator for beams with high Brilliance and low Emittance (ELBE) of HZDR (Hueso González et al., 2014), and at the superconducting cyclotron Accélérateur Groningen ORsay (AGOR) of Kernfysisch Versneller Instituut - Center for Advanced Radiation Technology (KVI-CART), in the same experimental campaign as in (Golnik et al., 2014). The BbCc setup is tested at ELBE and at the clinical isochronous cyclotron C230 of UPTD.

Setup and beam settings at each of these accelerators are compared in table 2.3. The research facilities are appropriate for characterising the detectors in a radiation field with similarities to the clinical scenario.

Table 2.3: Comparison of the characteristics of the photon radiation field produced at the three different accelerators.

Accelerator name	ELBE	AGOR	C230
Location	HZDR	KVI-CART	UPTD
Accelerator type	Superconducting LINAC	Superconducting cyclotron	Isochronous cyclotron
Accelerated particles	Electrons	Protons	
Used beam current	~ 1 nA	~ 10 pA	~ 40 pA
Kinetic energy	12.5 MeV	150 MeV	[70, 170] MeV
Bunch frequency f_{bunch}	13 MHz	55 MHz	106 MHz
Bunch width	~ 5 ps	~ 400 ps	~ 2 ns
Target material	Nb	Graphite	PMMA
Target size	2 μm foil	10 cm \times 10 cm \times 30 cm	5 cm \times 5 cm \times 10 cm
Photon energy range	≤ 12.5 MeV	$\lesssim 8$ MeV	
Photon energy spectrum	Continuous	Quasi-continuous + prominent γ -ray lines	
Detected radiation flux	10^5 s $^{-1}$	10^5 s $^{-1}$	5×10^4 s $^{-1}$
Production process	Prompt bremsstrahlung X-rays	Prompt nuclear reactions (γ -rays)	
Background fraction	Very low	High: neutrons, material activation	
Measurement campaigns	11/2012, 11/2013, 02/2014	07/2013	02/2015
Scintillators used	LSO2, LSO2-BGO1-BGO4	LSO2-BGO1	BGO1-BGO4
Rationale	Timing, spatial at high energies	Test at research facility	Test at clinical scenario

Note: the table presents the parameters set up in the respective experiments. The LSO2 detector is also used in (Hueso González et al., 2014), the BGO1 in (Kormoll et al., 2013). The target at UPTD is Polymethyl Methacrylate - $[\text{C}_5\text{O}_2\text{H}_8]_n$ (PMMA), also known as Plexiglas, and has a density $\rho_{\text{PMMA}} = (1.18 \pm 0.01) \text{g/cm}^3$. This organic glass is chosen due to the content of elements present in human tissue. The acronym LINAC stands for Linear Accelerator. The AGOR cyclotron is isochronous.

ELBE is a linear electron accelerator at HZDR, used to provide bunched bremsstrahlung photons with a maximum energy of 12.5 MeV. A comprehensive description of the facility is given in (Schwengner et al., 2005). It is a good testing platform for the block detectors concerning timing resolution as well as spatial resolution for different photon energy ranges:

- In a clinical proton cyclotron, the emitted prompt γ -rays are also bunched with the accelerator frequency, namely 106 MHz for the C230 (Verburg et al., 2013) compared to the 13 MHz at ELBE (Hueso González et al., 2014).
- The energy range of the bremsstrahlung photons is comparable to the one expected for prompt γ -rays in a clinical proton beam (several MeV) and allows testing detectors in an energy range not accessible using common radioactive sources.
- The electron bunch width (Schwengner et al., 2005) is about 5 ps, thus allowing a precise measurement of the intrinsic detector time resolution. In contrast, in the C230 accelerator, the proton bunch spread is ~ 300 ps at 230 MeV proton energy and up to 2 ns at 100 MeV (Hueso González et al., 2015b).
- The beam intensity can be adjusted over several orders of magnitude. This is useful for testing the stability of the detectors depending on the trigger rate.

AGOR is a superconducting cyclotron, which provides bunched protons with energies up to 190 MeV. Other ions can also be accelerated, but up to lower energies (per nucleon). In this experiment, a fixed proton energy of 150 MeV is used. A detailed description of this accelerator is given in (Brandenburg et al., 2007). It has many similarities to the clinical proton cyclotron and is therefore indicated to test all properties of the block detectors with phantom experiments:

- The emitted prompt γ -rays are also correlated to the accelerator frequency: 106 MHz for the C230 compared to the 55 MHz at AGOR for 150 MeV protons.
- 150 MeV is a relevant proton energy in clinical therapy, and the nature of prompt γ -rays and neutron background production is comparable to the conditions in the clinical environment.

C230 is a clinical proton cyclotron present at UPTD. The experimental area at this center, comprising a horizontal fixed beam line, resembles best the clinical irradiation conditions. It is one of the most common types of proton therapy accelerators (PTCOG, 2014). The bunch repetition rate of 106 MHz results from the periodic acceleration of protons in the resonator gaps of the isochronous cyclotron, controlled by the high voltage. This alternates with the accelerator RF. It should be noted that, in the current experiments, the setup is not tested in the gantry treatment room but in the experimental room (horizontal fixed beam line), that small beam currents (40 pA at nozzle exit) are deployed and no Pencil Beam Scanning (PBS) is applied (out of scope of this work). In contrast, clinical treatments in PBS

mode (Perali et al., 2014) use beam currents of ~ 2 nA at nozzle exit (instantaneous current), i.e. 1.25×10^{10} protons delivered per second or 118 protons per RF cycle (9.4 ns period).

2.5.2 Detector setup

The detector setup for the comparison of LSO and BGO is described in figs. 2.14 and 2.15. For the Cc arrangement, it is described in fig. 2.16. Note that at ELBE, the detectors are irradiated directly by the focused bremsstrahlung beam. In contrast, at AGOR and C230, the proton beam irradiates a target and part of the secondary prompt γ -rays (emitted in all directions) reach the detectors, which are not located on the beam axis.

2.5.3 Trigger regime

- At ELBE, each block is measured separately as standalone setup covering the whole beam spot. The electron current (flux of bremsstrahlung photons, which are forward focused) is adjusted so that the detector trigger rate is about 10^5 per second.
- At AGOR, both LSO2 and BGO1 are used simultaneously as part of a Cc setup, but with individual trigger on each block (no coincidence conditions). The trigger rate at each block, which is placed ~ 30 cm away from the center of the target (beam axis), is around 10^5 s⁻¹.
- At C230, the BGO4 and BGO1 blocks are measured in parallel, but without coincident trigger condition. BGO4 is placed about 20 cm from the beam axis and the measured rate is around 7×10^4 s⁻¹. BGO1 is ~ 5 cm further away and registers 6×10^4 s⁻¹.

Although the energy range of interest for PGI is above 2 MeV, the discriminator threshold at each detector has to be kept low (on the 100 keV scale) because valid Compton events may deposit also small energies in the absorber. Coincidences can be built based on the trigger time stamp and the correlation to the RF, and a 2 MeV sum energy threshold can be then applied in the data processing.

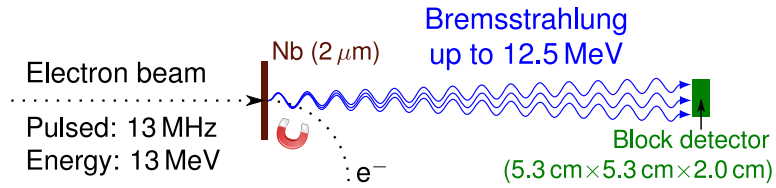


Figure 2.14: Experimental setup at the ELBE accelerator. Electrons (dotted arrow) accelerated up to a total energy of 13 MeV in 13 MHz bunches – corresponding to 77 ns bunch separation – interact with atoms of a Niobium foil. Bremsstrahlung photons (continuous spectrum up to 12.5 MeV) are radiated promptly (and forward-focused) as a result of the deflection of the electrons by the electric field of the nuclei, and are registered by the block detector (LSO2, BGO1 or BGO4).

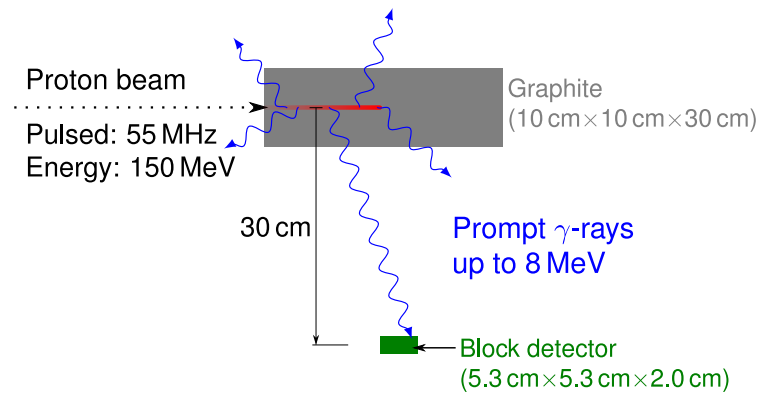


Figure 2.15: Experimental setup at the AGOR accelerator. Protons (dotted arrow) with 150 MeV kinetic energy in 55 MHz bunches – corresponding to 18.2 ns bunch separation – penetrate into a graphite target. As a result of nuclear interactions, γ -rays are radiated promptly in 4π , with a quasi-continuous spectrum and prominent characteristic lines, and measured by the block detector LSO2 or BGO1 (dynamic range up to 8 MeV).

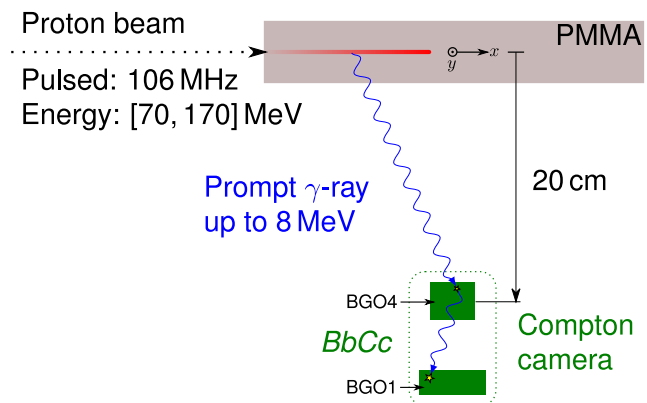
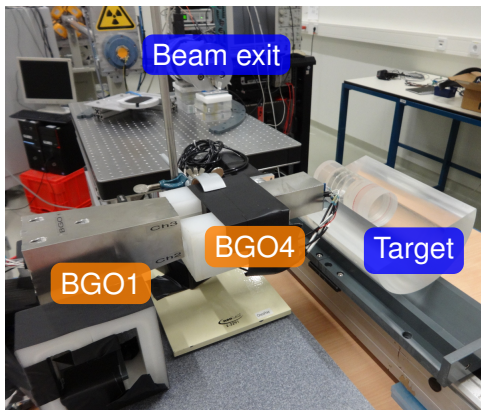


Figure 2.16: Photo (left) and schematic top view (right) of the BbCc setup at the experimental room of UPTD (C230 accelerator). The proton pencil beam, with an energy between 70 and 170 MeV, and a bunch repetition rate of 106 MHz, irradiates a homogeneous PMMA target, and the BbCc setup (block detectors BGO1 and BGO4) measures the prompt γ -rays (dynamic range up to 8 MeV). Real aspect ratio is preserved.

2.6 Methods

An extended calibration procedure for block detectors is mandatory to obtain a good energy, spatial and time resolution. The main steps are enumerated below and detailed in the corresponding subsections.

- The four PMT output channels are recorded by the QDC.
- Different gain and signal offset of each PMT are corrected for matching all spectrum shapes.
- A preliminary energy calibration is carried out for each corrected PMT spectrum.
- The crystal decoding map, also known as flood map, is generated.
- The flood map is segmented in regions corresponding to each pixel.
- Energy sum spectra are drawn for each pixel and recalibrated to account for the pixel-dependent light coupling. The dependence of the pulse height distribution on the interaction position is a well-known effect in detectors based on Anger logic. It is due to the different light emission (crystal inhomogeneities), the distinct light coupling to the PMT and also the differences among PMT gains.
- Time spectra of each pixel are corrected for transit time effects among PMTs.
- Global time spectrum is corrected for energy dependent time walk.

2.6.1 Energy calibration

For the energy calibration, a measurement with a radioactive source like ^{22}Na or ^{60}Co , with high activity and at a distance large enough to ensure a (more or less) homogeneous irradiation of all pixels, is performed. Note that the discriminator threshold should be low and similar for all PMT channels. The procedure is divided in two steps:

1. **PMT gain and offset adjustment.** Since the irradiation is homogeneous, the histogram of the charge recorded by the QDC, cf. fig. 2.17 (left), should have the same shape for each PMT (except for an offset and gain factor). A custom software tool, named as *HistStretcher*, allows the overlap of histograms and interactive adjustment of the histogram offset and gain. Thanks to the graphical real-time feedback, one can fine-tune until the four spectra match in shape, as seen in fig. 2.17 (right). The difference in gain among channels is already small in fig. 2.17 (left), as the PMT voltage is adjusted through the rear panel of the block detector. This provides four screws regulating the voltage division at each tube. These screws are adjusted iteratively so that the width of the distributions (in channels) is more or less similar, and the remaining differences are corrected by the aforementioned gain matching.

A provisional energy calibration of the corrected histograms is performed empirically. Since the scintillation light of each event is shared among the four PMTs, and this ratio and the light coupling vary from pixel to pixel, one should not expect to see a photopeak in these histograms (if all pixels are irradiated). But this does not mean that this preliminary calibration is done blindly. The guideline is the energy sum spectrum. It is obtained by summing for each event the calibrated energy, cf. fig. 2.17 (right), among the four PMT channels. The channel calibration can be refined until the resulting sum spectrum, cf. fig. 2.18 (left, no spatial filters), lies roughly in the expected energy range and the pedestal is located at 0 MeV. From the obtained calibrated energies, the crystal decoding map can be calculated (see subsection 2.6.2). One has to keep in mind that, rather than providing the final energy calibration, the goal of this step is to compensate for the different gain (and offset) of each tube, and to obtain a symmetric flood map with a clear separation between pixels, a precondition for the next step.

- 2. Energy calibration of the individual pixels.** After the spatial segmentation of the flood map is performed, cf. subsection 2.6.2, one can draw the energy sum spectrum of the detector for different regions (pixels), as depicted in fig. 2.18 (left). One can see that the selected pixel spectra have a similar shape but different offset or gain (as before), due to the distinct light coupling. In order to correct for this additional effect, separate energy spectra are drawn for every pixel and individually recalibrated with an automatic template matching procedure. The *HistStretcher* software tool allows refining by hand the automatic procedure, which is of interest e.g. for the energy spectra of edge pixels, which differ significantly from the rest. The result of this recalibration is shown in fig. 2.18 (right).

The energy information is relevant for analysing the photopeak resolution for discrete γ -ray lines. In principle, the energy resolution is different for each pixel, but a global detector resolution can be also obtained by summing up among all pixel regions, cf. fig. 2.18 (right). Apart from that, the energy scale is valuable for characterising the spatial and timing resolution for different ranges of interest:

- PET range: $[0, 1]$ MeV. This covers the typical energy region of 511 keV photons, created by the annihilation of positrons with electrons (PET imaging). Standard block detectors from medical PET scanners are well characterised and optimised for these energies. This energy range is accessible with common radioactive sources.
- Middle range: $[1, 2]$ MeV. This intermediate range is above the typical energies at PET imaging, but is still accessible with radioactive photon sources.
- PGI range: ≥ 2 MeV. It is the range of interest in PGI due to characteristic prompt γ -ray lines with a strong correlation with the particle range (Verburg and Seco, 2014). This region is not accessible by means of common radioactive sources.

When the block detector is deployed as absorber of a Cc (high energy deposit), the middle and high range are of special interest. It is worth remembering that the energy scale, labelled

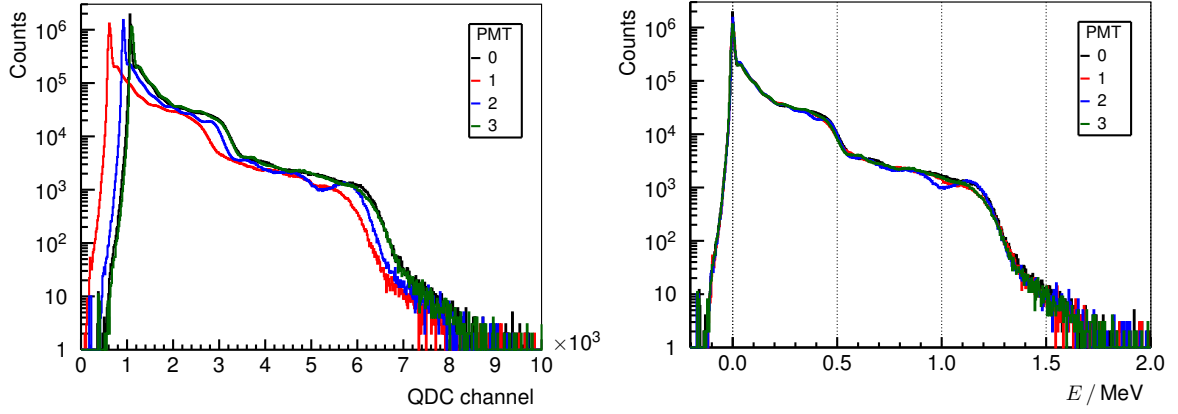


Figure 2.17: Left: response spectrum of the four PMTs of the BGO1 detector when irradiated with a ^{22}Na source. Right: calibrated energy spectra after regulating offset and gain to match their shapes. Vertical scale is arbitrary.

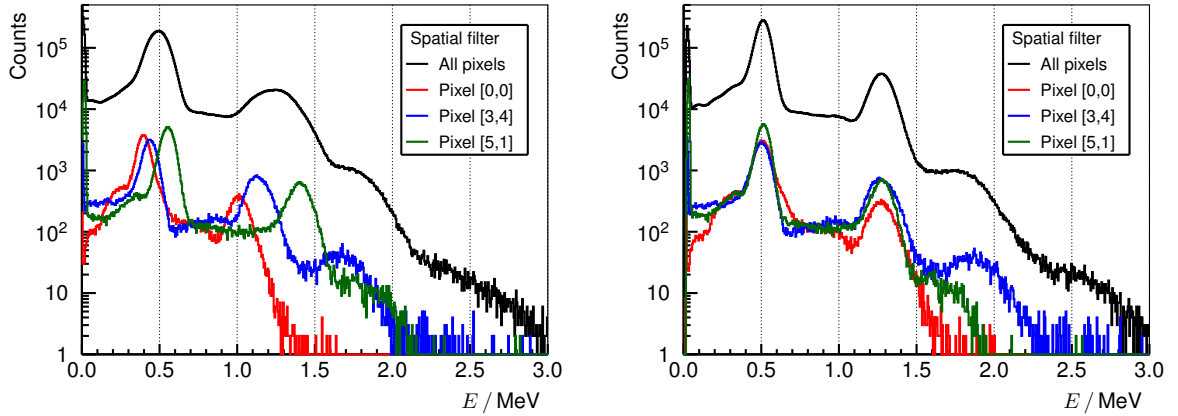


Figure 2.18: Left: event-wise sum of the energy recorded at each PMT of the BGO1 detector, as depicted in fig. 2.17 (right). Different energy spectra depending on the spatial cuts are superimposed. Right: event-wise energy sum after pixel-wise recalibration of the energy spectra of the left plot.

as E/MeV for the sake of clarity, does not refer to incident photon energy but to the energy deposit in the detector. The vertical axis of all 1D histograms is chosen arbitrarily and is labelled as *Counts*. 2D histograms are drawn as heat maps, that contain a color palette on the right hand side with an arbitrary scale. Its label (*Counts*) is omitted for compactness.

The relative energy resolution $R_E(E_\gamma)$ is determined as the FWHM Σ_E of the Gaussian shaped peak (photopeak or SDEP) of the acquired pulse height spectrum divided by the centroid position E_γ . A linear background subtraction of the detector response spectrum is previously applied.

$$R_E(E_\gamma) = \Sigma_E/E_\gamma \quad (2.22)$$

2.6.2 Spatial calibration

The flood map is a 2D histogram of the spatial coordinates $(X_{\text{Block}}, Y_{\text{Block}})$ of the interaction points of the γ -ray inside the pixellated or segmented block detector, retrieved based on the modified Anger logic. It can be obtained from the relative intensities measured at the four light-sharing PMTs (fig. 2.12). The standard center of gravity equation (Stonger and Johnson, 2004) is used to calculate these (relative) crystal coordinates $X_{\text{Block}} \in [0, 1]$, $Y_{\text{Block}} \in [0, 1]$:

$$X_{\text{Block}} = 0.5 + 0.5 \times \frac{E_2 + E_3 - E_0 - E_1}{\sum_{i=0}^3 E_i} \quad (2.23)$$

$$Y_{\text{Block}} = 0.5 + 0.5 \times \frac{E_2 + E_0 - E_3 - E_1}{\sum_{i=0}^3 E_i} \quad (2.24)$$

where E_i is the (calibrated) energy measured at the channel (PMT) i , cf. fig. 2.17 (right).

The crystal decoding map is drawn, cf. fig. 2.19 (left), and divided into regions corresponding to each pixel (crystal). This segmentation is done automatically with the neighbour standard deviation algorithm (Wei et al., 2013). The result (after additional distortion correction, see below) can be seen in fig. 2.19 (right). Energy and time histograms are then drawn for each region separately for a refined pixel-wise recalibration.

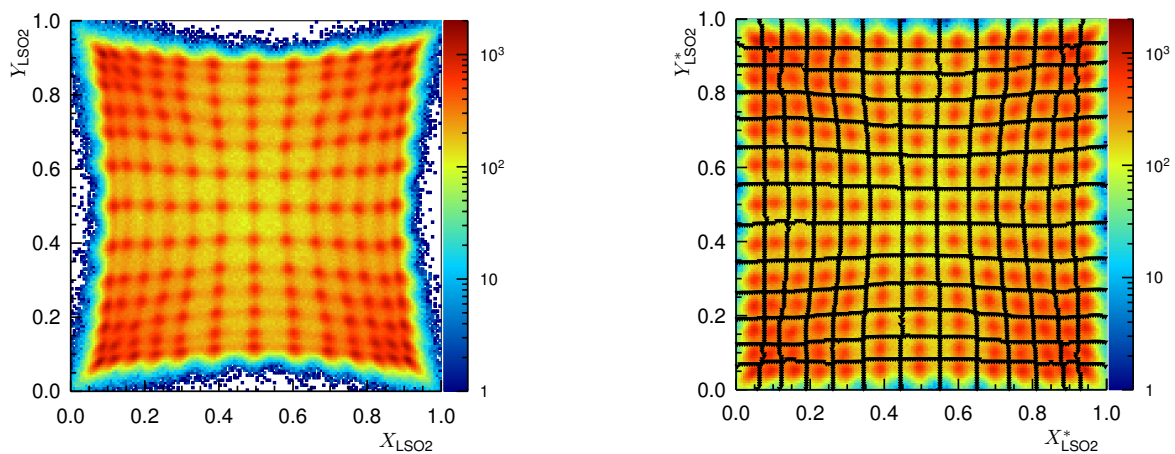


Figure 2.19: Left: example of a flood map of the LSO2 detector when irradiated homogeneously by a ^{60}Co source, calculated according to eqs. 2.23 and 2.24. Right: the flood map distortion correction is applied with the empirical parameters $p = 0.48$, $q = 0.44$, cf. eqs. 2.25 and 2.26, adapted from (Cui et al., 2013). The black markers are the pixel boundaries obtained with the automatic segmentation method (Wei et al., 2013).

Distortion correction In general, the flood map of block detectors does not exhibit a uniform distribution of pixels (hot spots in the heat map). The reason is the proportional re-

sponse (center of gravity equation) assumed by eqs. 2.23 and 2.24, that neglects non-linear effects. As a result, a distorted map is generated with the so-called pincushion shape, see fig. 2.19 (left). This shape is especially pronounced for the LSO2 detector: all pixels are independent (it is not a segmented crystal like BGO1) and a light guide distributes all scintillation photons to the four PMTs. In some cases, before performing the automated segmentation, a distortion correction (Cui et al., 2013) is applied to recover a more uniform and squared shape (X_{Block}^* , Y_{Block}^*). This takes into account the non-linear relationship between interaction position and light sharing ratio.

$$X_{\text{Block}}^* = 0.5 + 0.5 \times \frac{E_2 + E_3 - E_0 - E_1}{\sum_{i=0}^3 E_i} \times \frac{(E_2 + E_0) + p(E_3 + E_1)}{(E_2 + E_3) + q(E_0 + E_1)} \times \frac{(E_3 + E_1) + p(E_2 + E_0)}{(E_0 + E_1) + q(E_2 + E_3)} \quad (2.25)$$

$$Y_{\text{Block}}^* = 0.5 + 0.5 \times \frac{E_2 + E_0 - E_3 - E_1}{\sum_{i=0}^3 E_i} \times \frac{(E_2 + E_3) + p(E_0 + E_1)}{(E_2 + E_0) + q(E_3 + E_1)} \times \frac{(E_0 + E_1) + p(E_2 + E_3)}{(E_3 + E_1) + q(E_2 + E_0)} \quad (2.26)$$

The parameters p and q appearing in these equations are adjusted empirically. For $p = 1$ and $q = 1$, one falls back to eqs. 2.23 and 2.24, which depend linearly on the energies E_i . Note that the aim is not to obtain a perfectly square pixel distribution, since the pixel identification is done with the segmentation method and not with a rectangular grid. Still, the distortion correction optimises the outcome of the segmentation method, particularly for the edge pixels, which are originally compressed in very few bins, cf. fig. 2.19 (left).

Pixel decoding factors One way of determining the resolution with which one pixel is resolved from the neighbour ones is to measure the peak to valley ratio $P2V$ in the flood map (Ramirez et al., 2009). Alternatively, one could use as figure of merit the resolution R , defined as the distance to the nearest neighbour pixel centroid divided by the spatial FWHM Σ of the pixel peak. This is measured in a 1D projection of the flood map along a selected row or column of the crystal matrix.

2.6.3 Time calibration

The rise time of the detector signal extracted from the anode (scintillator coupled with PMTs and a custom PA box) is ~ 5 ns for LSO2, and ~ 10 ns for BGO1 and BGO4. This signal is fed to the CFD, whose internal delay line is 2 ns and 6 ns, respectively. Each anode channel is triggered separately. A copy of the input signal is delayed and fed to the QDC, cf. fig. 2.13. The correction of transit time effects and time walk can be done for each PMT separately. Alternatively, one can use a pixel-wise delay correction and a global time walk correction.

Pixel delay calibration Based on the ELBE experiment (Hueso González et al., 2014), where the intrinsic time resolution of the detector can be measured very accurately, the effect of different transit times for each PMT can be corrected. Another strategy is to perform this correction for each crystal based on the fast OR signal of the four PMT triggers and the flood map. The time difference between accelerator bunch arrival and detector trigger is drawn for each crystal with an energy threshold of 2 MeV. An automatic procedure locates then the centroid of the timing peak. A reference pixel is chosen, namely the one with the smallest value of the peak centroid. The time stamps of the rest of the pixels are corrected for all events with a pixel-wise offset in order to match the centroids of the respective timing histograms with the reference one.

Slewing correction 2D histograms of energy deposit over time difference (between detector and accelerator bunch) are acquired at ELBE, and are used to obtain a time walk correction (also known as slewing correction), as described in (Hueso González et al., 2014).

2.6.4 Error analysis

The measurement of the energy, spatial and time resolution after this complex calibration procedure is done by Gaussian fitting with background subtraction. Although the errors associated to the fitting algorithm are well known, they do not reflect the uncertainties of the manual as well as automatic calibration one may accumulate at each of these steps. Depending also on the experience of the person performing the calibration or the number of iterative refinements, the final resolution varies moderately.

Moreover, the energy resolution at different γ -ray lines is obtained from separate measurement campaigns. The same detectors are used, but part of the electronics, the operating voltage, detector load and electronics throughput, radiation background, orientation with respect to the Earth's magnetic field, and temperature are slightly different. This makes a trustworthy estimation of the underlying systematic errors challenging and to some extent subjective. This has to be kept in mind when analysing the results of different experiments in combined graphics. Furthermore, PMT gain stabilisation (Stein et al., 2015) is not applied.

A final comment is that the measurements are performed in non-monitored temperature conditions, although it is well known that temperature variations alter the properties of the scintillators (Payne et al., 2014) described in subsection 2.4.1.

2.6.5 Systematic measurement program

To test the BGO4-BGO1 Compton imaging setup, an experimental campaign at the proton beam of UPTD is designed. Previously, the BbCc is characterised extensively in the laboratory (at HZDR and UPTD) with point-like photon sources: ^{22}Na (511 and 1275 keV), ^{60}Co (1173 and 1333 keV) and ^{13}C (6130 keV). Spatial shifts of these radioactive sources are

performed and the respective BP images are analysed. A ^{22}Na line source measurement is acquired by a periodic uniform motion of the point source. Furthermore, the spatial and time resolution of each block detector (BGO1 and BGO4) is measured as a function of photon energy at the ELBE accelerator, in the same experiment where BGO1 is compared to LSO2 (absorber choice). The energy resolution is also measured for different photopeaks between 511 keV and 4.4 MeV. For the sake of clarity, most resolution results of the BGO4 detector are not reported explicitly due to their similarity to BGO1.

The camera is then tested at the horizontal pencil beam line (experimental area, no PBS) of UPTD. A PMMA target is irradiated with low beam currents compared to therapy conditions, since the employed acquisition system allows only a relatively small throughput. The BbCc is placed perpendicularly to the beam axis at a distance of 20 cm, cf. fig. 2.16, and detects the prompt γ -rays. The homogeneous target is constructed out of cylindrical PMMA slices of 5 cm diameter and different thicknesses, and is mounted on a linear stage with remote control.

Three types of experiments are carried out for exploring the responsiveness of the camera to range deviations:

1. Shifts of a 2 cm thick PMMA target along the beam axis for 70 MeV protons.
2. Increase of the target thickness in 2 cm steps for 160 MeV protons.
3. Variation of the beam energy from 70 to 170 MeV in 10 MeV steps for a 40 cm thick target.

Each measurement point lasts around 15 min with a continuous beam current of ~ 40 pA. The alignment of the detectors is performed with a self-levelling cross-line laser and the precision of the distance between detectors is not better than 3 mm.

2.7 Results – absorber choice

2.7.1 Energy resolution

Fig. 2.20 (left) depicts the detector response spectrum of the LSO2 and BGO1 block detectors to a ^{22}Na source. By simple inspection, LSO2 has a better energy resolution. Fig. 2.20 (right) compares two energy spectra of BGO1 and LSO2 at the C230 and AGOR facilities, respectively. Both provide a pronounced γ -ray line at 4.44 MeV, which can be seen together with SDEP. Unfortunately, no absolute efficiency calibration is available at these experiments and the relative height of the peaks of fig. 2.20 cannot be compared quantitatively.

Fig. 2.21 compares the energy resolution R_E , cf. eq. 2.22, at different characteristic γ -ray lines for both block detectors: 0.511 and 1.275 MeV of a ^{22}Na source, 1.173 and 1.333 MeV of a ^{60}Co source, 2.224 MeV from the capture of thermal neutrons on the hydrogen nucleus

2 Compton camera

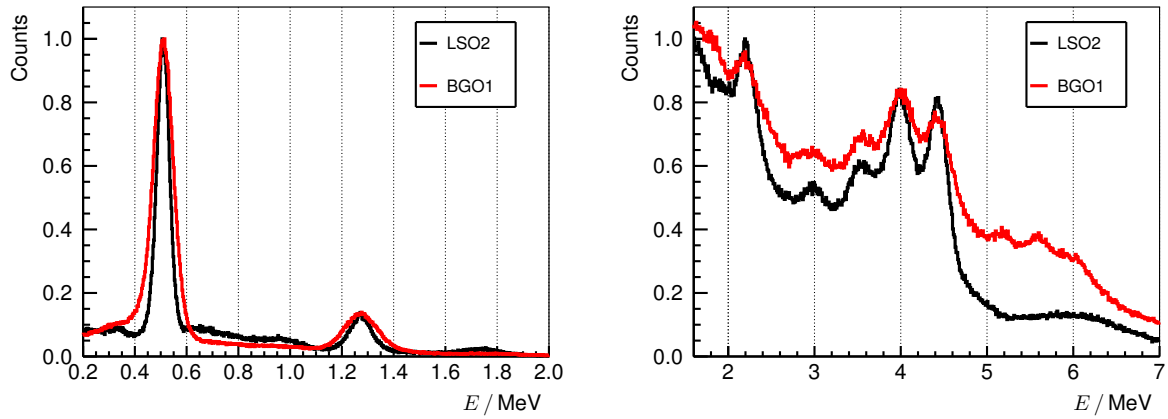


Figure 2.20: Left: detector response spectrum of the LSO2 block detector (black line) for a ^{22}Na source compared to the BGO1 detector (red line). Respective maxima are normalised to one. For LSO2, the intrinsic background is not visible as the source activity is significantly higher. Right: analogous energy spectrum at the prompt γ -ray field at AGOR with 150 MeV protons irradiating a graphite target for the LSO2 and at C230 with a 100 MeV beam impinging a PMMA target for the BGO1. Histogram maximum is normalised to one for the LSO2 detector; the BGO1 spectrum is scaled to match the height of the single escape peak of the LSO2.

($^1\text{H} + n_{\text{th}} \rightarrow ^2\text{H} + \gamma$) at AGOR/C230, and also 4.440 MeV prompt γ -rays as well as the SDEP.

Note that the measurement of the energy resolution is particularly difficult between 3.4 and 4.4 MeV as photopeak, its Compton edge as well as SDEP overlap considerably, cf. fig. 2.20 (right). A Gaussian mixture fit has to be applied together with linear background subtraction. This is also the reason for higher error bars at some of these points. It should be taken into account that at 4.4 MeV, the pair production is dominant (see fig. 2.1) and non-linearities have a significant impact on the energy resolution. For example, the 511 keV annihilation photons interact also via incoherent scattering, and complicated structures may arise within the SDEP region and degrade the peak shape. The detector response to these high γ -ray energies has to be modelled based on dedicated MC simulations (Römer et al., 2015).

From fig. 2.21, it is concluded that LSO2 has a better energy resolution than BGO1 across the whole energy range. Nevertheless, the differences are much lower in the high energy range. This points out that LSO2 is significantly better at the PET scenario, below 1 MeV. On the other hand, for the PGI scenario, above 2 MeV, the performance gap is less pronounced (below two percentage points), so that the still large material price difference does not correlate necessarily to a much better detector quality.

What is the reason for the comparable resolution at high energies? The relative energy resolution R_E depends on two independent contributions: statistical and intrinsic. The first one depends on the light yield and is proportional to the inverse square root of number of (collected) scintillation photons, according to Poisson statistics. The second one is due to non-linearity effects (Dorenbos et al., 1995) and is dependent on the crystal structure. At low

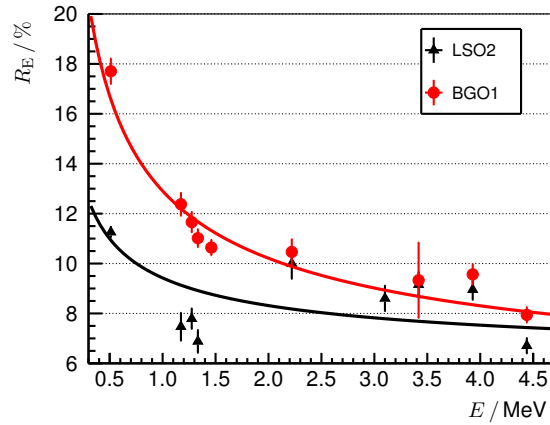


Figure 2.21: Relative energy resolution R_E , see eq. 2.22, of the LSO2 (black line) and BGO1 (red line) block detectors as a function of the energy deposit E . The results from various photopeaks obtained at different experiments are combined. The empirical fit to the experimental points is $R_E(E) = (3.8 \pm 0.3)\%/\sqrt{E/\text{MeV}} + (5.6 \pm 0.3)\%$ for LSO2 and $R_E(E) = (9.2 \pm 0.5)\%/\sqrt{E/\text{MeV}} + (3.7 \pm 0.4)\%$ for BGO1.

photon energies, the range of usual radioactive sources or the case of PET, the statistical contribution dominates over the intrinsic one. As LSO has a four times higher light yield than BGO, its energy resolution is better. At high photon energies, e.g. the PGI energy range, the number of scintillation photons is larger, so that the statistical contribution is smaller and the intrinsic contribution starts to dominate. The intrinsic factor is comparable between BGO and LSO (Balcerzyk et al., 2000; Moszyński et al., 2004; Römer et al., 2015), see also offset parameter in the fit of fig. 2.21. This explains their comparable performance concerning energy resolution at the PGI energy range.

2.7.2 Spatial resolution

Fig. 2.22 depicts the flood maps of the LSO2 and BGO1 block detectors for different energy ranges of interest. One can clearly identify that the pixel decoding capability increases with the energy range. For higher γ -ray energies, the relative energy error R_E is lower. Thus, as the spatial coordinates depend on the measured energy, cf. eqs. 2.23 and 2.24, one can distinguish better between pixels. Note that the higher intensity of some pixels is due to the non-uniform irradiation of the crystals: the photons at ELBE are focused (in contrast to 4π emission at AGOR and C230) and the beam spot is smaller than the front face size of the block. There are additional effects like varying energy threshold depending on pixel location or different amount of bins covered by a certain pixel in the flood map, which explain the different intensities in the flood map even with a perfectly homogeneous irradiation.

By simple inspection, BGO1 shows a worse spatial resolution than LSO2 (broader spots in the map). Nonetheless, the pixels are resolved much sharper for the high energy range. The numerical results presented in table 2.4 confirm this tendency. In fact, the measured

2 Compton camera

pixel width of BGO1 at the PGI range is similar to that of LSO2 at the PET range, i.e. $\Sigma_{Y(\text{BGO1, PGI})} \sim \Sigma_{Y(\text{LSO2, PET})}$, as illustrated by fig. 2.23 (right).

Table 2.4: Comparison of the spatial resolution factors of the two scintillation materials at the ELBE experiment.

Detector	LSO2			BGO1		
	Σ	$P2V$	R	Σ	$P2V$	R
Factor (Y_{Block})						
PET range	0.05 ± 0.02	2.7 ± 1.1	1.5 ± 0.8	0.08 ± 0.04	1.8 ± 0.4	1.9 ± 0.5
Middle range	0.04 ± 0.02	2.8 ± 1.6	2.1 ± 1.0	0.06 ± 0.02	3.3 ± 1.1	2.5 ± 0.5
PGI range	0.03 ± 0.01	3.7 ± 1.7	2.4 ± 0.9	0.05 ± 0.02	4.4 ± 1.3	3.1 ± 0.8

Note: Σ is the width of the pixel peak (in relative crystal coordinates), $P2V$ the peak to-valley ratio and R the resolution. Calculations are made with respect to neighbour pixels of the same crystal column (Y_{Block} axis), cf. fig. 2.23. The result is averaged over all pixel columns and the error refers to the standard deviation. Note that Σ is calculated numerically after application of an iterative background subtraction algorithm (Ryan et al., 1988).

In other words, one could divide the BGO1 block in more pixels per block (as the 13×13 LSO2 matrix), utilise also the same light guide design as of LSO2, cf. fig. 2.12 (left), and still identify each pixel for the PGI range. This is clearly not the case for PET energies, where additional pixels would just overlap in the flood map and one would not be able to separate them any more. To confirm this statement and give some numbers, the flood map of a virtual 8×16 BGO block detector is modelled by cloning the spatial profile of fig. 2.23 (left), which corresponds to BGO1 at the PGI range, shifting it to the right about half the average distance between consecutive pixel peaks and summing it to the original one.

The resulting artificial profile is shown in fig. 2.24. The corresponding figures of merit are $\Sigma = (0.06 \pm 0.04)$, $P2V = (2.0 \pm 1.0)$ and $R = (1.7 \pm 1.2)$. Hence, the performance of a virtual 8×16 BGO block at the PGI range would be close to that of the actual 8×8 BGO1 detector at the PET range. It should be emphasised that this ad hoc procedure simulates more pixels per block detector but does not account for the higher probability of inter-crystal scattering in neighbour (closer) pixels or increased reflection losses, which may degrade further the flood map.

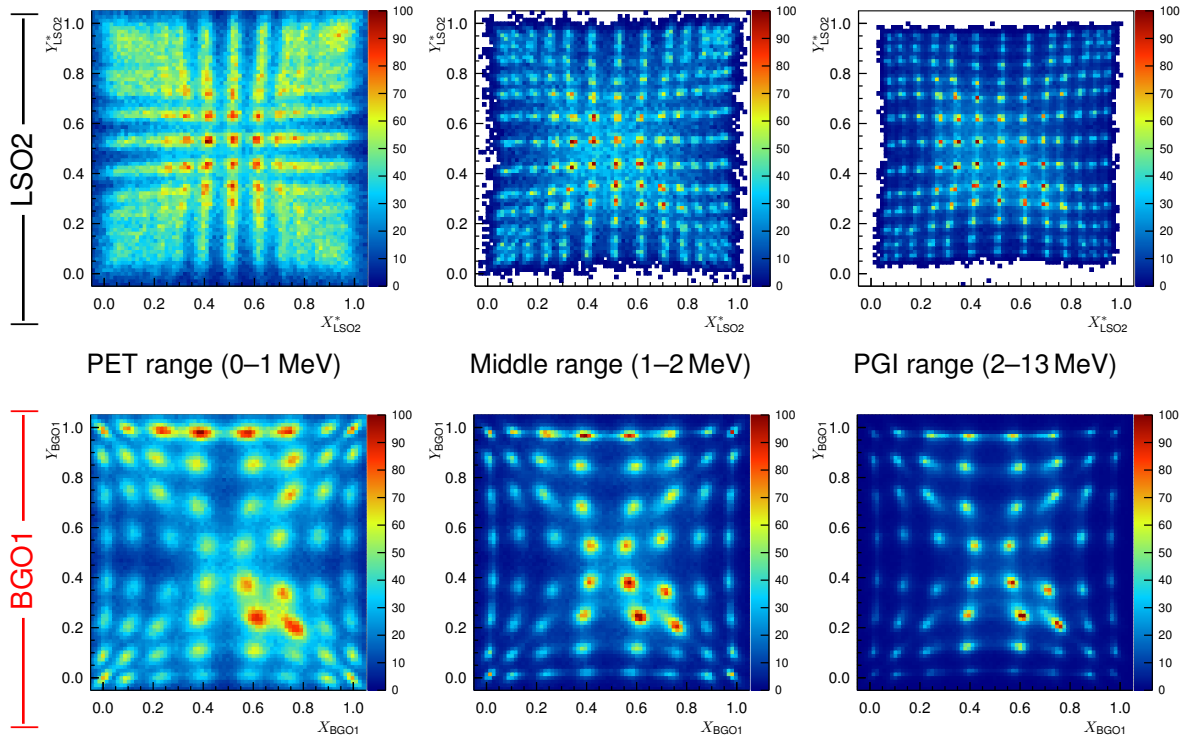


Figure 2.22: Block detector flood map (top: LSO2, bottom: BGO1) for different energy ranges at the ELBE accelerator (distortion correction applied for LSO2). Non-uniform intensities are due to the fact that the focused bremsstrahlung beam spot is smaller than the detector size, as well as the different extension (number of bins) of each pixel spot in the map.

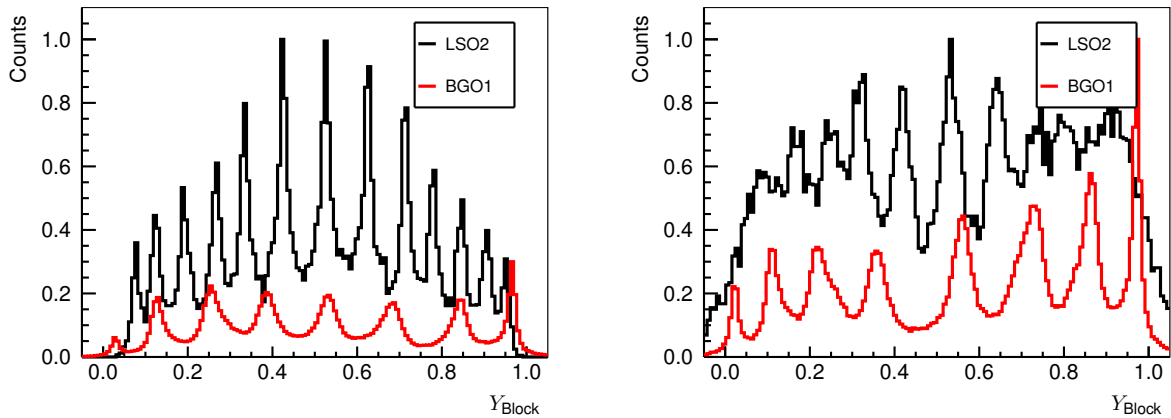


Figure 2.23: Left: 1D projection of the flood maps depicted in fig. 2.22 along the fourth crystal column (Y_{Block} axis) of the LSO2 (black line) and BGO1 (red line) block detectors for the PGI range. Right: 1D projection along the third crystal column and the PGI range for the BGO1 compared to the PET range for the LSO2. Both: vertical scale and BGO1 intensity relative to LSO2 are arbitrary.

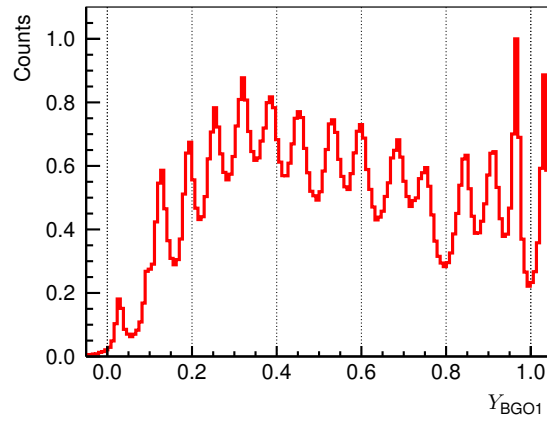


Figure 2.24: Artificial 1D projection of the flood map of a virtual 8×16 BGO block detector along the fourth crystal column (Y_{Block} axis). The original projection, which corresponds to BGO1 at the PGI range, cf. fig. 2.23 (left), is cloned and shifted to the right half the average distance between consecutive pixel peaks. Vertical scale is arbitrary.

2.7.3 Time resolution

Fig. 2.25 (left) shows the intrinsic time resolution of both blocks at the ELBE accelerator. LSO2 has an excellent time resolution thanks to its high light yield and short decay time. On the other hand, BGO1 has a four times lower light yield and much longer decay time, and cannot compete with LSO2 in relative terms, at least with analogue constant fraction trigger.

However, when considering the time resolution as a function of the energy, cf. fig. 2.25 (right), one can see that BGO1 increases its performance significantly, up to 2 ns for high energies, thanks to the larger amplitude of the signals and better determination of the time with the CFD (more photoelectrons, lower relative jitter). By using digital silicon PMTs, which can trigger (in principle) on the first photon, a time resolution below 300 ps can be achieved for high photon energies (Petzoldt et al., 2014).

From the experimental results, it is evident that the LSO2 detector has a significantly better time resolution than BGO1. This is an excluding factor for BGO1 in application fields as time of flight PET or prompt γ -ray timing (Golnik et al., 2014). For PGI at a clinical accelerator, a good time resolution is also advisable for suppression of radiation background (Biegun et al., 2012) in correlation with accelerator RF. However, the amount of background that can be discriminated depends not only on the detector time resolution, but on the accelerator bunch repetition rate and bunch time spread.

Is then the time resolution obtained with BGO block detectors good enough for PGI in a clinical radiation environment? To give a quantitative answer, the figure of merit FoM_{BSR} (Hueso González et al., 2014) is used, which measures the fraction of background that can

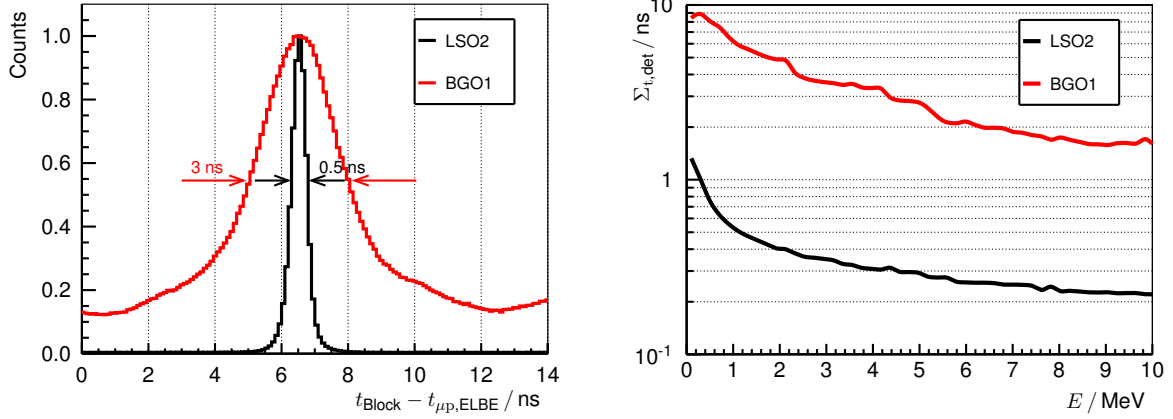


Figure 2.25: Left: time spectrum of the LSO2 detector (black line) compared to the BGO1 detector (red line) at the ELBE accelerator. The difference between detector signal arrival t_{Block} and closest accelerator micro pulse $t_{\mu\text{p,ELBE}}$ (13 MHz repetition rate, corresponding to 77 ns period) is represented. No energy filter is applied (bremsstrahlung spectrum goes up to 12.5 MeV). Vertical scale is arbitrary. The arrows mark the FWHM of the time distributions. Right: time resolution $\Sigma_{t,\text{det}}$ (FWHM) for the LSO2 (black line) and BGO1 (red line) block detectors measured at the ELBE accelerator as a function of the released energy E . The experimental points are approximately reproduced by the curves $\Sigma_{t,\text{det}} = (460 \pm 10) \text{ ps}/\sqrt{E/\text{MeV}} + (80 \pm 5) \text{ ps}$ for LSO2 and $\Sigma_{t,\text{det}} = (4900 \pm 500) \text{ ps}/\sqrt{E/\text{MeV}} + (10 \pm 10) \text{ ps}$ for BGO1.

be suppressed thanks to timing measurements in a pulsed accelerator:

$$FoM_{\text{BSR}} = 1 - \frac{\sqrt{\Sigma_{t,\text{det}}^2 + \Sigma_{t,\text{bunch}}^2}}{T_{\text{bunch}}} \quad (2.27)$$

where $\Sigma_{t,\text{det}}$ is the detector time resolution (FWHM), $\Sigma_{t,\text{bunch}}$ the bunch time spread (FWHM) and $T_{\text{bunch}} = f_{\text{bunch}}^{-1}$ the time separation between consecutive accelerator bunches (the inverse of the RF).

For the widespread C230 isochronous cyclotron, $T_{\text{bunch}} = 9.4 \text{ ns}$ and $\Sigma_{t,\text{bunch}} \approx 2 \text{ ns}$ for 100 MeV protons (Hueso González et al., 2015b). In this realistic scenario, the resulting figures of merit for 4 MeV prompt γ -rays are $FoM_{\text{BSR,LSO2}} = 84 \%$ and $FoM_{\text{BSR,BGO1}} = 64 \%$.

The BGO1 performance is worse than for LSO2 but acceptable for the defined goals, as long as its time resolution is in the order of magnitude of (or below) the intrinsic proton bunch width (plus γ -ray emission time) of the accelerator in question. The transit time of protons inside the target (and thus the prompt γ -ray emission time), which depends on the energy and target composition, is of the order of 1 ns (Golnik et al., 2014). This effect contributes also to the measured width of the prompt γ -rays in a time spectrum, and implies an additional limit to the background suppression capabilities. Consequently, the BGO1 and LSO2 figures of merit (effective performances) have the same order of magnitude, as the significant difference in time resolution is shadowed by the bunch time spread and transit

time. Rather than the detector time resolution itself, two other material features are of great significance: the decay time and the intrinsic radioactivity.

The decay time of BGO (7.5 times longer than LSO) is not appropriate for very high counting rate applications. As a rule of thumb, the count rate limit with manageable pile up is given by an average impulse separation of ten times the decay constant: 300 kcps for BGO and 2.5 Mcps for LSO. What is the expected rate in a clinical scenario for a BGO block detector? At an instantaneous beam current of ~ 2 nA (10^{10} protons per second) as in the C230 accelerator (Perali et al., 2014), assuming for simplicity a yield of 0.16 prompt γ -rays per proton as in (Golnik et al., 2014), a γ -ray attenuation of $\sim 40\%$ within the patient (Hubbell and Seltzer, 2004) and the BGO1 block at 30 cm distance with interaction efficiency $\epsilon_D \approx 50\%$ (Berger et al., 2010), one scores $\epsilon_{p\gamma} \simeq 10^{-4}$ γ -rays per proton. The resulting detector trigger rate (during effective beam delivery) is ~ 1 Mcps. This implies that BGO blocks with a smaller area (one third) should be deployed for this application, or (alternatively) that the distance from block to beam axis should be increased up to 55 cm, to keep the count rate around the ~ 300 kcps limit. It is worthwhile mentioning that such detector rates are also challenging for the electronics, data acquisition and real-time processing.

On the other hand, LSO has a larger afterglow and a high intrinsic radioactivity below 1 MeV due to ^{176}Lu , which may lead to a considerable amount of false coincidences in a Cc, as discussed in subsection 2.4.2.

2.8 Discussion – absorber choice

PGL is a reasonable approach for reconstructing the particle range in ion beam therapy. A Cc for these γ -ray energies is very challenging, as the underlying detector materials need to cope with demanding and diverse prerequisites at the same time. To support the design and development of a Cc, an experimental exploration of the detector behaviour in clinical-like radiation environments is needed concerning energy spectroscopy, spatial resolution and timing. Two scintillation materials, BGO and LSO, which are promising candidates for the absorber plane, are compared at three different accelerators.

LSO has an overall better performance, especially concerning timing resolution, but BGO closes the gap in the PGL range, as the high number of scintillation photons compensates for its lower light yield. The higher photofraction, absence of intrinsic radioactivity and much lower price make BGO a promising alternative material for the absorber, with an outcome comparable to LSO for the intended application. In other words, for the same price, a bigger camera could be built made of BGO without significant quality loss. Indeed, a 13×13 BGO block detector, as the LSO one, might be constructed to improve its spatial resolution.

In conclusion, the statement about the superiority of LSO in the PET scenario cannot be directly transcribed to PGL applications. The experimental detector characterisation reveals the suitability of BGO as absorber of a clinical Cc with a superior cost-effectiveness ratio.

2.9 Results – BbCc setup

In fig. 2.26, some representative detector energy spectra are shown for the scatterer (BGO4) and absorber (BGO1) of the BbCc. The energy resolution R_E at 511 keV is better for BGO1 ($\sim 19\%$) than for BGO4 ($\sim 22\%$). At the 1275 keV photopeak, one obtains 12% and 13%, respectively. This difference is more significant at 4.4 MeV, where the photopeak cannot be easily resolved from the SDEP for BGO4. The reason might be the smaller size of the BGO4 pixels (larger electron escape probability, worse light collection from thin long crystals) or a misleading pixel-wise energy calibration.

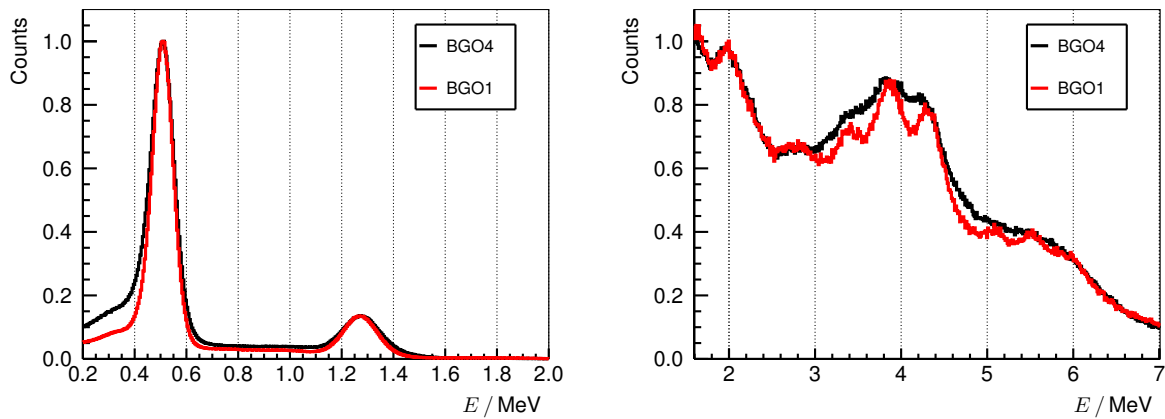


Figure 2.26: Detector response energy spectra of the scatterer (BGO4) and absorber (BGO1) of the BbCc at UPTD. Left: ^{22}Na point-like source. Right: prompt γ -rays emitted in a homogeneous PMMA phantom when irradiated by a 100 MeV proton pencil beam. No explicit time filter is applied, see text. Profiles are normalised to their respective maximum.

In fig. 2.27, one can see the correlation between the energy deposit at each block detector when the ^{22}Na source is located between the blocks (PET camera, left) and in front of them (Compton imaging, right). In the case of PET, one can observe the uncorrelated 511 keV lines (one vertical, one horizontal) and the actual coincidences (hot spot) from the back-to-back annihilation photons due to the emitted positrons. The scatter plot in the case of Compton imaging is completely different. Apart from the uncorrelated lines, one can see diagonal structures with -45° inclination, that correspond to real Compton events (scattered and absorbed photons) in the camera, stemming from the 511 and 1275 keV γ -rays. Mathematically, these straight lines are expressed by the implicit equation $E_{\text{BGO1}} + E_{\text{BGO4}} = E_\gamma$.

It is worth noting that no time filter is applied explicitly in the presented results, meaning that no cut is set on the coincidence time spectrum. The rationale is to recover events where one of both detector signals is under the discriminator threshold, so that its time stamp is missing, but a valid (small) energy is measured. The trigger is produced by the other block detector, and the same integration gate is used for both. The condition of positive energy implies an indirect time filter, as broad as the integration window. Thus, more events are recovered at the price of a higher number of random coincidences, which has more or less significance depending on the detector rate.

2 Compton camera

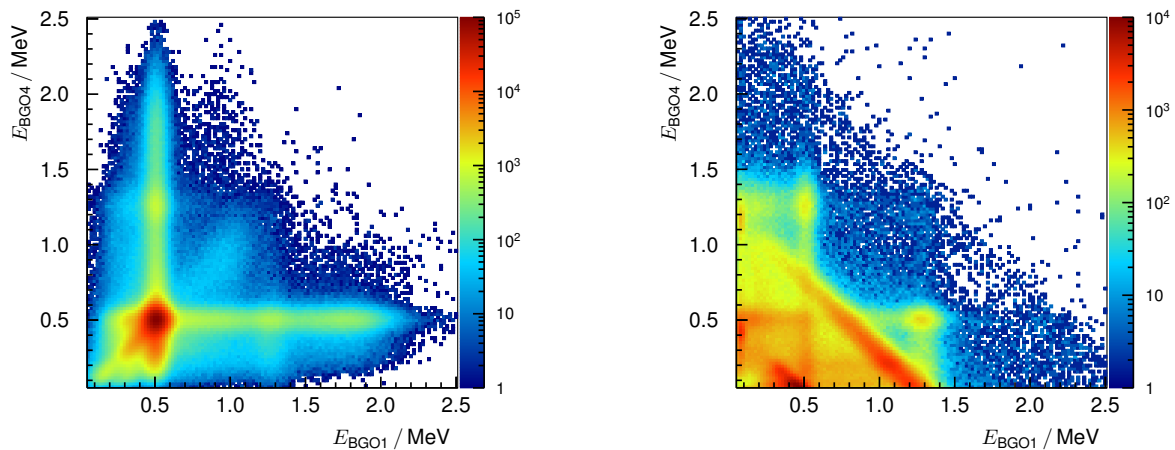


Figure 2.27: Energy scatter plots of the BbCc camera for a ^{22}Na point-like source. No explicit time filter is applied, see text. Left: the source is located between both block detectors (PET camera). Right: the source is in front of both blocks (Compton imaging).

Fig. 2.28 (top left) depicts the BP images of a ^{22}Na photon source placed in front of the BbCc. The definition of the x and y axis is from the perspective of an observer standing behind the camera (looking at the source), so that the images are upright. No iterative reconstruction algorithm has been applied. The FWHM is ~ 5 cm in each spatial dimension. In fig. 2.28 (top right and bottom row), the point-like source is moved periodically along the x axis to generate a line source.

In the reconstructed image profiles of fig. 2.29, the effect of spatial shifts along the x axis is observed. The left plot corresponds to a ^{60}Co source. The right one, to a $^{242}\text{Cm} + ^{13}\text{C}$ source. Curium emits α particles, that sometimes fuse with a carbon nucleus. The product is a neutron and $^{16}\text{O}^*$ in an excited state, similar to that produced in proton reactions (Kozlovsky et al., 2002), which deexcites via the emission of a 6.1 MeV prompt γ -ray.

At UPTD, a 70 MeV proton pencil beam irradiates a thick homogeneous target, and the resulting prompt γ -ray distribution is measured with the BbCc setup. The energy correlation spectrum is shown in figure fig. 2.30 (left), whereas the energy sum is depicted in figure fig. 2.30 (right), showing a broad peak at the 4.4 MeV energy region. The resolution of photopeak from SDEP is not expected due to the insufficient energy resolution of the individual detectors, cf. fig. 2.26 (right).

Fig. 2.31 shows the image of a 4.4 MeV prompt γ -ray distribution produced by a 70 MeV (left) and 160 MeV (right) proton pencil beam irradiating a homogeneous PMMA phantom at UPTD. Note that an energy filter is applied between 3.0 and 5.0 MeV, to enclose the peak seen in fig. 2.30 (right), i.e. the 4.4 MeV prompt γ -ray line and the SDEP (3.4 and 3.9 MeV). In addition, it is assumed that all filtered events stem from 4.4 MeV γ -rays. The energy deposit $L_a \equiv E_{\text{BGO}_1}$ in the absorber is then corrected event-wise for missing energy (due to the photon escape) so that the energy sum $E_\gamma = L_s + L_a$ yields 4.4 MeV ($L_s \equiv E_{\text{BGO}_4}$).

Fig. 2.32 evinces the effect of spatial shifts on BP profiles of a ^{22}Na source (left), and of

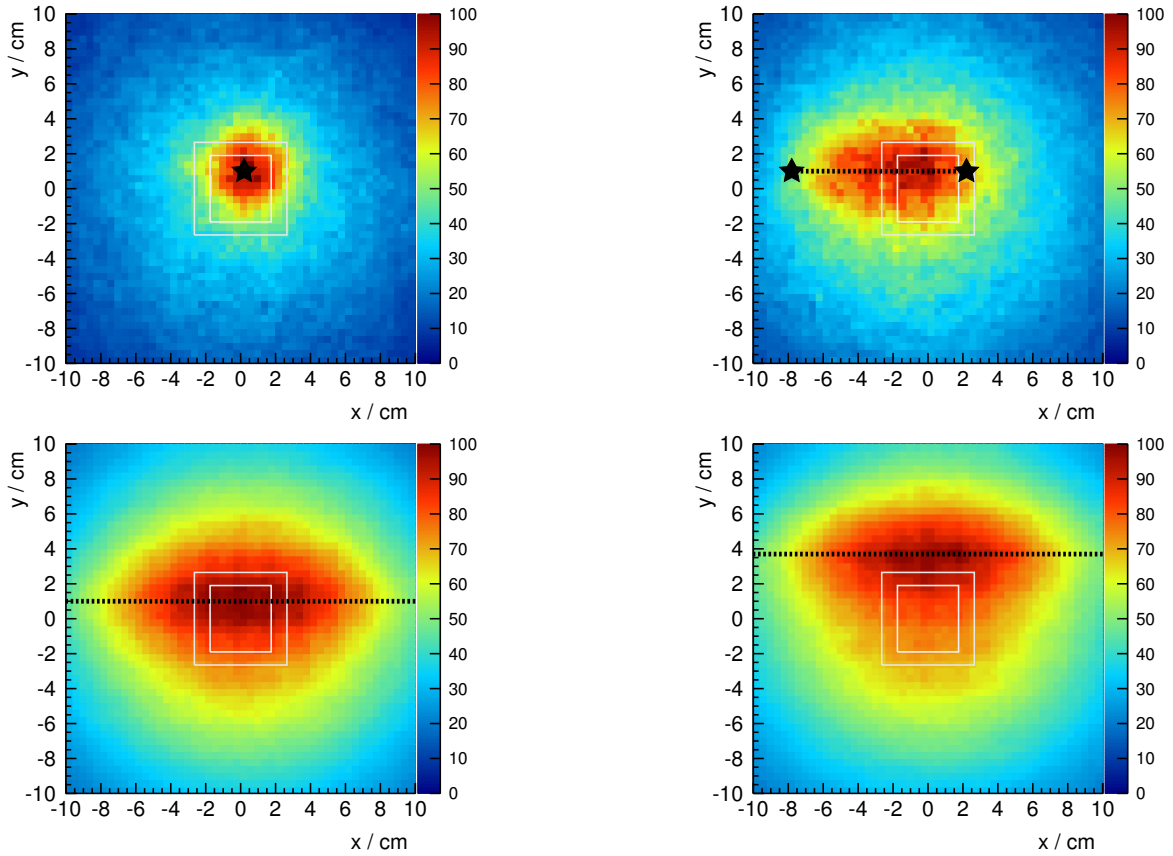


Figure 2.28: BP images of the BbCc at UPTD with a 1275 keV point-like source. Its separation to the scatterer center is (18.0 ± 0.9) cm. The scatterer to absorber distance is (6.5 ± 0.4) cm. The white rectangles represent the front faces of BGO4 and BGO1 in the center of the field of view. Top left: the black star is the expected source position. Top right: a 10 cm line source is produced by a periodic motion of the source across the dashed line (between the two black stars). Bottom row: 30 cm line source (see dashed line, black stars are out of the histogram range) at different heights (y axis) with respect to the camera.

4.4 MeV prompt γ -rays (right) produced by a 70 MeV proton pencil beam irradiating a thin PMMA target. The source/target spatial shift is correlated with a change of the mean value of the distribution. Fig. 2.33 analyses quantitatively the centroid of the distribution over the actually performed shift. There is a good agreement for the left graph; for the right case, one can see a trend but no quantitative match based on the analysis of the BP images.

Fig. 2.34 (left) compares BP profiles of 4.4 MeV prompt γ -rays produced in targets of various thicknesses by a 160 MeV proton beam. Fig. 2.34 (right) shows a complementary experiment with a fixed thickness target, but increasing the initial proton energy from 70 MeV up to 170 MeV. In both cases, a shift to the right in the mean value of the distribution can be identified correlated to the spatial range of γ -ray emission.

2 Compton camera

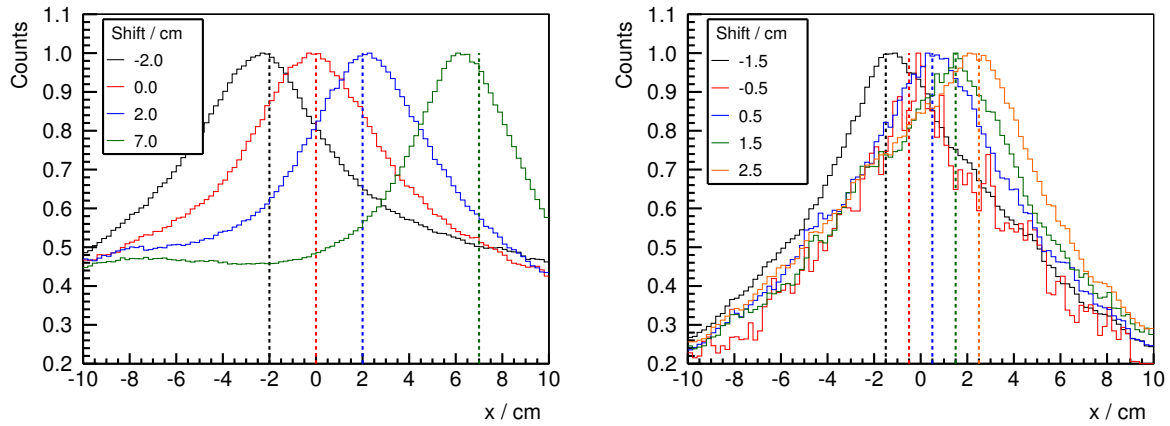


Figure 2.29: BP profiles of the BbCc for the spatial shift experiment at HZDR (across the x axis). Left: ^{60}Co point-like source (energy filter around the two photopeaks, which are not resolved in the energy sum spectrum). Right: 6.1 MeV γ -rays (energy filter includes the SDEP) produced by a ^{13}C source. Profiles are normalised to their respective maximum. Both: the dashed lines represent the performed source shift. The distance between source and center of the scatterer is (19.6 ± 0.9) cm. Between scatterer and absorber centers, it is (6.8 ± 0.4) cm.

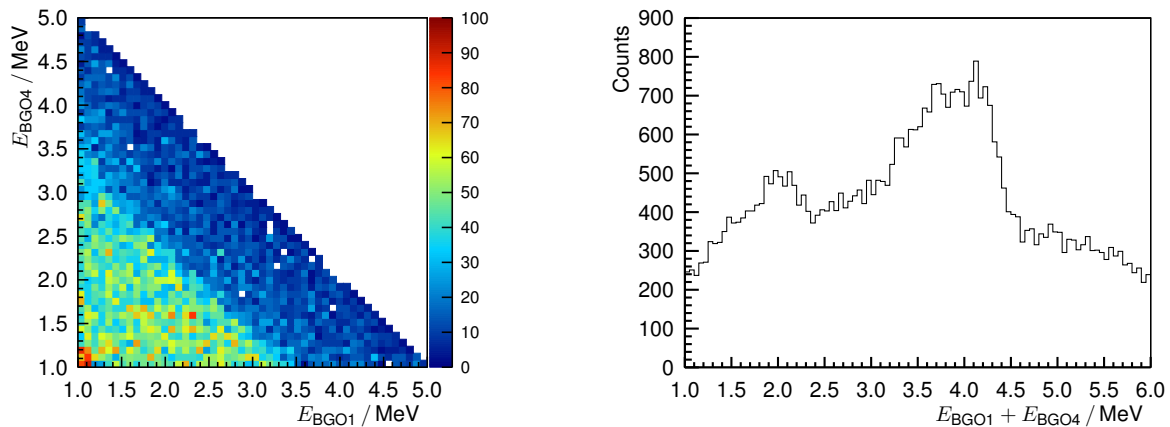


Figure 2.30: The BbCc measures at UPTD prompt γ -rays produced within a homogeneous PMMA phantom by a 70 MeV proton pencil beam. Coincident events are selected based on a broad time window of 40 ns and an energy sum filter between 1.0 and 6.0 MeV, see third filter of table 2.5. Left: energy correlation spectrum. Right: energy sum spectrum.

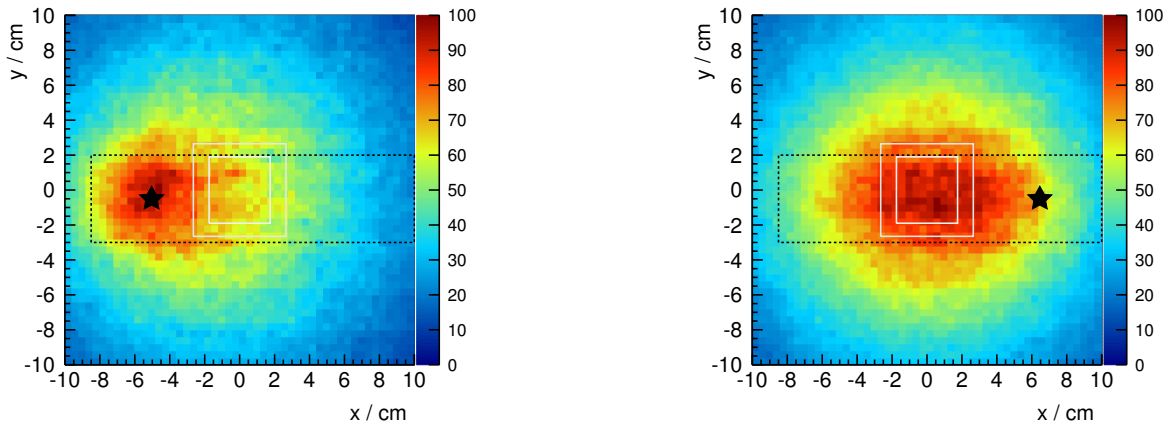


Figure 2.31: BP images of the BbCc at UPTD corresponding to 4.4 MeV prompt γ -rays, produced by a protons irradiating a homogeneous PMMA phantom. Beam incidence is from the left. The distance between beam axis and scatterer center is (20.0 ± 0.9) cm, the separation between crystal centers is (6.5 ± 0.4) cm. The white rectangles represent the front faces of BGO4 and BGO1 in the center of the field of view. The dashed black rectangle represents the target size ($\varnothing 5$ cm \times 40 cm) and the black star, the expected proton range in PMMA. It yields 3.5 cm for 70 MeV (left) and 15.1 cm for 160 MeV (right) protons. The fourth filter of table 2.5 is applied, and the effect of missing energy is corrected.

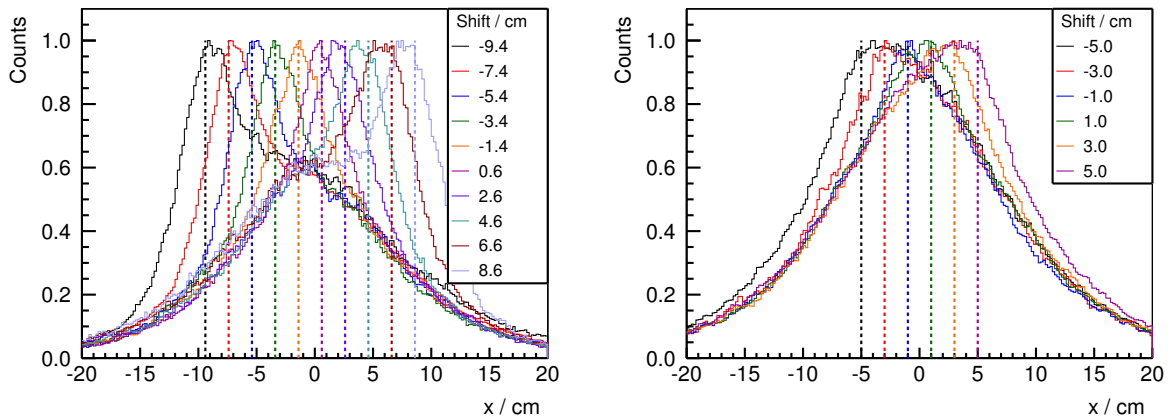


Figure 2.32: BP profiles of the BbCc for the spatial shift experiment at UPTD. Left: ^{22}Na point-like source (energy filter around the 1275 keV photopeak). The distance between motion axis and scatterer center is (18.0 ± 0.9) cm. Right: 4.4 MeV prompt γ -rays (fourth filter of table 2.5 is applied, missing energy is corrected) produced by 70 MeV protons crossing a thin PMMA phantom ($\varnothing 5$ cm \times 2 cm). Beam incidence is from the left. Profiles are normalised to their respective maximum. The dashed lines represent the performed shift of the source (left) or of the target (right). The distance between motion axis and scatterer center is (20.0 ± 0.9) cm. Both: the separation between crystal centers is (6.5 ± 0.4) cm.

2 Compton camera

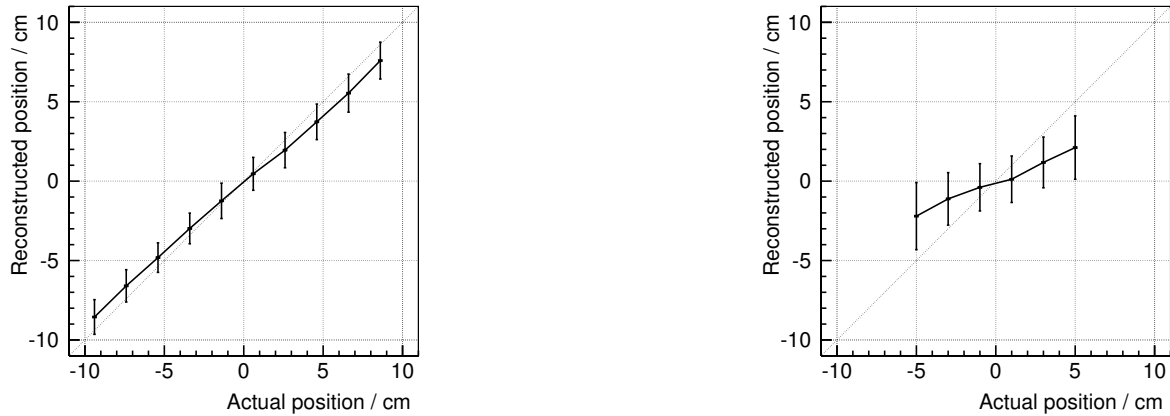


Figure 2.33: Left: centroid of the reconstructed profiles of fig. 2.32 (left) versus the actual position of the ^{22}Na point-like source (1275 keV photopeak). Right: analogous plot for 4.4 MeV prompt γ -rays produced inside the thin PMMA phantom, cf. fig. 2.32 (right). Both: the fit function for obtaining the centroid is a Pseudo-Voigt profile. The diagonal grid line depicts the ideal point distribution.

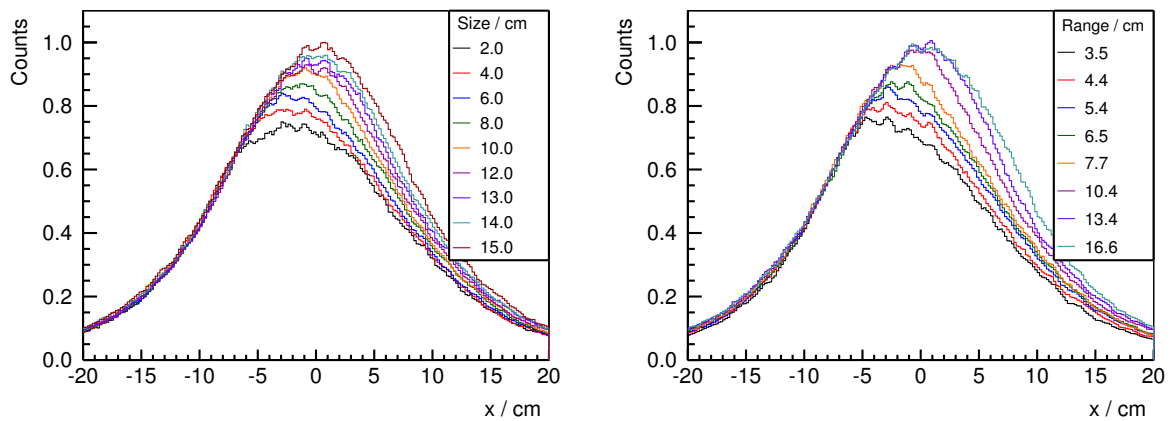


Figure 2.34: BP profiles of the BbCc for 4.4 MeV prompt γ -rays at UPTD. Normalisation is done arbitrarily to match approximately the distributions at $x \simeq -10$ cm. The fourth filter of table 2.5 is applied, and the effect of missing energy is corrected. Left: increasing the PMMA target thickness for 160 MeV protons (15.1 cm range). Proton range exceeds the thickness of the target for all measurements. Right: varying the proton beam energy (range) in 10 MeV steps from 70 to 170 MeV for a thick PMMA phantom ($\varnothing 5\text{ cm} \times 40\text{ cm}$). The measurements at 120, 140 and 160 MeV are excluded for the sake of clarity. Both: the beam axis is (20.0 ± 0.9) cm away from the scatterer center, the separation between scatterer and absorber centers is (6.5 ± 0.4) cm. Beam incidence is from the left.

2.10 Discussion – BbCc setup

A slight scepticism has settled down in the scientific community concerning Compton cameras for PGI. Due to technical complexity and high radiation background, only few experimental results hint at their applicability in a clinical environment. To close this gap, a high efficiency Cc setup is used to measure 4.4 MeV prompt γ -rays produced in a PMMA phantom when irradiated by a proton pencil beam. Low currents are chosen to adapt the count rate to the low throughput of the current acquisition system, and long measurement times are selected for collecting enough statistics to draw significant conclusions.

Target shifts, thickness increase or beam energy variation, corresponding to range differences down to 1 cm, correlate to changes of the BP images. This highlights the ability of the BbCc setup, comprising just eight electronic channels, to image high energy prompt γ -rays and detect associated range variations by simple inspection. This preliminary analysis has to be extended with a full reconstruction algorithm based on iterative methods and including the detector response matrix, as mentioned in subsection 2.1.4, but is out of the scope of this work. Setup optimisation, statistical sample reduction, use of heterogeneous targets and of clinical beam currents are also necessary future steps. It is worth remembering a weakness of the presented results: the normalisation of the profiles is done arbitrarily (matching by hand the leading edges), as no charge monitor is available during the experiments.

Nonetheless, some trends can already be identified based on the simple images obtained, which yield one of the first experimental results of Compton cameras at 4.4 MeV in a proton pencil beam of a clinical facility, together with (Polf et al., 2015). In both cases, the beam currents are far below the clinical values. The main difference is that (Polf et al., 2015) used semiconductor detectors with better energy resolution, but less efficiency than BGO (lower density), and a scatterer with 1.5 cm thickness instead of the 3.0 cm of BGO4. This trade-off, mentioned in subsection 2.2, has to be kept in mind: statistics (sensitivity) are a major concern in the field of PGI. The precision with which one can retrieve range differences are directly correlated to the statistics one can collect during the delivery of a pencil beam (as the γ -rays are prompt). And this collection efficiency depends on the manageable detector throughput (assuming fixed clinical beam currents) and the efficiency of the Cc. Thus, more events with less exact information may be more important than few very precise events.

How is this statement quantified? Considering the unoptimised BbCc setup, the number of valid Compton events (coincidences) compared to the single trigger rate at the scatterer is analysed. A particular measurement is chosen, namely an irradiation of a 40 cm thick PMMA phantom (\varnothing 5 cm) with ~ 160 MeV protons. The individual detector trigger rate is 90 kcps for BGO4 and 70 kcps for BGO1, arranged as depicted in fig. 2.16. The measurement lasts 7 min and the dynamic dead time of the VME data acquisition is $\sim 85\%$. The number of hits acquired and processed is 6.8×10^6 for BGO4 and 3.4×10^6 for BGO1. The number of valid Compton events depends on the condition set for the coincidence, cf. table 2.5 for different filters.

Table 2.5: Valid Compton events for a particular experiment at a 160 MeV proton pencil beam with the BbCc setup and a homogeneous 40 cm thick PMMA phantom.

	Applied filters	Valid events	k_ϵ
	$E_{\text{BGO}i} \in [0.05, 6] \text{ MeV}; E_{\text{sum}} \in [1, 6] \text{ MeV}$	280×10^3	4.1 %
	$E_{\text{BGO}i} \in [0.05, 5] \text{ MeV}; E_{\text{sum}} \in [3, 5] \text{ MeV}$	130×10^3	1.9 %
$ t_{\text{BGO}1} - t_{\text{BGO}4} < 20 \text{ ns}; E_{\text{BGO}i} \in [0.05, 6] \text{ MeV}; E_{\text{sum}} \in [1, 6] \text{ MeV}$		85×10^3	1.3 %
$ t_{\text{BGO}1} - t_{\text{BGO}4} < 20 \text{ ns}; E_{\text{BGO}i} \in [0.05, 5] \text{ MeV}; E_{\text{sum}} \in [3, 5] \text{ MeV}$		28×10^3	0.4 %

Note: Depending on the applied coincidence filters, a different number of events usable by the image reconstruction algorithm is obtained. $E_{\text{BGO}i}$ refers to the energy at each block detector ($i = 1, 4$). $E_{\text{sum}} \equiv E_{\text{BGO}4} + E_{\text{BGO}1}$. k_ϵ is the ratio between valid events and the number of hits acquired by the BGO4 detector (6.8×10^6).

One can see that applying the (explicit) time filter reduces about a factor of four the number of valid events. This is due to the CFD threshold (leading to a valid time stamp), which is relatively high as a consequence of the signal to noise ratio of the electronics. As mentioned before, one may think of not applying a time filter in order to maximise the statistics in spite of a higher amount of random coincidences and non-prompt background.

Are the measured detector rates in agreement with theoretical estimations? The beam current during the experiment is about 40 pA (2.5×10^8 protons per second). The total number of protons delivered during the whole measurement time is 1.1×10^{11} . Assuming a yield of 0.16 as in (Golnik et al., 2014), the total number of produced γ -rays is 1.7×10^{10} . Taking into account the covered solid angle, cf. eq. 3.10, and detection efficiency (Berger et al., 2010), the expected rate at the BGO4 detector is ~ 50 kcps. The discrepancy with respect to the measured rate (90 kcps) is most probably because the assumed γ -ray yield is for energies above 1 MeV, whereas the detector threshold is at the scale of 100 keV. Also, contributions from target activation are significant (up to 20 kcps background rate in some cases).

What would be the situation in a clinical irradiation scenario? The instantaneous beam current in PBS at the C230 accelerator (Perali et al., 2014) is around ~ 2 nA, i.e. 1.2×10^{10} protons per second (measured at nozzle exit). In any treatment plan, there are beam spots with different number of protons (Smeets et al., 2012, fig. 19). This is not regulated by changing the beam current, but by the beam spot duration, which may be up to 8 ms for the strongest spot. If the BGO4 detector is placed at 25 cm distance from the beam axis, the covered solid angle $d\Omega/\Omega$, cf. eq. 3.10, is 1.4×10^{-3} . Assuming 45 % attenuation in the phantom and 56 % detection efficiency (Berger et al., 2010), the number of registered γ -rays per proton $\epsilon_{p\gamma} = 6.6 \times 10^{-5}$ and the estimated detector trigger rate is 8.2×10^5 cps (above 1 MeV, but far more than 1 Mcps if lower energies are included). Taking an average factor $k_\epsilon = 2\%$, and dismissing the fact that BGO cannot sustain such detector load, this would lead to 16 kcps coincident rate. Hence, for the longest spot, around 130 valid coincidences would be collected. This implies that a dosimetry based on each pencil beam spot is not feasible even with this high efficiency camera setup; one should increase the number of detectors considerably to obtain statistically significant conclusions.

Of course, one cannot scale directly the experiments at 40 pA to 2 nA, as more random coincidences would fall in the time window, the large γ -ray flux would affect the resolution, the electronics should cope with that rates, not to mention that the slow decay time of BGO would lead to an unmanageable pile-up if the detector load is above 3×10^5 cps. Reducing the block detector front face size and keeping the same number of pixels per block increases the camera granularity and reduces the detector load and dead time. Otherwise, one has to increase the distance to the beam axis to reduce the rate at each block detector. Note also that these are rough estimates, that depend strongly on prompt γ -ray yield, CFD threshold, detector size, applied energy and time filters, among others. One should look at the order of magnitude rather than at the exact numbers. MC simulations of this setup may provide more reliable estimates, as in (Rohling, 2015).

One could also argue that there is no need for a dense or thick scatterer, i.e. with a high macroscopic incoherent scattering cross section, as there is anyway a huge number of impinging γ -rays. But then, the absorber should fully stop the γ -rays that do interact in the scatterer in order to balance the poor scattering efficiency. As it is a process of statistical nature, one is forced to use a thick or dense detector as absorber, not a thin one (in the two-plane camera). Consequently, the detector load in the absorber is comparatively huge, as the γ -rays are absorbed independently from the interaction or not in the scatterer. The asymmetry in the detection rate in absorber and scatterer plane is very large, which leads to few valid coincidences, and many unwanted single events and random coincidences. In the BbCc setup, this asymmetry is broken or minimised by using BGO also as scatterer. Whether or not the thickness of BGO4 as scatterer material is too large and leads to a reduction of valid Compton events due to multiple scattering before reaching the absorber should be subject of study based on MC simulations (Herbach et al., 2009), for maximising the effective efficiency of the BbCc setup.

BGO is used as scatterer instead of LSO, despite the better energy resolution of the latter and similar scattering efficiency, in order to avoid the problem of trojan coincidences discussed in subsection 2.4.2. This choice is endorsed by the comparable performance of BGO and LSO at the PGI range (high γ -ray energies), demonstrated in section 2.7. The intrinsic background of LSO is a too high price to pay for a small increase in energy resolution, that is wasted anyway in the case of events with incomplete energy deposition.

In conclusion, the presented experimental data indicate that the imaging of 4.4 MeV prompt γ -rays is feasible with a Cc, as shown also by (Polf et al., 2015), and using BGO as scatterer. However, technical constraints like detector throughput, random coincidences and scarce statistics per spot make this approach almost hopeless in a clinical scenario, if one wants to obtain a real-time range estimation with millimetre precision without reducing the usual beam current. Indeed, one has to ponder if the electronics complexity and corresponding expense in order to obtain 2D or even 3D images is worth the effort compared to other simpler systems like the slit camera, which provides reliable 1D profiles and trustworthy estimators of the particle range in realistic clinical conditions (Priegnitz et al., 2015).

3 Prompt gamma-ray timing

3.1 Theoretical background

3.1.1 Detection principle

At OncoRay and HZDR, an innovative method for range assessment complementary to actively and passively collimated PGI systems has been recently proposed (Golnik et al., 2014): the Prompt Gamma-ray Timing (PGT). The transit time of therapeutic ions in matter is around one nanosecond, a time scale that can be assessed with commercial detectors and electronics. Prompt γ -rays, a by-product of the passage of the particles, are emitted instantaneously (most of them on the scale of picoseconds). As a consequence, the birth time of γ -rays reflects the ion penetration depth (transit time until interaction point).

Fig. 3.1 illustrates this physical effect: the deeper the ion interaction (prompt γ -ray emission) point, the larger the ion transit time and the time of flight of the γ -rays to the detector. Changes in the reception time distribution are correlated with particle range differences. This distribution is a handle to obtain essential information about the depth-dose profile. Hence, a single detector in a timing spectroscopy setup can verify the range at minimum expense and without collimation, just measuring the time between particle entrance in the target and reception of the prompt γ -ray. As usual, the accelerator RF can be used as time reference (bunch arrival).

3.1.2 Kinematics

The derivation of the 1D ion transit time equation based on kinematics and the CSDA is detailed in (Golnik et al., 2014), and reviewed here. A heavy charged particle (p) with initial kinetic energy $E = E_0$, position $z = z_0$ and emission time $t = 0$ propagates across the z axis through a target with mass density $\rho(z)$. The ion energy variation per unit length is related to the stopping power:

$$\frac{dE}{dz} = -\rho(z) S(E) \quad (3.1)$$

where the stopping power $S(E)$ is specific to the particle and target material. The kinetic energy E of the ion at any depth $z > z_0$ is:

$$E(z) = E_0 - \int_{z_0}^z \rho(z') S(E(z')) dz' \quad (3.2)$$

3 Prompt gamma-ray timing

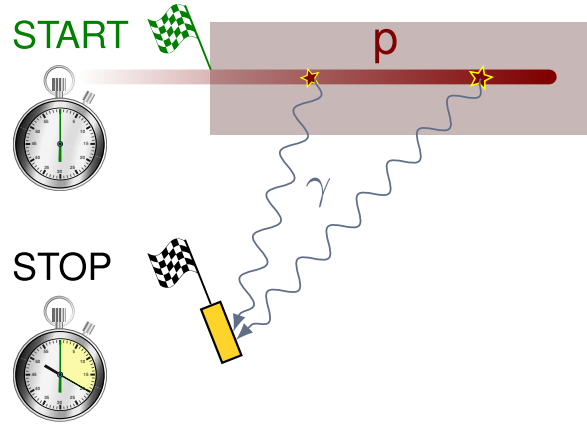


Figure 3.1: Illustrative sketch of the PGT method for range assessment in ion beam therapy. The therapeutic projectile (p) slows down as it penetrates the target and interacts with a nucleus, which emits a prompt γ -ray. The time between the entrance of the ion to the target (the start flag) and the arrival of the γ -ray to the detector (the stop flag at the yellow rectangle) reflects the ion transit time plus the γ -ray time of flight. This time span is correlated to the depth of interaction of the ion (γ -ray emission point).

The relativistic velocity v of the particle is (in natural units, i.e. $c \equiv 1$):

$$v(E) = \sqrt{1 - (1 + E/m_0)^{-2}} \quad (3.3)$$

where m_0 is the particle mass. The equation of the particle transit time yields:

$$t_p(z) = \int_{z_0}^z \frac{1}{v(E)} dz' = \int_{E(z)}^{E_0} \frac{1}{v(E) \rho(z'(E)) S(E)} dE \quad (3.4)$$

where dz' has been exchanged with dE using eq. 3.1. This substitution is only valid in regions where $\rho(z') > 0$. Indeed, the factor $z'(E)$, i.e. the inverse of eq. 3.2, is only well defined within these intervals. In regions with vacuum $z \in (a, b]$, namely the white slice in fig. 3.2, a piecewise function accounting for the propagation at a constant velocity $v(a)$ has to be introduced instead:

$$t_p(z) = t_p(a) + \frac{z - a}{v(a)} ; z \in (a, b] \quad (3.5)$$

If the target is thick enough, the ion is stopped completely at the particle range $R_p(E_0) \equiv z(E = 0)$ and eqs. 3.4 and 3.5 are only defined for $z_0 < z < R_p(E_0)$. If the particle exits the rear face of the target at $z = z_{\max}$ without being stopped, then eq. 3.5 applies for all $z > z_{\max}$.

Given the number of prompt γ -ray emissions dG per particle, the spatial density profile (per particle and unit length) is $g_z(z) \equiv dG/dz$, and the corresponding density $g_t(t_p) \equiv dG/dt_p$ per unit transit time is:

$$g_t(t_p) = \frac{dG}{dz} \frac{dz}{dt_p} = g_z(z(t_p)) \cdot v(E(z(t_p))). \quad (3.6)$$

where $z(t_p)$ is the inverse of eq. 3.4, that is correctly defined until the particle stops. Eq. 3.6 can be expressed also in terms of a binned transit time histogram h_t :

$$h_t(i) = \int_{z(t_{p,i}^-)}^{z(t_{p,i}^+)} g_z(z) dz. \quad (3.7)$$

where i refers to the bin number, and $t_{p,i}^-$ and $t_{p,i}^+$ to the respective lower and upper edge values of this bin.

3.1.3 Detector model

The previous subsection considers just the ion transit time t_p . Assuming (for simplicity) instantaneous nuclear de-excitation, t_p is equivalent to the emission or birth time of γ -rays. The next step is to introduce an ideal γ -ray detector in the xz plane, cf. fig. 3.2, at a distance d from the reference point $z = z_r$ and an angle α with respect to the $z > z_r$ axis. The beam energy is E_0 , the bunch time spread is $\sigma_{t,\text{bunch}}$ and the incidence is from the left. In the results section, the bunch spread or detector time resolution is reported as the FWHM Σ (capital letter) of the Gaussian-shaped distribution, which is proportional to the aforementioned σ through the relation $\Sigma = 2\sqrt{2\ln 2} \sigma$.

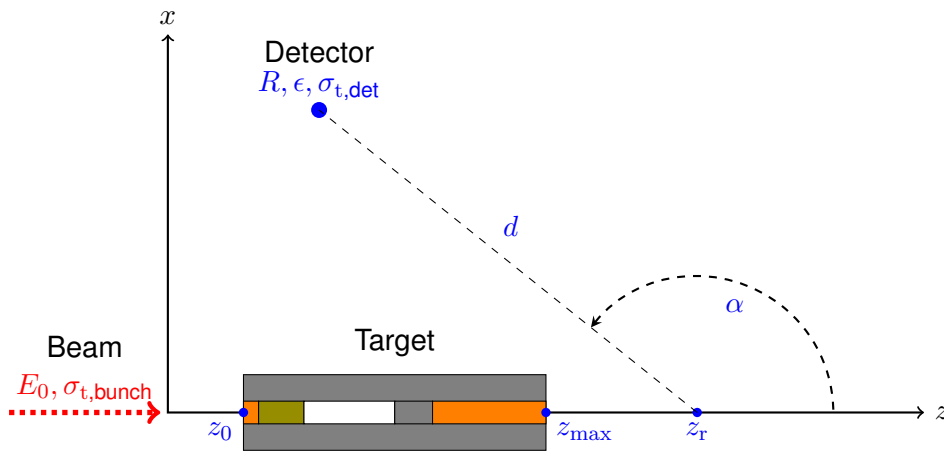


Figure 3.2: Schematics of detector and target position in a Cartesian coordinate system. The ion beam incidence direction is from the left and along the z axis. The initial ion kinetic energy is E_0 and the bunch time width is $\sigma_{t,\text{bunch}}$. The cylindrical target comprises an inner shell made of different materials (colors) and an outer homogeneous shell (in gray). The front face is at z_0 , the rear face at z_{max} . The detector is an ideal sphere of radius R , efficiency ϵ and time resolution $\sigma_{t,\text{det}}$. It is located at a distance d from the rotation center z_r and an angle α with respect to the $z > z_r$ axis.

The (illustrative) clock of fig. 3.1 measures the time difference Δt between the arrival of the γ -ray to the detector and the entrance of the ion in the target. In practice, the reference time is given by the RF, whose phase can be correlated to the passage of the ion through a virtual plane. This implies just a fixed time offset $t_0 \neq 0$ in the clock start (the time the ion

3 Prompt gamma-ray timing

needs to cover the distance between virtual plane and target entrance), depending solely on the accelerator settings and target location. The γ -rays are generated in the region $z_0 \leq z \leq \min(z_{\max}, R_p(E_0))$ with $\rho(z) > 0$. The *reception time* $t_r(z)$ measured by the clock (stop flag) is expressed as:

$$t_r(z) = t_0(E_0; z_0) + t_p(z) + t_\gamma(z). \quad (3.8)$$

where $t_p(z_0) = 0$ and $t_\gamma(z) = l_\gamma(z)$ is the γ -ray time of flight from emission point z to the detector. The γ -ray propagates at speed of light $c \equiv 1$ independently of the index of refraction of the traversed medium. Applying the law of cosines, the distance $l_\gamma(z)$ yields:

$$l_\gamma(z) = \sqrt{d^2 + (z - z_r)^2 - 2d(z - z_r) \cos \alpha} \quad (3.9)$$

However, not all emitted γ -rays (in 4π) are measured by the detector. The covered solid angle $d\Omega/\Omega$, assuming for simplicity a spherical detector entrance window on the symmetry axis for all z (Shelyuto, 1989), is:

$$\left(\frac{d\Omega}{\Omega}\right)(z) = \frac{1}{2} \left(1 - \sqrt{\frac{1}{1 + (R/l_\gamma(z))^2}}\right) \quad (3.10)$$

The attenuation of γ -rays I/I_0 inside the target (between emission point and detector) is also a significant weighting factor, that depends on the γ -ray energy as well as the target geometry and composition. Ray tracing is required for complex geometries in order to calculate the effective traversed path as a function of the emission depth z . A first-order approximation may include only the path $L_\gamma(z)$ traversed inside the gray material surrounding the slices on the beam path (fig. 3.2).

$$\left(\frac{I}{I_0}\right)(z; E_\gamma) = \exp \left[- \left. \frac{\mu}{\rho} \right|_{E_\gamma} \rho L_\gamma(z) \right] \quad (3.11)$$

where μ/ρ is the energy-dependent X-ray mass attenuation coefficient (Hubbell and Seltzer, 2004). Any γ -ray may interact inside the detector and give a valid timing signal, but it cannot be ensured that high energy photons are completely absorbed. In the case where the original γ -ray energy is not well known, or in the situation where the detector energy resolution is poor, one may evaluate the attenuation factor at the average energy \bar{E}_γ of the expected energy spectrum. This approximation is legitimate, since the attenuation coefficient curve is almost flat in the region of typical prompt γ -ray energies, cf. fig. 2.10.

Based on this simple beam, kinematics, detector and sensitivity model, the expected reception time histogram r_t is:

$$r_t(i) = \epsilon(\bar{E}_\gamma) \int_{z(t_{r,i}^-)}^{z(t_{r,i}^+)} g_z(z) \cdot \left(\frac{d\Omega}{\Omega}\right)(z) \cdot \left(\frac{I}{I_0}\right)(z; \bar{E}_\gamma) \cdot dz. \quad (3.12)$$

where $z(t_r)$ is the inverse of eq. 3.8. Note that t_0 has to be calibrated beforehand for each

beam energy E_0 and target location z_0 . It is also affected by changes of cable length in the electronics.

What would be the timing histogram measured with a realistic particle beam with bunch time spread $\sigma_{t,\text{bunch}}(E_0)$ and a detector of time resolution $\sigma_{t,\text{det}}$? Assuming a Gaussian convolution kernel $g(t; \sigma_T)$ with global system time response $\sigma_T = (\sigma_{t,\text{bunch}}^2 + \sigma_{t,\text{det}}^2)^{1/2}$, the measured PGT histogram m_t is:

$$m_t(i) = r(t) * g(t; \sigma_T) = \sum_{j=1}^N r_t(j) \frac{1}{\sqrt{2\pi}\sigma_T} \int_{t_{r,i}^-}^{t_{r,i}^+} \exp\left[-\frac{(t' - t_j)^2}{2\sigma_T^2}\right] dt' \quad (3.13)$$

where i or j refer to the bin number and t_i or t_j , to the bin center of the respective histograms. The integral of the Gaussian function can be evaluated in terms of the error function (erf) or approximated by:

$$m_t(i) \approx \frac{\Delta t_i}{\sqrt{2\pi}\sigma_T} \sum_{j=1}^N r_t(j) \exp\left[-\frac{(t_i - t_j)^2}{2\sigma_T^2}\right] \quad (3.14)$$

denoting Δt_i the bin width $t_{r,i}^+ - t_{r,i}^-$. Whether or not the emission density profile $g_z(z)$ will be retained after this transformation depends strongly on the convolution width σ_T (Golnik et al., 2014). As state-of-the-art γ -ray detectors achieve very good timing resolutions, the blurring may be dominated by the accelerator-dependent $\sigma_{t,\text{bunch}}(E_0)$.

This is the current model under the PGT method. The known limitations are:

- The pencil beam is assumed to be infinitely sharp (1D, neither spot size nor lateral spread).
- Neither initial energy spread $\sigma_{E_0,\text{bunch}}$ of the beam bunch nor range straggling (time straggling) are included.
- No energy dependence in the γ -ray emission profile $g_z(E_\gamma)$ has been yet introduced.
- For the derivation of the solid angle formula, cf. eq. 3.10, the ideal detector is assumed to have a spherical entrance window.
- Slices on the beam path are assumed to be 1D, see $\rho(z)$, whereas the γ -ray attenuation is considered only in the enclosing material (in gray).
- The uncertainties (Andreo, 2009) concerning the tissue-dependent stopping power $S(E)$ affect eq. 3.4.
- The error bars regarding the absolute prompt γ -ray yield ($g_z(z)$). The average number of γ -rays emitted per proton depends on tissue composition and incident energy (Janssen et al., 2014; Pinto et al., 2015).
- The anisotropy of the γ -ray emission is not taken into account (Shute and Baxter, 1966, p. 8).

3 Prompt gamma-ray timing

- The bunch time spread $\sigma_{t,\text{bunch}}(E_0)$ is assumed to be known and stable. For energies with large bunch time spread, the PGT method is still applicable based on distribution momenta (Golnik et al., 2014).
- The system time response is approximated by a Gaussian kernel of width σ_T .
- The half life of excited nuclei is significant for certain (quasi) prompt γ -ray lines (Kozlovsky et al., 2002) and should not be neglected in those specific cases, e.g. 1.0 ns for $^{10}\text{B}^*$ (0.718 MeV) or 27 ps for $^{16}\text{O}^*$ (6.130 MeV).

3.1.4 Quantitative assessment

In a practical situation, medical physicists need tools or indicators for verifying the particle range during beam delivery. If severe range deviations are detected, the therapy could be interrupted and the source of error analysed. Is the PGT method able to provide a quantitative estimate of the particle range or of the range deviation? Even though the PGT spectra encode information about the prompt γ -ray spatial emission distribution, neither the conversion of time to spatial profile nor the direct quantitative retrieval of the range are trivial procedures. Here, various strategies towards range reconstruction are proposed.

Forward calculation

One option is to compare the experimental PGT spectrum with a modelled one, once a spatial emission profile $g_z(z)$ is known or assumed. The spatial profile can be modelled analytically, or calculated by means of a MC simulation (Verburg et al., 2012), which depends on tissue composition and reaction processes involved (γ -ray lines). Discrepancies between different codes and experimental validation need still to be addressed (Schumann et al., 2015). The modelled or simulated spatial emission density is then transformed into a timing spectrum after application of eq. 3.13, and is compared to the measurement.

A more sophisticated approach is to compute directly the measured spectrum m_t with a full MC simulation including the detector response (detection probability and pulse height distribution for a given γ -ray energy) and the selected energy window of the PGT spectrum. However, the comparison of measured PGT distributions with MC simulations is out of the scope of this dissertation.

If the differences in the shape or momenta of the distribution (between reference m_t and experiment) are statistically significant, one can draw the conclusion that the treatment is not being delivered as planned. Changes in the centroid or width of the distributions can provide a quantitative estimate of the range shift, as proven by (Golnik et al., 2014).

Backward calculation

From the reception time spectrum r_t , one can try to reconstruct $g_z(z)$. Once the time origin t_0 is adjusted, eq. 3.12 can be inverted. Reception time is correlated to spatial depth unambiguously if the stopping power is known a priori, and the inverse histogram transformation can be applied.

However, the measured spectrum m_t is the time convolution of r_t and is thus not invertible. Deconvolution algorithms designed for locating photopeaks in convolved energy spectra are not applicable in this scenario, independently on how precise the convolution kernel (Gaussian-like or not) is known, or on how much spectrum statistics are collected. As a consequence, if one approximates $r_t \approx m_t$, the reconstructed spatial profile $g_z(z)$ will be blurred by the time convolution kernel. For large σ_T , this approach is not advisable.

In the case of small σ_T , the backward calculation is particularly interesting, as one may reconstruct in real-time a prompt γ -ray emission profile and assess quantitatively range differences by identifying shifts in the distal fall-off. In fact, one may be able not only to recover the particle range, but to have an estimate of the emission along the ion track (provided that the *true* stopping power is known, so that no large bias is introduced).

Parametric reconstruction

The MLEM method seems appropriate for the reconstruction of the prompt γ -ray emission distribution based on the measured PGT spectra. One could also combine data from several detectors in a single system matrix. Compared to MLEM in Compton imaging, the number of dimensions and measurement uncertainties are smaller, so that the inverse problem is better conditioned. However, the algorithm needs a very good characterisation of the system response, as the time convolution kernel σ_T and deviations from the Gaussian shape may play a significant role on the final reconstructed profile.

In this study, to keep it as simple as possible, an alternative strategy is applied: the *parametric reconstruction*. In controlled experiments, where the target geometry and beam settings are well known, the γ -ray emission distribution can be parametrised as $g_z(z; \lambda)$. What does the parameter λ represent? Imagine a particle beam impinging a homogeneous target. The beam energy E_0 is unknown, but it is sure that the ion range $R_p(E_0)$ is smaller than the target thickness. It is assumed that g_z is constant from target entrance to ion stopping point, and zero otherwise. This is known as the simple Box (simBox) model (Golnik et al., 2014). This curve shape can be easily parametrised with λ equal to the width of the box, i.e. the particle range. Note that λ does not change the height of the box, but just the width.

For several values of λ within a region of interest, the expected PGT profile is computed (forward calculation) and compared to the experimental one, e.g. with the weighted χ^2 test. The value of λ with the lower deviation in the associated test is the likeliest ion range. In

3 Prompt gamma-ray timing

other words, the minimum of the parametric function $\chi^2(\lambda)$ is found and the most probable range is estimated as $R_p(E_0) = \lambda_{\min}$.

This quantitative method is well defined and provides a fast range assessment tool. It circumvents the ill-posed deconvolution problem mentioned in the backward calculation by applying only forward calculation and minimising a cost function with respect to a single parameter. It is worth noting that this method compares implicitly the mean value and width of the distribution (as in the forward calculation), but incorporates additional information about the integral of the distribution (related to the region of γ -ray emission and its distance to the detector).

However, this simple approach seems only applicable in cases with enough a priori information, so that a single parameter can describe the emission profile. In addition, the time offset t_0 and prompt γ -ray yield (height of the square box) have to be calibrated empirically (once) for a benchmark case. In more realistic cases, one could describe the emission profile with two or three parameters and minimise with respect to these multiple dimensions.

Limitations

In any of the techniques described, one has to take into account that calculations are biased by the a priori assumption of the stopping power (eq. 3.4). In the case where there is an untracked anatomy change (like cavity filling), the effect on the reconstructed profile may be shadowed or remain unnoticed. In contrast, the Cc method or the slit camera are independent on the stopping power, at least for obtaining a prompt γ -ray profile.

Other factors that may have a significant impact on the quantitative range assessment, as mentioned before, are the radiation background, the prompt γ -ray yields, the non-Gaussian shape of the beam bunch, the attenuation inside the target and the detector efficiency (both dependent on the event-wise γ -ray energy, which is unlikely to be completely absorbed in the detector), or the γ -ray lines stemming from excited nuclei with long lifetimes. One should not forget any of these, as characterising or optimising too much a single of these contributions is useless if the error introduced by another factor is much higher. Further work is needed in many directions to provide accurate and robust range estimation.

3.2 Goals

The proof of principle experiment carried out at a research accelerator (Golnik et al., 2014) raises expectations about the future of the PGT method. To evaluate its potentials as well as its limitations, a dedicated experiment at a clinical therapy facility with heterogeneous targets and a pencil beam is mandatory.

The goals are:

- To test the robustness of PGT at a clinical proton accelerator against background and bunch time stability, and examine the factors limiting its applicability and precision.
- To characterise the bunch time structure of the proton beam and its dependence on the energy.
- To analyse if the PGT method is able to detect range variations due to the presence of heterogeneities.
- To estimate the precision of the retrievable range differences as a function of the collected statistics.
- To compare the experimental PGT spectra with simple analytical modelling.
- To assess the mandatory next steps for translation into clinical practice.

Altogether, this work (Hueso González et al., 2015b) aims at exploring the problems and weak points that may arise when a technique proven at a research accelerator is translated into a real medical scenario, and proposes some strategies to circumvent or solve the encountered limitations. In other words, the intention is not to present a final clinically applicable prototype, but rather investigate and mark the way towards it.

3.3 Materials

3.3.1 Detectors

At the Westdeutsches Protonentherapiezentrum Essen (WPE), three monolithic scintillation detectors are used to compare the PGT spectra at different geometries, as well as to check the robustness and compliance of the method. The experimental data are acquired in parallel for all detectors. Their characteristics are summarised in table 3.1.

Table 3.1: Monolithic scintillation detectors available in the PGT experiment at WPE.

Alias	Material	$\varnothing \times$ Length	PMT model	Rise time / ns	Rationale
B1	BaF ₂	[25 : 38] × 30 mm ²	R2059	2 ± 1	Time resolution
B3	BaF ₂	48 × 31 mm ²	R2059	2 ± 1	Time resolution
L0	LaBr ₃ :Ce	2" × 2"	R2083	8 ± 1	Energy resolution

Note: B3 and L0 are cylindrical, whereas B1 is a tapered cone (for optimum time resolution). All PMTs are from Hamamatsu. The rise time refers to the anode signal (50 Ω input impedance).

3.3.2 Electronics

Each scintillation crystal is optically coupled to a PMT, whose type is given in table 3.1. The VME and NIM modular electronics employed in this experiment are similar to those described in subsection 2.4.3. For the B1 and B3 detectors, the anode signal is fed to a Canberra CFD, model 454, for trigger generation, while the dynode signal is shaped and fed to a peak-sensing Analog to Digital Converter (ADC), model V785N. For the L0 detector, the anode signal is amplified and split. One branch is for the CFD, the other for a QDC, model V965. A TDC, model V1290A, monitors the output of the CFD. The energy deposit in the crystal is measured by the QDC or ADC, whereas the γ -ray interaction time is given by the TDC module.

3.3.3 Accelerators

For the verification of the PGT method, an experiment at the WPE, Germany, a clinical proton therapy facility comprising a C230 cyclotron, is conducted. Complementarily, the detector time resolution and time slewing are characterised at the ELBE facility, situated at HZDR, using the same detector set and electronics. The methodology developed for such analysis is published in (Hueso González et al., 2014).

Setup at WPE proton accelerator

The experiment is carried out in the gantry treatment room TR4 of WPE with a pencil beam (no scanning), a single incidence angle (horizontal), and manual control mode. The patient table is aligned to the gantry room isocenter. A target holder mounted on a linear stage with remote control is placed on the patient table, see fig. 3.3 (bottom).

Protons bunched with (105.98 ± 0.09) MHz are shot onto a target, with an energy adjustable between 70 and 230 MeV. Two hollow PMMA half cylinders with an external diameter of 15 cm, an internal of 5 cm, a length of 20 cm and a density of $\rho_{\text{PMMA}} = (1.18 \pm 0.01) \text{ g/cm}^3$ are available. Cylindrical slices of 5 cm diameter and different thicknesses can be inserted into the hollow cavity left inside the two joined half cylinders. Available slice materials are PMMA, bone-equivalent tissue or air (hollow slice). Custom target configurations can thus be constructed by joining slices heterogeneously. The enclosing half cylinders are used to reproduce the therapeutic irradiation conditions concerning neutron production and moderation in surrounding tissue. The spatial dimensions are measured with 0.2 mm precision.

The bone-equivalent material corresponds to SB3 cortical bone, model 450 from Gammex-RMI (Middleton, USA). The measured density is $\rho_{\text{bone}} = (1.809 \pm 0.009) \text{ g/cm}^3$. The electron density, effective atomic number and elemental composition are listed in (Helmbrecht, 2015, appendix A).

Various detectors are arranged at the desired angle and distance, as described in fig. 3.3 (top), to measure the prompt γ -rays exiting from the target. A photograph of the experimental setup is shown in fig. 3.3 (bottom). For a given proton energy, a target is labelled as *full* target if the protons are stopped completely inside it, i.e. if the proton range is smaller than the target thickness.

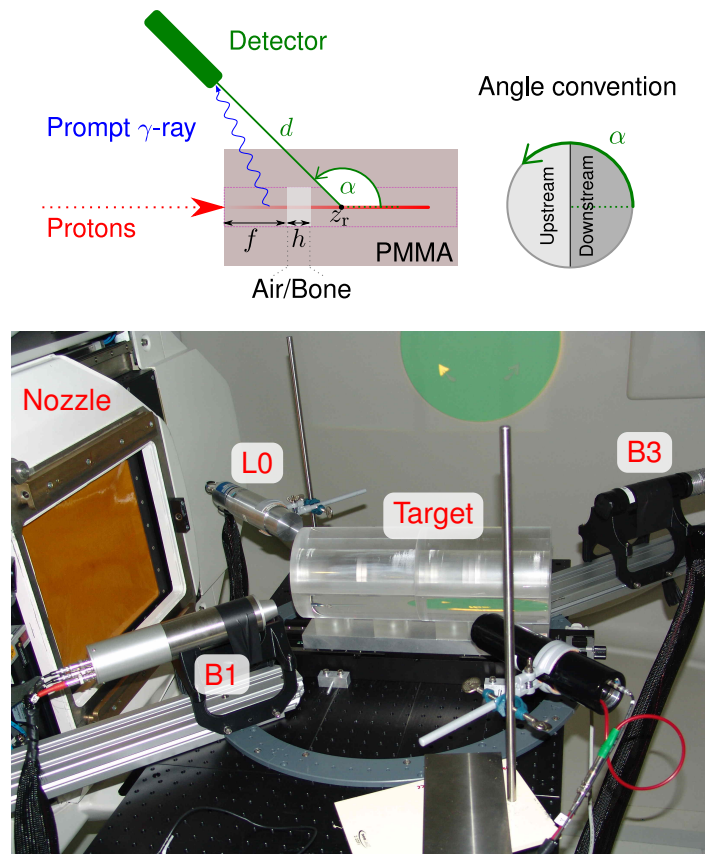


Figure 3.3: Top: schematic sketch of the experimental setup at WPE and the longitudinal cross section of the target. The accelerated protons bunched with 105.98 MHz (corresponding to 9.436 ns separation) collide with the target. As a result of nuclear reactions between the protons and nuclei of the phantom, prompt γ -rays are emitted. These are measured with a monolithic scintillation detector. The PMMA cylindrical target contains a cavity or bone insert of thickness h located at a distance f from the beam entrance point. Bottom: photograph of the experimental setup with three detectors (B1, B3 and L0) at different angles α . The linear stage on the center of the ring holds the two hollow joined half cylinders, in which PMMA, cavity or bone slices can be inserted. The beam incidence is horizontal from the left, where the snout of the nozzle is seen.

The positioning inside the gantry room is based on the built-in laser room system. The pencil beam spot size is measured with an EBT3 gafchromic film from International Specialty Products (Wayne, USA) placed on the front face of the target (from beam point of view). The position of the target with respect to the gantry room isocenter is described in subsection 3.4.4.

3.4 Methods

3.4.1 Detector and module settings

Detectors and electronics settings are chosen according to the energy range of prompt γ -rays that are correlated to the particle range (Verburg et al., 2013), namely higher than 1 MeV and lower than 8 MeV. The detector voltage is adjusted so that the height of the CFD input signal yields around 150 mV when ^{60}Co source photons (1.173 and 1.333 MeV) are detected. The CFD threshold is then set to 1.0 MeV (guided by the calibrated energy spectrum). The zero-crossing is adjusted empirically with a ^{60}Co source by optimising the Coincidence Time Resolution (CTR) with respect to B1 (the reference).

With the same detectors and electronics, an experiment at ELBE is performed in a setup similar to (Hueso González et al., 2014). The goal is to accurately measure the intrinsic detector time resolution and time walk, and apply a time slewing correction retrospectively to the data acquired at WPE.

3.4.2 Proton bunch phase stability

The PGT method is based on the dependence of the prompt γ -ray emission time (or ion transit time) on the particle depth of interaction. Since the protons are bunched with the accelerator RF, it can be used as a time reference for the beam entrance in the target (clock start) if the beam parameters remain stable.

This methodology, a standard in time-of-flight measurements, is successfully applied by (Golnik et al., 2014) for testing the PGT method with a fixed proton energy at the research accelerator AGOR at KVI-CART. However, one has to wonder if this technique is also robust and stable on a longer term at a clinical accelerator.

In every cyclotron, the charged particles are accelerated by a high voltage alternating with the mentioned RF, which must be a multiple of the orbital frequency of the particles in the isochronous electromagnetic field. If this condition is not kept completely stable (Schutte, 1973), the bunches may still be accelerated but not in perfect resonance. This would lead to phase shifts between RF signal and extracted beam bunches, i.e. the PGT spectrum would displace.

To analyse this potential effect in the C230, following experiments are performed in a setup similar to fig. 3.3 (top) with a homogeneous PMMA target at a fixed proton energy:

1. Short PGT spectra of similar statistics are acquired, separated from each other about one hour. The comparison of the, in principle, equivalent spectra can shed light on potential long-term instabilities of the bunch phase relative to the RF .

2. PGT spectra are measured for several (very close) values of the main coil current of the cyclotron. Corresponding variations of the magnetic field change the orbital frequency of the accelerated ions. This is expected to affect (at each turn) the phase slip of particle bunches during acceleration and thus their time correlation at the extraction radius relative to the RF. Potential shifts in the time axis of the associated PGT spectra will quantify the effect of small instabilities of the magnetic field or the accelerator RF, which might be caused by thermal effects (among others).

3.4.3 Proton bunch time structure

The system time resolution is a key parameter for the accuracy of the PGT method, cf. eq. 3.13, that depends on the detector and the beam bunch time structure. Whereas the detector time resolution can be reduced down to 150 ps FWHM with fast scintillation detectors (Hueso González et al., 2015b), a prompt γ -ray width between 1.2 and 2.8 ns FWHM is measured in experiments with a slit gamma camera at clinical accelerators (Verburg et al., 2013). This suggests that a significant contribution to the global system time resolution is the proton bunch time spread.

Such spread is dependent on the proton energy for the C230, as a graphite or beryllium degrader brakes the protons from 230 MeV down to the desired energy. That introduces an additional energy straggling (Clasie et al., 2012) and thus a velocity spread, which translates to a time spread depending on the length of the beam line. Indeed, the experiments are performed in TR4, the farthest treatment room from the cyclotron, which implies the worst case bunch spread. Therefore, the conclusions of this part of the thesis regarding the applicability and robustness of the PGT method are implicitly valid for the remaining rooms.

To characterise the intrinsic bunch time spread (namely at 230 MeV, where the thick degrader is replaced by an aluminium foil), a measurement with a detector in downstream orientation ($-\pi/2 < \alpha < \pi/2$) instead of upstream ($\pi/2 < \alpha < 3\pi/2$) and a thin PMMA target is performed, see fig. 3.3 (top). Note that, for full targets, one cannot overlook the contribution of the proton transit time to the width of the PGT peak. This transit time has the same order of magnitude as the proton bunch spread. The effect of transit time is explicitly discussed in (Biegun et al., 2012; Robert et al., 2013).

The measurement of the bunch time spread is repeated for representative energies covering (to a large extent) the range applied in therapeutic irradiations: 160 and 100 MeV. The effect of the degrader on the time spread is explored. In addition, for the 100 MeV case, a potential reduction of the bunch time spread by changing the settings of the energy selection system is analysed. Namely, the momentum spread limiting slits are closed, a handle which limits the energy spread of the beam after the degrader. With the usual clinical setting, the relative momentum spread dp/p is $\lesssim 0.5\%$.

3.4.4 Systematic measurement program

A systematic measurement program is accomplished for three energies of interest: 100, 160 and 230 MeV. Although the latter is a rather infrequent energy in clinical practice, it has an important research interest, since the bunch time spread is expected to be the lowest and, hence, the upper limit for the precision of the PGT method can be explored.

The nominal energy precision is 0.7 MeV, so that the error of the range in water is below 1.2 mm (Clasie et al., 2012). For the sake of clarity, proton energies refer to those at the exit of the energy selection system. The actual energy at the front face of the target is lower due to losses in the nozzle and beam exit window: (98.2 ± 0.8) , (158.4 ± 0.8) and (227.0 ± 0.9) MeV for the respective initial proton energies of 100, 160 and 230 MeV. The corresponding proton range in a full PMMA target is (6.5 ± 0.1) , (15.1 ± 0.1) and (28.0 ± 0.1) cm.

Three detectors are measured in parallel (individual trigger on each of them). The geometrical arrangement is depicted in fig. 3.3 (bottom), with B1 and L0 in upstream orientation ($\alpha_{B1} = -140^\circ$, $\alpha_{L0} = 140^\circ$) and B3 placed downstream ($\alpha_{B3} = 40^\circ$).

The reference full PMMA target is aligned with 1 mm precision on the linear stage so that, for a given proton energy, half of the particle range lies on the ring center on which the detectors are rotated, cf. fig. 3.2. This way, the emission distribution is in the middle of the field of view of the detectors. The center of the ring is $z_r = (7.5 \pm 0.1)$ cm downstream from the gantry room isocenter ($z = 0$), i.e. to the right in the beam axis, cf. fig. 3.3. Note that d and α are measured with respect to this rotation center z_r , not the room isocenter.

For each proton energy, the following measurement series is performed with the hollow PMMA cylinder and its customisable insertions:

- *Stacked target.* Slices of PMMA are taken out of the full target, so that the protons are not completely stopped inside it. The slices are removed from the back face of the target.
- *Air cavities.* Hollow slices with a thickness h of 2, 5 and 10 mm are inserted at different positions f , as described in fig. 3.3 (top).
- *Bone inserts.* A slice of bone-equivalent material with a thickness h of 20 mm is placed at different positions f .

Another possible experiment, namely the variation of the range by changing the beam energy, is discarded because the relative time offset $t_0(E_0; z_0)$ of the PGT profiles and the bunch time structure $\sigma_{t,\text{bunch}}(E_0)$ are dependent on the proton energy E_0 .

Despite a careful alignment with the room laser system, the spatial accuracy in the target front face position among measurements is estimated to be about 1 mm (statistical), as the upper half cylinder has to be temporarily removed each time a slice is replaced. The error of the detector distance d is 2 mm (systematic), but does not vary in the meantime. The angle

precision is 1° (systematic). The protons impinge the target approximately at the center of the target: this position is verified with two gafchromic films at the target front and back face with 3 mm precision (systematic). For this measurement, the target thickness is smaller than the proton range.

The systematic errors may introduce a constant global offset in all PGT spectra, which has however little importance when comparing PGT measurements with respect to a reference one. Rather, the statistical error of the front face position has a significant influence, as it may shift the leading edge of PGT spectra of consecutive measurements. For example, the theoretical time jitter in the PGT spectrum of a detector (at $\alpha = 140^\circ$ and $d = 30.0$ cm for 100 MeV protons) due to a target positioning error is ~ 10.4 ps/mm, according to the additional proton time of flight ~ 7.8 ps/mm and extra γ -ray time of flight ~ 2.6 ps/mm.

3.4.5 Data acquisition rate

The duration of each measurement of the systematic program described above is around 6 min with a proton current at nozzle exit between 10 and 100 pA. The reason for choosing a beam current far below the clinical values (between 1 and 3 nA) is that the data acquisition with the deployed electronics sustains a maximum throughput of 40 kcps. The detector distance d to the ring center is adjusted between 20 and 60 cm so that, for a given beam current and proton energy, the individual detector trigger rate (above 1 MeV) is $\lesssim 30$ kcps and the system dead time is 50 % at most.

This experiment is intended neither to explore the throughput capabilities nor to provide clinically applicable PGT prototypes, but to acquire spectra in a clinical scenario with enough statistics despite long measurement times and low beam current: around 10^{11} irradiated protons per measurement, which translate to at least $\sim 10^6$ valid γ -ray events per detector (entries in the PGT histogram). Depending on the detector considered, between 10^{-5} and 7×10^{-5} γ -ray events per proton are registered.

3.4.6 Data analysis

All time spectra are corrected according to the time slewing characterisation carried out at the ELBE experiment, see details in (Hueso González et al., 2014).

The PGT spectra are analysed for two different energy filters: between 1.0 and 6.5 MeV (gaining statistics due to multiple characteristic γ -ray lines), and between 3.0 and 5.0 MeV (matching with the pronounced 4.4 MeV line and the corresponding SDEP). In the figure captions, for compactness, these filters are referred to as energy threshold of 1 and 3 MeV, respectively. Please remember that, in all experimental spectra, the energy scale E does not refer to the incident γ -ray energy E_γ , but to the energy deposit L in the detector.

3 Prompt gamma-ray timing

In the offline analysis, the PGT spectra are normalised according to annotated proton charge (from a built-in ionisation chamber used in clinical routine) and system dead time factor. An absolute normalisation is not intended, but rather a relative one among PGT measurements. Therefore, the vertical axis of the histograms is labelled as *Counts* without units. In all PGT spectra, the bin width is 24.41 ps.

Due to the high dynamic system dead time in the VME electronics and parallel operation of several detectors in the same crate, the estimation of the dead time correction factor by the scaler in the electronics is not very accurate: the precision of the (relative) normalisation is not expected to be better than 5% between consecutive measurements.

In some cases, one can correct by eye normalisation fluctuations or phase drifts according to the expected leading edge or maximum value of the PGT spectra. The rationale is to at least compare them qualitatively and illustrate the effect of a stacked target measurement or the presence of heterogeneities. Nevertheless, the quantitative analysis can only be justified with more reliable and accurate measurement tools in upcoming experiments. If present, the illustrative manual correction of normalisation and bunch phase drift will be stated clearly in the figure description.

3.4.7 Modelling of PGT spectra

It turns out that the experimental results, obtained with rather simple target configurations, are well described with a coarse approximation: the simBox model (Golnik et al., 2014). It assumes, for simplicity, a flat spatial emission profile (between target entrance and the particle range) with a scale factor depending on the material: 1, 0.001 and 1.6 for PMMA, air and SB3 cortical bone, respectively. Outside the target region or beyond the range, the emission falls to zero. It should be emphasised that the simBox model is just a transitory tool in the roadmap towards clinical application. The effect of having an oversimplified flat spatial emission profile can surely lead to differences between measurement and model at the falling edge (near the Bragg peak), especially for detectors in downstream direction, whose covered solid angle is maximum for this region of the depth profile. For this reason, the simBox model will only be used in the current work for upstream detectors. The goal is to investigate if range deviations of few millimetres can be seen identified on changes of the timing spectra, and to assess if these shifts are in qualitative agreement (follow the expected trend) with the model. This strategy can give already some hints towards quantitative range retrieval, notwithstanding the need of more reliable models, which are considered a further indispensable step.

3.5 Results

3.5.1 Intrinsic detector time resolution

Table 3.2 summarises the energy resolution and CTR of all detectors as measured with a ^{60}Co source.

Table 3.2: Detector energy resolution and CTR for photons of a ^{60}Co source.

Alias	Energy resolution R_E	$\Sigma_{t,\text{CTR}}$ versus B1
B1	$(9.8 \pm 0.2) \%$	
B3		$(290 \pm 20) \text{ ps}$
L0	$(3.1 \pm 0.1) \%$	$(420 \pm 20) \text{ ps}$

Note: the energy resolution R_E (FWHM) is measured at the 1.173 MeV photopeak. For the B3 detector, the two ^{60}Co photopeaks cannot be resolved. The CTR $\Sigma_{t,\text{CTR}}$ (FWHM) is measured with respect to the B1 detector and an individual CFD threshold of 1.0 MeV.

The result of the intrinsic detector time resolution, measured at the ELBE accelerator as a function of the photon energy, is shown in fig. 3.4. The electronic resolution (precision of the time stamp) with which the ELBE RF is measured, $(90 \pm 10) \text{ ps}$ (FWHM), is already subtracted.

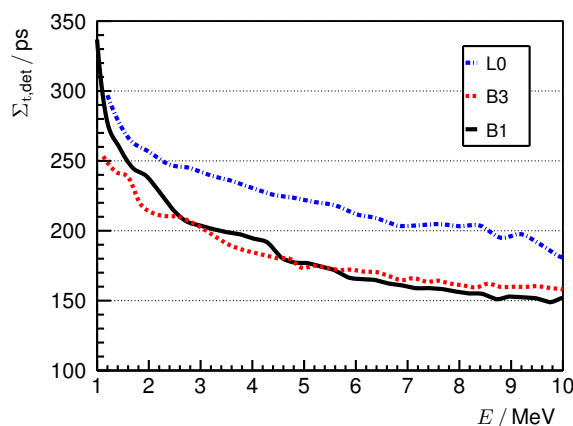


Figure 3.4: Intrinsic time resolution $\Sigma_{t,\text{det}}$ (FWHM) of the L0, B3 and B1 detectors, measured at the ELBE bremsstrahlung beam as a function of the energy deposit E . CFD threshold level corresponds to about 1.0 MeV. The electronic resolution of the RF, i.e. the precision of the time reference, is already subtracted.

3.5.2 Illustrative energy over time spectra

Fig. 3.5 shows three illustrative cases of energy over time spectra for 230 MeV protons. In (a), corresponding to an upstream detector with excellent energy resolution (L0), clear prompt γ -ray lines are distinguished corresponding to 6.1 MeV and 4.4 MeV, as well as their SDEP. In addition, the time uncorrelated γ -ray line of neutron captures on hydrogen is

3 Prompt gamma-ray timing

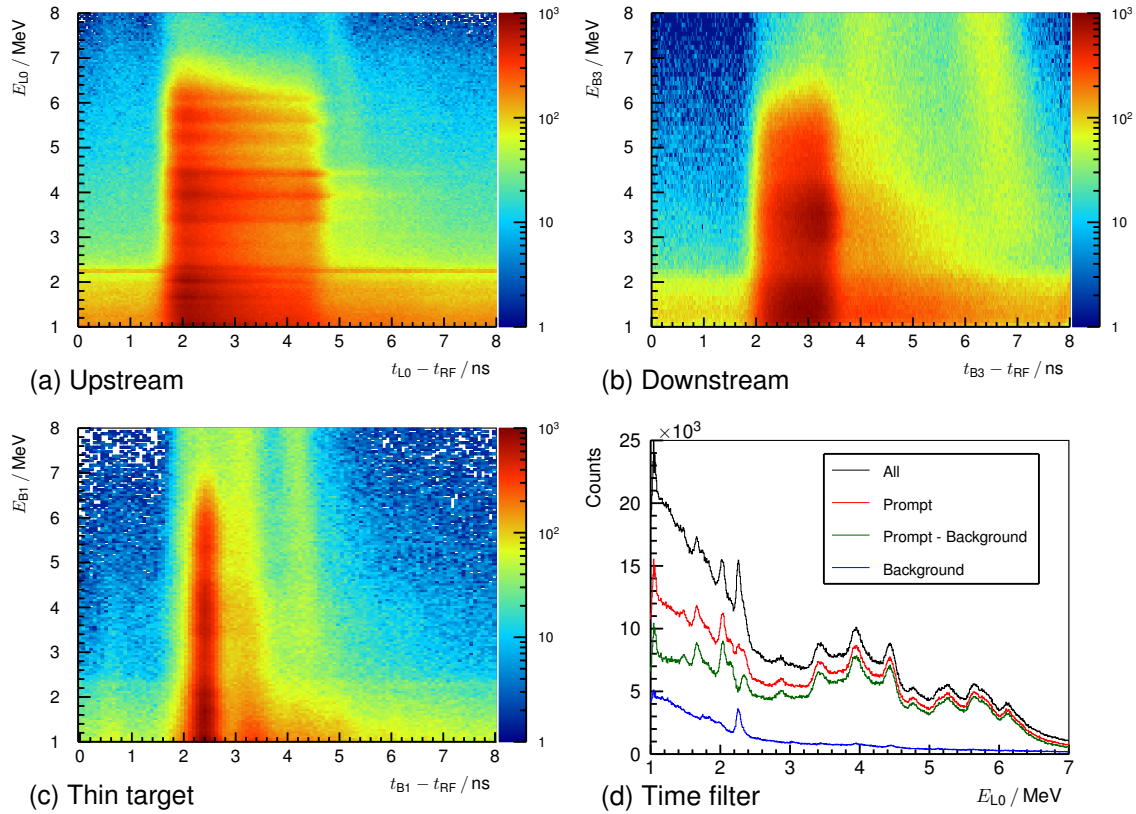


Figure 3.5: (a) Energy over time spectrum of the L0 detector at $\alpha = 140^\circ$, $d = 30.0$ cm and a homogeneous full PMMA phantom. (b) Analogous spectrum for the B3 detector at $\alpha = 40^\circ$, $d = 30.0$ cm. (c) Spectrum of the B1 detector at $\alpha = -140^\circ$, $d = 20.0$ cm with a thin PMMA target. In all cases, the proton energy is 230 MeV and the color scale refers to the number of collected counts. (d) Detector response energy spectra obtained based on the projections of graph (a) for different regions (time filters). *All* (black) refers to no time filter, *Prompt* (red) to a selection between 1.5 and 4.8 ns, *Background* (blue) to the complementary region, *Prompt - Background* (green) to the subtraction of the two last. Each projection is rescaled according to the size of the time filter relative to the full time period.

identified at 2.2 MeV (horizontal line). Conversely, (b) evinces a more compressed PGT distribution, no energy-resolved γ -ray lines (B3 has worse energy resolution) as well as a considerable increase of background. The bump located at [4 to 6 ns; 1 to 4 MeV] may be related to fast neutrons (secondary γ -rays), whereas the vertical structure at [~ 7 ns; 3 to 8 MeV] could be associated with scattered protons leaving the target. (c) corresponds to a thin PMMA target, and vertical structures due to scattered particles are also visible.

The reason behind the stretching or compression of PGT profiles for full targets is the angle α : for downstream detectors, the protons and γ -rays fly both downwards, and the γ -ray time of flight (distance l_γ) to the detector for the entrance point is larger than for the stopping point $l_\gamma(z_0) > l_\gamma(z_{\max})$, cf. eq. 3.9. This reduces the spread of arrival times at the detector and compresses the emission time spectrum. On the contrary, for upstream detectors, the γ -rays travel backwards, in opposite direction to the protons. The γ -ray time of flight is larger at the

stopping point than at the entrance point $l_\gamma(z_0) < l_\gamma(z_{\max})$, and the emission time spectrum is stretched. For $\alpha = 90^\circ$ and large d , all γ -rays need the same time of flight to the detector $l_\gamma(z_0) \approx l_\gamma(z_{\max})$, and the PGT spectrum reflects just the emission time distribution.

Fig. 3.5 (d) shows the projection of graph (a), corresponding the detector energy response of the L0 detector, for different time regions. One can identify a continuous background and the 2.2 MeV γ -ray line of neutron captures on hydrogen (no time correlation with the beam). The prompt component shows a continuous distribution (also due to incoherent scattering) and several characteristic γ -ray lines together with the SDEP. The subtraction of the background allows to resolve a peak close to the 2.2 MeV line and illustrates the importance of time of flight information in the PGI field (Biegun et al., 2012).

3.5.3 Proton bunch phase stability

The PGT spectra shown in fig. 3.6 (left) correspond to independent measurements with the B3 detector at $\alpha = 40^\circ$, for 230 MeV protons impinging a full homogeneous PMMA target. The mean value of the depicted distributions is shown in fig. 3.6 (right). There is an evident drift of the PGT spectrum on a long time scale: the mean value shifts around 400 ps in a time span of four hours. Albeit a constant detector location, target position and proton energy, the PGT spectrum is not stable. The origin of this deviation is attributed to the phase shift of the proton bunch with respect to the RF signal.

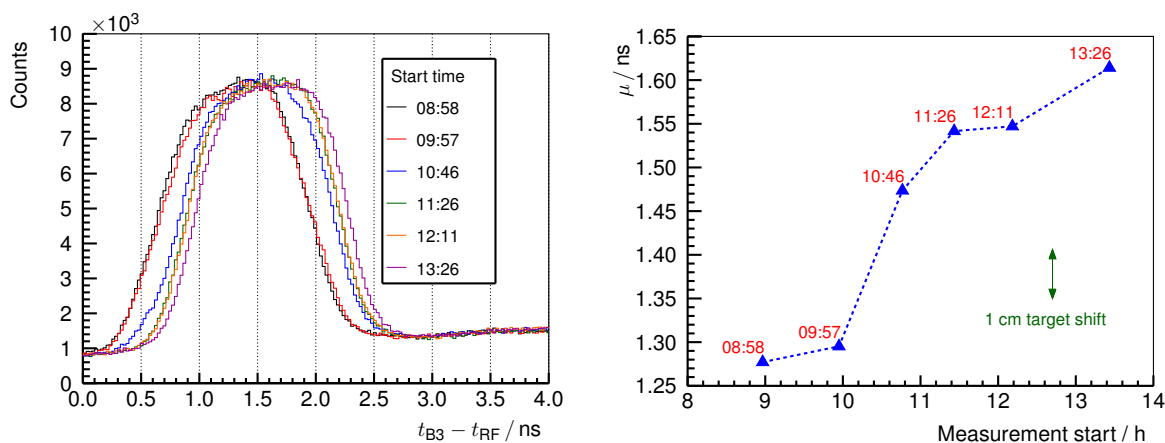


Figure 3.6: Left: PGT spectra of the B3 detector at $\alpha = 40^\circ$, $d = 60.0$ cm, a homogeneous PMMA target and a proton energy of 230 MeV. Independent redundant measurements of about 5 min duration with a separation of around one hour are overlaid. Spectra are normalised to the number of protons (obtained from the measured charge and considering the system dead time correction). Energy threshold is 1 MeV. Right: mean value μ of the PGT distributions. The green arrow illustrates the PGT effect corresponding to a 1 cm target shift.

The results of the complementary experiment to analyse the stability of the bunch phase with respect to the RF when slightly varying the cyclotron main coil current are shown in fig. 3.7 (left). The dependence of the mean value of the distribution on the magnet current

3 Prompt gamma-ray timing

is plotted in fig. 3.7 (right) and is more or less linear in this range: a shift of about 14 ps/mA at an average current of ~ 740 A is measured. This reflects the extremely high sensitivity of the PGT spectrum mean value to cyclotron instabilities: relative current variations of one per million result in measurable center of gravity shifts and thus affect or limit the long-term precision of the PGT method in the absence of a bunch phase monitor.

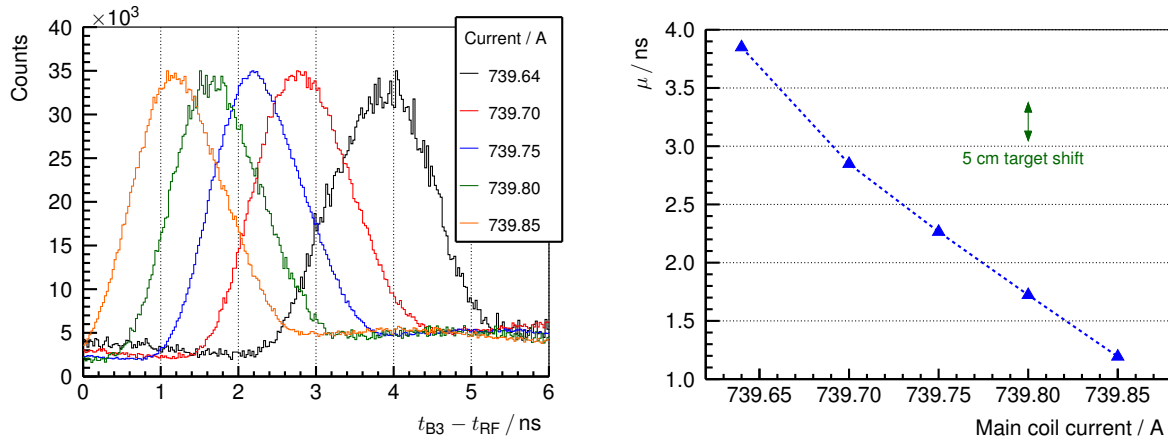


Figure 3.7: Left: PGT spectra of the B3 detector at $\alpha = 40^\circ$, $d = 45.0$ cm, a full homogeneous PMMA target and a proton energy of 160 MeV, for different values of the main coil current of the cyclotron (detailed in the legend). Spectra are normalised to their respective maximum. Energy threshold is 1 MeV. Right: mean value μ (Gaussian fit with linear background) of the PGT distributions. The green arrow illustrates the PGT effect corresponding to a 5 cm target shift. The blue dashed line is just a subsidiary line connecting the points.

3.5.4 Proton bunch time structure

In fig. 3.8 (left), the dependence of the bunch width on the proton energy is demonstrated indirectly when measuring the prompt γ -rays produced in a thin homogeneous target. The presence of a tail right from the main peak of the spectra is related to secondary charged particles, mainly protons backscattered at ^{12}C and ^{16}O nuclei of the PMMA target. Thus, delayed but correlated background is generated (see fig. 3.5c). This is not suppressed despite the increase of the γ -ray energy threshold to 3 MeV for fig. 3.8 (statistics are not critical in this case). For thicker targets, this background is also present but has a lower relative intensity compared to the prompt γ -ray production.

The bunch time spread, detailed in table 3.3, is measured with different detectors by determining the FWHM Σ_t of the PGT distributions and subtracting the proton transit time as well as the intrinsic detector and RF time resolution.

Fig. 3.8 (right) shows the resulting bunch time spread at 100 MeV for different values of the momentum slit, see subsection 3.4.3. All measurements of the systematic program, see subsection 3.5.5, are done with a momentum slit opening of 25 mm, i.e. the usual clinical setting.

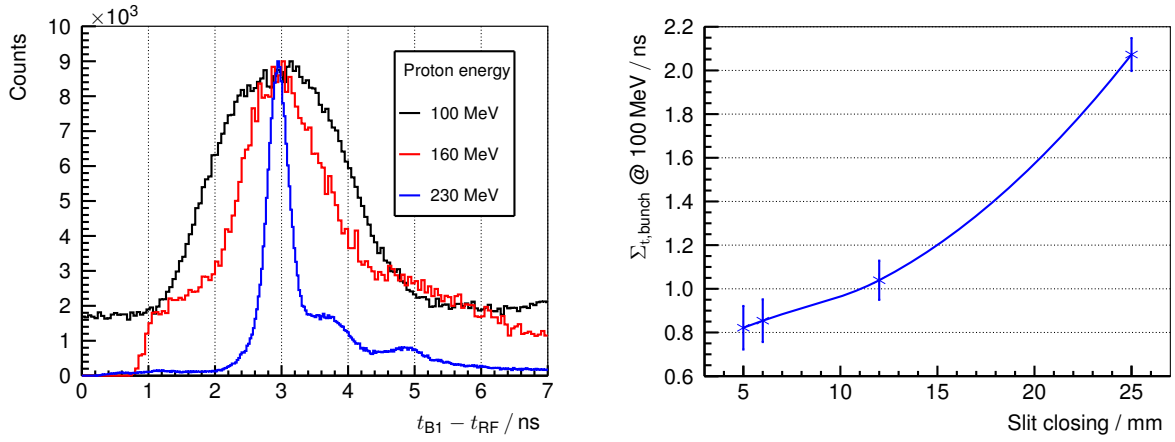


Figure 3.8: Left: PGT spectra of the B1 detector at $\alpha = -140^\circ$, $d_{100\text{ MeV}} = 30.0\text{ cm}$, $d_{160\text{ MeV}} = d_{230\text{ MeV}} = 20.0\text{ cm}$, with a thin PMMA target (10 mm) for three different proton energies and the usual slit closing (25 mm) at the WPE gantry TR4. Spectra are normalised to their respective maximum and shifted in time to match their centroids for correcting the different proton time of flight to the target. Energy threshold is 3 MeV. Right: bunch time spread $\Sigma_{t,\text{bunch}}$ (FWHM after numerical background subtraction) at 100 MeV proton energy as a function of the closing of the momentum spread limiting slits. The measurements correspond to a full PMMA target and the B3 detector at $\alpha = 40^\circ$, $d = 60.0\text{ cm}$. γ -ray energy threshold is 3 MeV. Proton transit time as well as RF and detector time resolution are already subtracted.

Table 3.3: Proton bunch time spread $\Sigma_{t,\text{bunch}}$ at the gantry TR4 of the WPE facility for the B1, B3 and L0 detectors and three proton energies.

Alias	100 MeV	160 MeV	230 MeV
B1	$(2.1 \pm 0.2)\text{ ns}$	$(1.3 \pm 0.1)\text{ ns}$	$(310 \pm 30)\text{ ps}$
B3	$(2.1 \pm 0.1)\text{ ns}$	$(1.0 \pm 0.2)\text{ ns}$	$(380 \pm 50)\text{ ps}$
L0	$(2.1 \pm 0.2)\text{ ns}$	$(1.2 \pm 0.2)\text{ ns}$	$(300 \pm 40)\text{ ps}$

Note: [$\alpha_{\text{B1}} = -140^\circ$, $d_{\text{B1}} = 20.0\text{ cm}$, $d_{\text{B1},100\text{ MeV}} = 30.0\text{ cm}$], [$\alpha_{\text{B3}} = 40^\circ$, $d_{\text{B3}} = 60.0\text{ cm}$, $d_{\text{B3},160\text{ MeV}} = 45.0\text{ cm}$], [$\alpha_{\text{L0}} = 140^\circ$, $d_{\text{L0}} = 30.0\text{ cm}$]. The usual slit closing (25 mm) is set up for the experiments. A prompt γ -ray energy threshold of 3 MeV is applied. The time spread $\Sigma_{t,\text{bunch}}$ refers to the FWHM of the timing distributions after subtraction of proton transit time, intrinsic detector time and RF resolution.

3.5.5 Systematic measurement program

230 MeV proton energy

Stacked target. Fig. 3.9 (left) evinces the potential of the PGT method at 230 MeV compared to 160 or 100 MeV due to the very low bunch time spread, see fig. 3.8 (left). Individual characteristics can be identified along the spectrum shape, instead of focusing on the distribution momenta, as done in the experiment at the AGOR accelerator (Golnik et al., 2014).

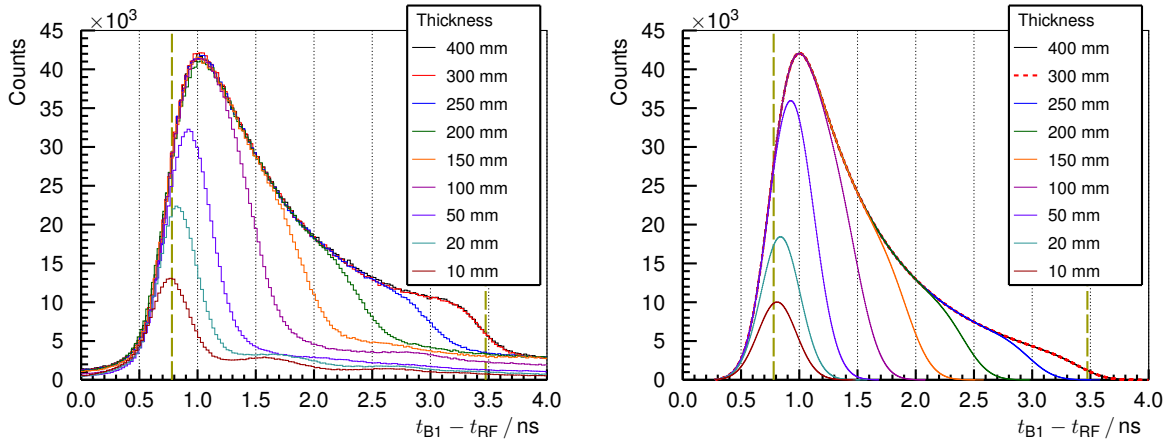


Figure 3.9: Left: experimental PGT spectra of the B1 detector at $\alpha = -140^\circ$, $d = 20.0$ cm, for 230 MeV protons and different PMMA target thicknesses (listed in the legend). Spectra are normalised according to dead time and charge and retuned within a 5% error margin for illustrative purposes. In addition, the bunch phase shift is corrected to match all leading edges of the spectra. Energy threshold is 1 MeV. Right: spectra calculated with the simBox model. The time offset relative to experiment is adjusted manually. Both: the two vertical dashed lines refer to the expected target front face and proton range positions.

In the case of the full PMMA target, the proton stopping point is at 28.0 cm depth. A smooth leading edge is identified in the PGT spectrum, which is associated to the front face of the target (beam entrance point). A trailing edge related to the distal fall-off is found, but with lower relative intensity. Despite the increased γ -ray production rate expected within the Bragg peak, the measured profile does not reproduce it directly due to the following factors:

- Solid angle effects for upstream detectors, i.e. the Bragg peak is much farther away than the entrance point.
- Larger path through PMMA (attenuation) for the prompt γ -rays emitted at the distal edge.
- Transformation among measured time, γ -ray emission time and nuclear interaction depth. As the velocity of the particle is not constant, the conversion from space to time is not linear and the histogram is stretched over more time bins close to the Bragg peak (slowest proton) than at the beam entrance point (fastest).

An example of a spatial emission profile through backward calculation, which compensates for all these factors, is shown later on for the full target case (thickness > 280 mm), cf. fig. 3.11 (right; $f = 0$ mm; $h = 0$ mm).

The removal of a slice from the rear face of the target links to a decrease in the area and shift to the left in the mean value of the PGT distribution over the whole thickness range studied (except for the 400 mm case). For the thinner targets (thickness ≤ 50 mm), the reduction in the area correlates with a decrease of the maximum of the curve, since the proton transit time effect has the same order of magnitude as the system time resolution. Conversely, for the thicker targets, the effect of removing a slice can be clearly identified as a decrease of the prompt γ -ray production at a given depth, which changes the right leaf of the distribution but not the maximum. Comparing the 300 and 400 mm cases, no change at all is observed. This confirms the intuitive idea that adding material beyond the particle range (280 mm) does not have any effect on the PGT profiles, as the protons are completely stopped at equal depth in both cases, and the region of prompt γ -ray production is identical.

Fig. 3.9 (right) shows the PGT distributions calculated with the simBox model. The general shape along the time axis is reproduced. However, near to the right fall-off, the model fails to incorporate the rectangular edge of the 300 and 400 mm targets, in which the protons stop completely. This is because the simBox model underestimates the γ -ray production rate close to the Bragg peak. Furthermore, the background is not included in the model.

Air cavities. An extensive study about air cavities of different thicknesses and locations inside the full PMMA target is accomplished for 230 MeV protons, as shown in fig. 3.10. Comparing the PGT spectra, one can visually identify a deficit in the γ -ray production of a magnitude correlated to the cavity thickness and at a time position linked to its location, as well as a shift to the right in the position of the trailing edge (overshoot). Air cavities and thus range differences down to 2 mm can be retrieved with the gathered statistics and without any sophisticated numerical analysis. Similar spectra are measured with the B1 detector.

These experimental spectra are in significant agreement with the modelled ones, if the region near the Bragg peak is excluded. The centroid of the cavity, namely the time point with the largest deficit in counts with respect to the homogeneous case, is depicted in fig. 3.12 (left) for different locations f of the 10 mm cavity. The values expected by the simBox model are in reasonable agreement with the experimental ones.

Bone inserts. A bone-equivalent slice of $h = 20$ mm thickness is inserted at different locations inside a PMMA target for 230 MeV protons. The PGT distributions measured with the L0 detector are shown in fig. 3.11 (left). The bone insert correlates evidently with an increase of the prompt γ -ray production with respect to the homogeneous case at the bone location. Moreover, a shift to the left in the falling edge (undershoot) is visible. These effects are basically attributed to the higher density of bone with respect to PMMA. Hence, an 8 mm

3 Prompt gamma-ray timing

range shift, according to stopping power data (Berger et al., 2005), due to a bone heterogeneity can be at least retrieved with the collected statistics. Note that the measurement at $f = 269$ mm depth is a special case, as the proton stopping point is inside the bone insert.

Fig. 3.11 (right) shows a tentative conversion of PGT spectra to depth profiles after corrections for solid angle effects, attenuation, γ -ray time of flight and transformation of time to space, see backward calculation in subsection 3.1.4. In other words, a simple BP is applied to recover the depth profile information from the experimental data. Note that an iterative background subtraction algorithm (Ryan et al., 1988) is applied. However, at this stage, the time origin t_0 is elected arbitrarily and a deconvolution with the system time response is not applied, which explains the absence of a sharp leading edge at $z = 0$.

For all bone insert measurements (the special case at 269 mm aside), the trailing edge is (7 ± 2) mm left from the homogeneous phantom, while the expected range difference is ~ 8 mm. It is worth pointing out that the a priori assumption of the target geometry, stopping power, election of t_0 and time to space conversion curve predetermines (biases) the respective position of the falling edge in fig. 3.11 (right).

The centroid of the bone, namely the space point with the largest surplus in counts with respect to the homogeneous case, is depicted in fig. 3.12 (right) for all locations f of the $h = 20$ mm insert. The values expected by the simBox model are in considerable agreement with the experimental ones.

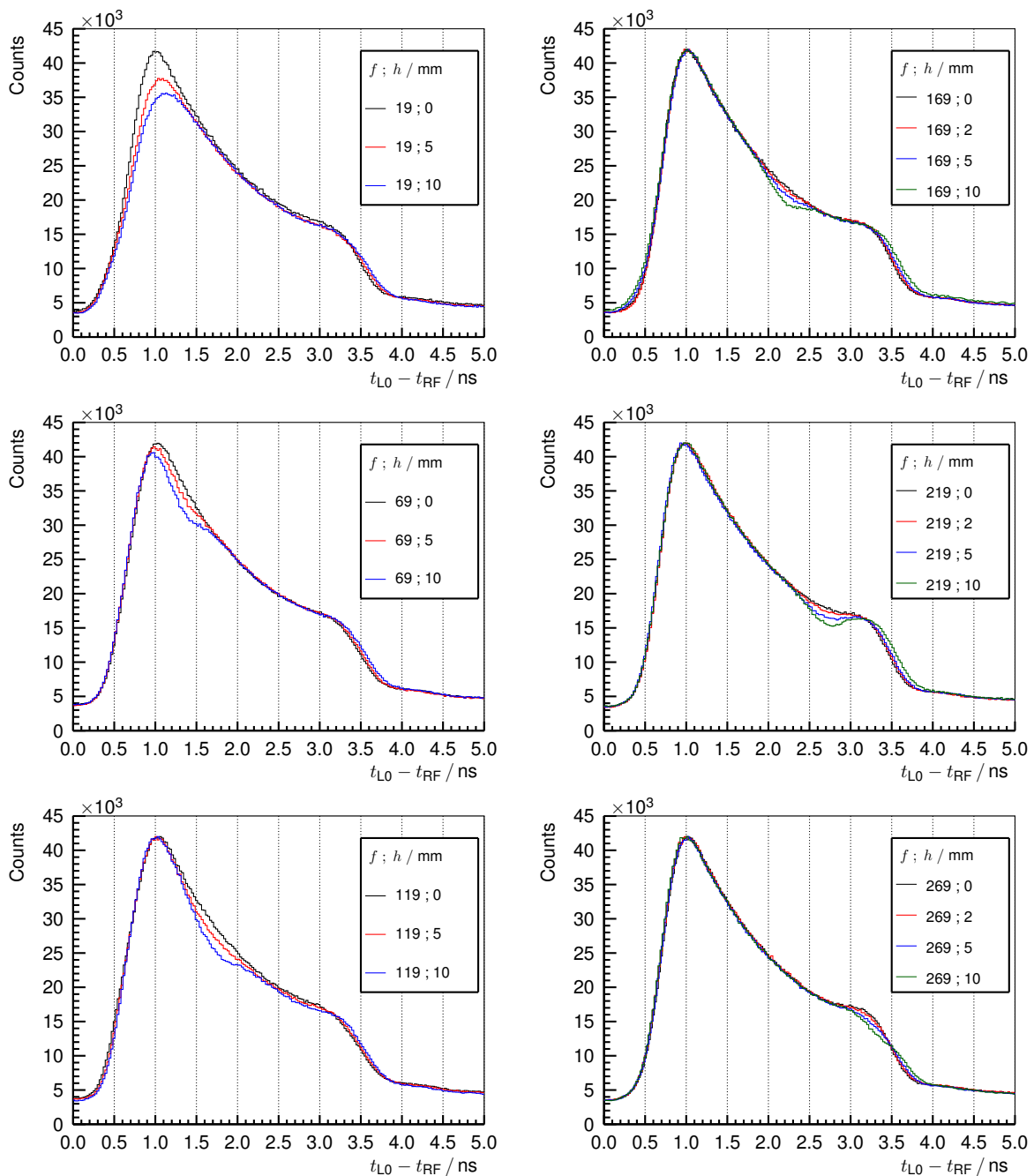


Figure 3.10: Experimental PGT spectra of the L0 detector at $\alpha = 140^\circ$, $d = 30.0$ cm, for 230 MeV protons and different air cavities inside the full (400 mm) PMMA target at $f ; h$ (front face position; thickness) as described in fig. 3.3 (top). Spectra are normalised to charge and dead time (first two graphs of left column) or to their respective maximum (other graphs). Distributions are shifted in time to match their leading edges: at $\sim 50\%$ of the rise except for all figures except for the top left one, which is at 10% of the maximum as the cavities close to the front face of the target affect the 50% level. Energy threshold is 1 MeV.

3 Prompt gamma-ray timing

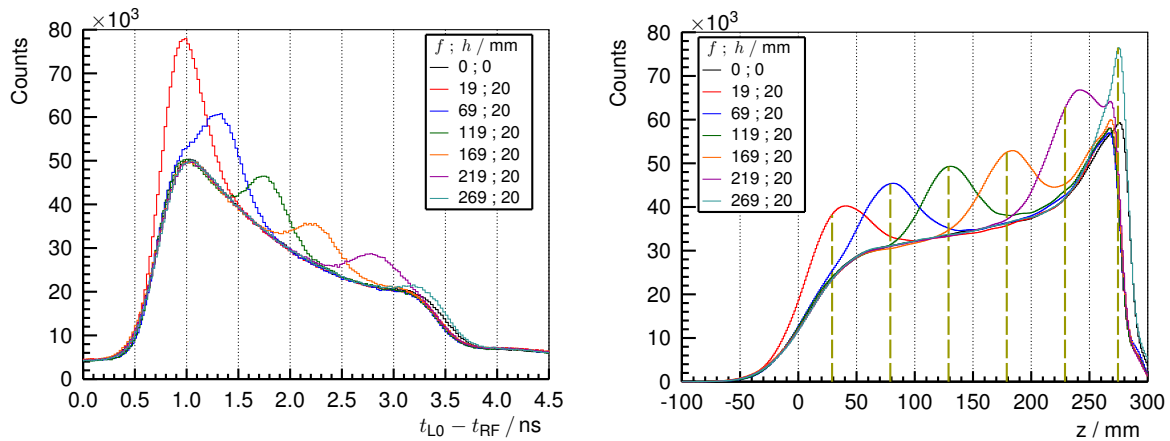


Figure 3.11: Left: experimental PGT spectra of the L0 detector at $\alpha = 140^\circ$, $d = 30.0$ cm, for 230 MeV protons and a bone insert inside the full (400 mm) PMMA target at $f ; h$ (front face position; thickness) as described in fig. 3.3 (top). Spectra are normalised according to dead time and charge, whereas phase drift is corrected manually to match all leading edges. Energy threshold is 1 MeV. Right: time to distance conversion from the left PGT spectra after application of stopping power, sensitivity and γ -ray time of flight corrections, as well as background subtraction. z refers to the depth with respect to the front face of the target (beam entrance point). Vertical dashed lines mark the centroid of the bump according to the simBox model.

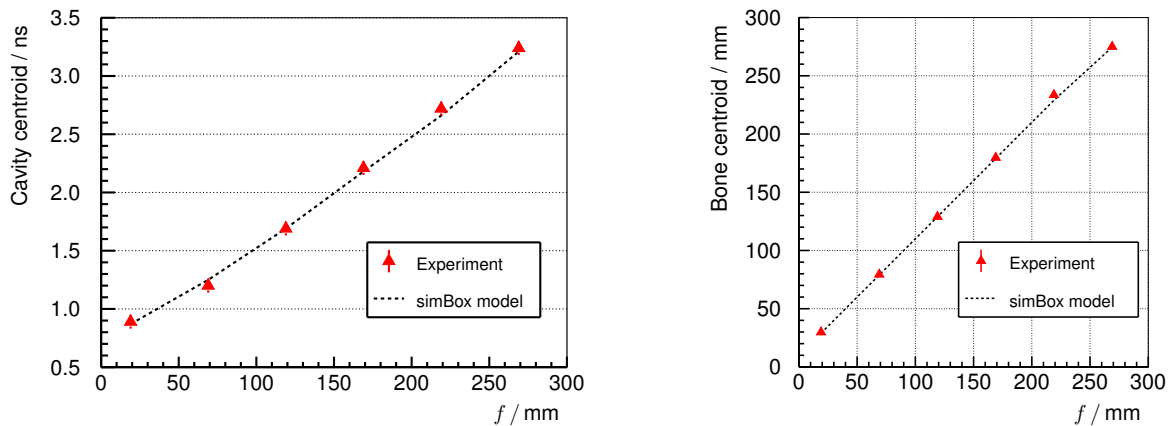


Figure 3.12: Left: measured time position (centroid of the deficit) of a $h = 10$ mm cavity at different distances f from the PMMA target front face, corresponding to the PGT spectra of fig. 3.10 (L0 detector). The experiment is compared to the values expected according to the simBox model. The relative time offset is adjusted empirically. Right: measured spatial position (centroid of the surplus) of a $h = 20$ mm bone insert at different distances f from the PMMA target front face with the L0 detector, corresponding to the converted spectra of fig. 3.11 (right). The experiment is compared to the values expected according to the simBox model.

100 MeV proton energy

Stacked target. For the stacked target experiment at the WPE accelerator, cf. fig. 3.13 (left), analogous to that at the AGOR facility (Golnik et al., 2014), one can identify a shift to the right in the peak centroid correlated to the target thickness, as well as an increase in the prompt γ -ray production (area under the curve). Compared to fig. 3.9, the PGT profile is highly blurred due to the much larger bunch time spread at 100 MeV (see table 3.3). Nonetheless, one can rely on the analysis of distribution momenta, which retain essential information about the proton range.

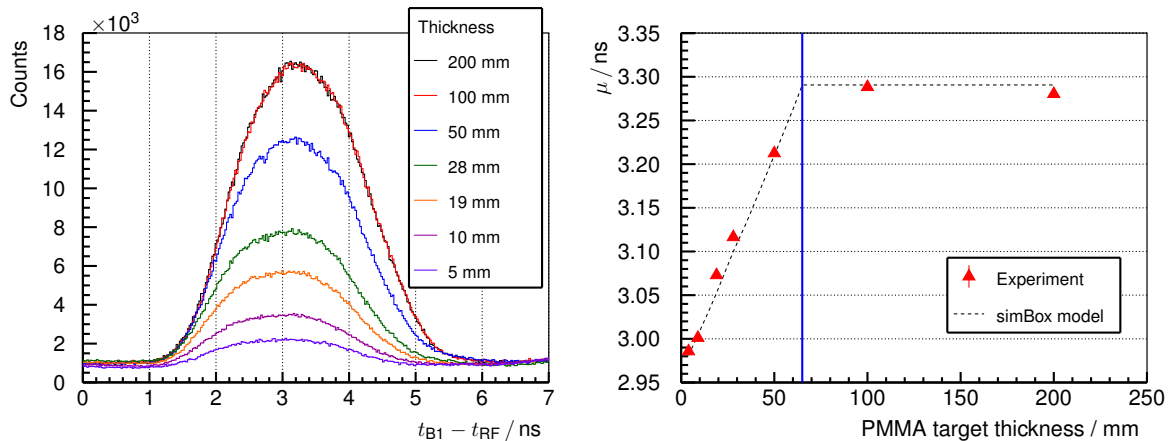


Figure 3.13: Left: PGT spectra of the B1 detector at $\alpha = -140^\circ$, $d = 30.0$ cm, for 100 MeV protons and different PMMA target thicknesses (listed in the legend). Spectra are normalised according to dead time and charge. Energy threshold is 1 MeV. Right: mean value μ (center of gravity after numerical background subtraction) of the PGT distributions over the target thickness. The experimental data are compared to the values predicted by the simBox model. The blue vertical line marks the range of 100 MeV protons in a full PMMA target (65 mm).

Fig. 3.13 (right) evinces the linear relationship between centroid and target thickness until a saturation or plateau is reached, i.e. when the protons are already completely stopped (proton range is 65 mm). As in (Golnik et al., 2014), a reasonable agreement between modelling and experiments is found. When fitting the slope of the left part of the graph, (5.1 ± 0.1) ps/mm are obtained for the experiment versus (5.03 ± 0.03) ps/mm for the simBox model. Note that the election of the global time offset in the experiment relative to the model is arbitrary. The value maximising the agreement with all experimental points is selected.

Fig. 3.14 (left) shows the energy spectra for different target thicknesses, normalised according to dead time and charge. One can see the increase of integral over the distribution the thicker the target. Fig. 3.14 (right) shows this integral as function of the thickness and compares it with the values from the simBox model. The trend is similar, but there is a disagreement for the full targets, probably due to the underestimation of the prompt γ -ray production at the Bragg peak, which is not included in the simBox model.

So far, the forward quantitative analysis is used in figs. 3.9 (right) and 3.12 (left), and the backward calculation in figs. 3.11 (right) and 3.12 (right), methods which are detailed in sub-

3 Prompt gamma-ray timing

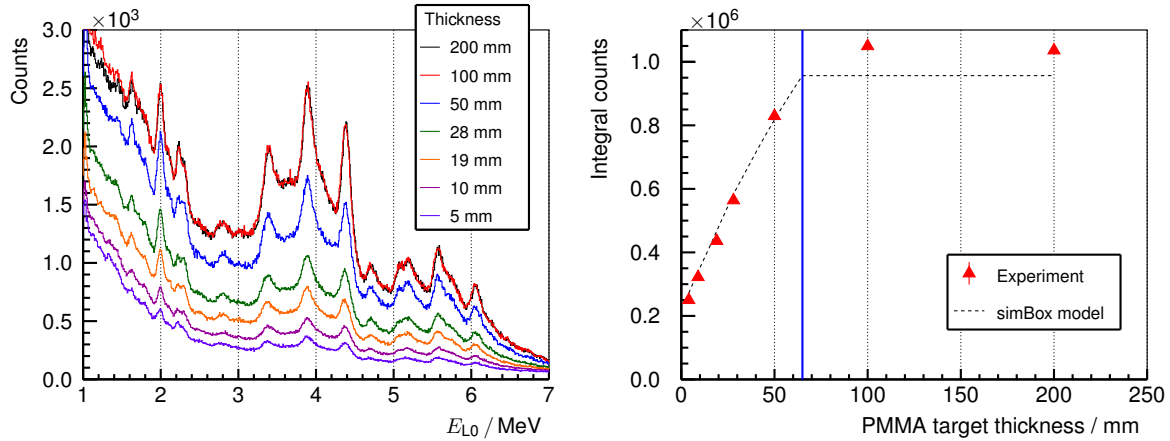


Figure 3.14: Left: response energy spectra of the L0 detector at $\alpha = 140^\circ$, $d = 30.0$ cm for 100 MeV protons and different PMMA target thicknesses (listed in the legend). Spectra are normalised according to dead time and charge. No time filter is applied. Right: integral of the spectra of left figure between 1 and 7 MeV versus the target thickness. The experimental data are compared to the values predicted by the simBox model after empirical adjustment of background offset and relative scale factor. The blue vertical line marks the range of 100 MeV protons in a full PMMA target (65 mm).

section 3.1.4. For the stacked target experiment at 100 MeV proton energy, the third variant is tried: the parametric reconstruction. The parameter λ is in this case the target thickness (width of the simBox profile) and the χ^2 test is minimised with respect to it. Fig. 3.15 (left) shows the experimental spectrum (black line) after background subtraction for a 9.5 mm thick PMMA target, compared to the modelled spectra for different values of λ in 1 mm steps. Although it may seem so at first glance, note that the amplitude of the modelled curves is not a free parameter. The height of the simBox profile is a fixed value for all curves, just its width λ is increased. This leads to a broader γ -ray emission range, and thus a larger area and amplitude after convolution with the system response, as well as a distinct shape.

Fig. 3.15 (right) shows the respective χ^2 tests: the curve exhibits a minimum for a value λ_{\min} that is close to the actual thickness. It is evident that the larger the statistical sample, the more precise one is able to determine the minimum of the curve and thus the particle range (systematic errors due to the assumed model aside). Note that the experimental shape of the PGT spectrum is not perfectly reproduced by the simBox model due to the oversimple spatial emission profile and, presumably, the non-Gaussian bunch time structure. The complete procedure is repeated for all PGT spectra of fig. 3.13 and the reconstructed parameter λ_{\min} is compared to the actual target thickness, cf. fig. 3.16.

Air cavities. The influence of tissue heterogeneities is illustrated in fig. 3.17 (left): air cavities of different thicknesses are inserted at a fixed position inside the full PMMA target. On the one hand, the spectrum maximum decreases with increasing cavity thickness. On the other hand, the falling edge of the distribution shifts slightly to the right as a consequence of the overshoot. Thus, at least 5 mm range differences can be distinguished at 100 MeV

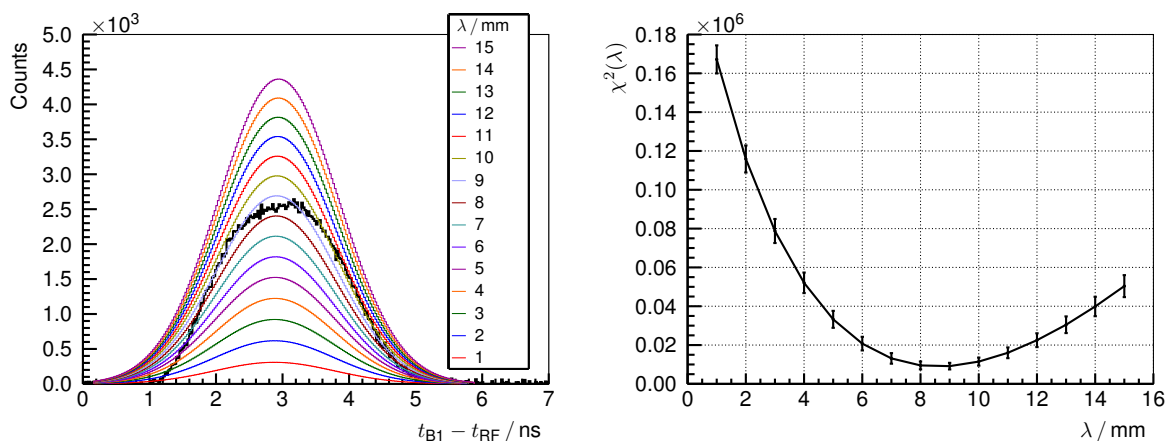


Figure 3.15: Left: experimental PGT spectrum (black line) of the B1 detector at $\alpha = -140^\circ$, $d = 30.0$ cm, for 100 MeV protons and a 9.5 mm thick PMMA target. Normalisation and energy threshold is as in fig. 3.13. Background subtraction is applied. The simBox model with the parameter λ as the width of the box is used to calculate analytical PGT spectra in 1 mm steps, cf. legend. Relative time offset and normalisation of the simBox spectra are adjusted empirically for one independent measurement and applied here. Right: χ^2 test between experimental and modelled spectra of the left plot for the different values of λ . A connecting line is drawn as visual help.

with the gathered statistics and without any further numerical algorithm. The shift to the right in the centroid of the distribution for the 5 mm cavity is (28 ± 1) ps for the experiment and (27.1 ± 0.2) ps for the simBox model. For the 10 mm cavity, the experimental shift with respect to the homogeneous case is (65 ± 2) ps versus (53.6 ± 0.2) ps for the model.

Bone inserts. Fig. 3.17 (right) compares a full target PGT spectrum to the case with a 20 mm bone insert at 29 mm depth. The distributions are normalised to their respective maximum, otherwise (when normalised to dead time and charge) the higher amount of γ -rays produced in the heterogeneous case leads to a much taller spectrum (red line) and shadows the comparison of the trailing edge with respect to the homogeneous (black line). The conclusion is that a bone insert increases the γ -ray production rate as well as decreases the width of the time distribution due to the undershoot effect, ~ 8.5 mm range difference according to stopping power data (Berger et al., 2005). This results in an earlier average detection time of the prompt γ -rays. The shift to the left in the centroid of the distribution with respect to the homogeneous case is (28.6 ± 0.6) ps for the experiment and (17.9 ± 0.4) ps for the simBox model.

3 Prompt gamma-ray timing

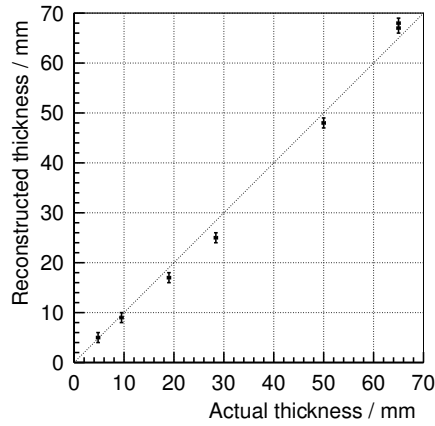


Figure 3.16: Comparison of reconstructed thickness (λ_{\min}) to actual thickness for all measurements of fig. 3.13. The parametric reconstruction is described for a single measurement in fig. 3.15. Note that for the measurements corresponding to 100 and 200 mm PMMA thicknesses, the protons stop completely inside the target. Hence, the respective points of the graph are moved to the *effective* thickness of 65 mm (the expected proton range). A diagonal grid line marks the ideal distribution of the points.

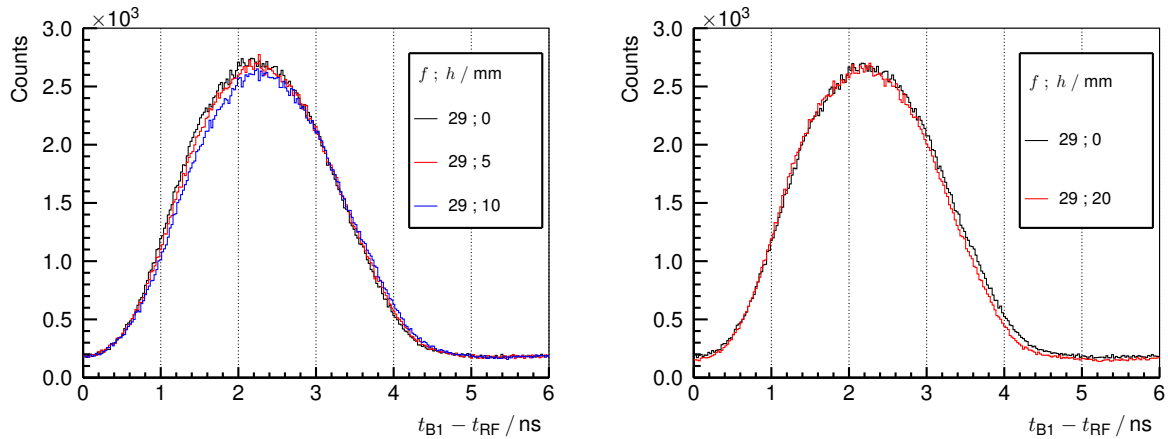


Figure 3.17: Left: PGT spectra of the B1 detector at $\alpha = -140^\circ$, $d = 30.0$ cm, for 100 MeV protons and different air cavities inside the full (200 mm) PMMA target at $f ; h$ (front face position; thickness) as described in fig. 3.3 (top). Spectra are normalised according to dead time and charge. Energy threshold is 1 MeV. Right: equivalent settings, but a single bone insert instead of an air cavity. Spectra are normalised according to their respective maximum.

3.6 Discussion

Motivation. A main purpose of the present experiment is the estimation of the minimum range difference that generates a measurable change in the shape of the PGT spectrum, rather than the quantitative retrieval of the range. The setup is optimised for timing but is not intended for high rate measurements or long-term detector gain stability. This is considered as a further step once the suitability of PGT in clinical environments is shown at all.

The presented PGT spectra corresponding to different proton energies and targets illustrate the feasibility of range assessment for clinical pencil beams based on this novel and simple approach. It relies on a compact fixed monolithic detector setup, with low footprint in a gantry treatment room and at minimum expense.

Systematic program. Proton range variations due to a stacked PMMA target as well as cavity and bone heterogeneities are detected. In most cases, an energy threshold of 1 MeV is applied to the data for maximising the statistics, despite the fact that the correlation of the γ -ray emission profile with the dose is higher for an energy threshold of 3 MeV (Verburg et al., 2013). For 100 MeV proton energy, range differences of five millimetres can be successfully retrieved (without any sophisticated numerical analysis). These are identified qualitatively based on the distinctness of the spectra compared to the homogeneous case. The quantitative assessment relies on the comparison of distribution momenta between experiment and simBox model, with overall reasonable agreement. There are some systematic deviations in certain cases, either due to bunch-to-RF phase drift or because of the oversimplified model.

For an energy of 230 MeV, the much lower bunch time spread allows to recover information across the shape of the PGT spectra and not just through distribution momenta. This can be deployed for spatial emission profile reconstruction with a single detector, a milestone in the field of in vivo proton dose verification. Fig. 3.12 demonstrates the potential for differentially correlating time to depth, and imply a qualitative leap forward of the PGT method with respect to (Golnik et al., 2014), notwithstanding the need of more advanced conversion tools.

First tested at the AGOR research accelerator, the robustness of the PGT method is examined in terms of background, bunch time spread and bunch stability during the experiment at the clinical WPE facility. In this scenario, several factors limiting the accuracy of PGT in its simplest form are encountered. First attempts to understand and quantify these effects are described, and strategies to circumvent them are proposed.

Bunch structure. The bunch time spread is measured indirectly with a thin PMMA target. Besides the prompt γ -rays, there is a high background of scattered protons. In contrast to the detector resolution, the bunch time spread varies depending on the beam energy and has to be monitored, as it influences the precision and outcome of the range reconstruction

3 Prompt gamma-ray timing

algorithms based on PGT data. This motivates the use of dedicated charged particle detectors in upcoming experiments to determine in real-time the bunch width (and phase) directly from protons, e.g. those scattered at the beam exit window.

The increase of the bunch time spread at lower energies is an intrinsic hurdle for the PGT method at the C230 machine (and, in general, at other clinical fixed-energy cyclotrons relying on a degrader to slow down the ions), compared to the AGOR research accelerator. As a consequence, PGT spectra revealing valuable profile information at 230 MeV due to a low bunch time spread may blur completely at 160 or 100 MeV, which are proton energies more frequently used in a therapeutic irradiation. Strategies like the reduction of the momentum slit opening suggest that there is still room for improving the system time resolution, or even for optimising the bunch time structure in future designs of clinical isochronous cyclotrons. However, the change of the slit opening affects the proton bunch shape and decreases the absolute proton transmission, so that higher beam currents have to be requested (or longer treatment times), and the machine commissioning for clinical routine should be repeated completely.

Some research cyclotrons (like AGOR) do not require an energy selection system, as they vary magnetic field and RF to provide the desired beam energy directly at the extraction radius, but are not usual in the clinics. Rather, fixed-energy isochronous cyclotrons are a widespread choice in hospitals. Synchrotrons or synchrocyclotrons are also available (or planned) in many treatment centers (PTCOG, 2014). A priori, the application of the PGT method at these synchronous accelerators, where the micro bunch time spread may be large and the instantaneous current higher, is not straightforward and has to be explored.

Phase drift. The main burden that affects the experimental data presented in this chapter of the thesis is the bunch phase drift with respect to the RF signal, which prevents from further quantitative analysis on centroid shifts. To overcome this instability experimentally, a bunch phase monitor based on phoswich detectors (Wilkinson, 1952) is under development. It identifies and selects by energy the protons scattered at the beam exit window, and measures their crossing time. Then, the actual shift between bunch and RF can be subtracted from the PGT spectra of the γ -ray detector. Additionally, the measurement of the time structure of the beam bunch (non-Gaussian shape) is essential for the modelling, in order to apply a convolution with the proper system response.

Within a clinical PBS session (few minutes), the effect of long-term bunch drift is expected to be negligible when comparing consecutive spots. Rather, one has to correct the mean drift (and variation of bunch time spread) when comparing the measurements of two different treatment fractions (one day separation). Moreover, for the comparison of experimental PGT spectra with modelled ones, one has to discriminate the different energy layers within the fraction, as the proton crossing time of the beam exit window with respect to the RF signal depends on the beam energy (and beam line length). This has to be calibrated accurately

beforehand, or monitored with the aforementioned phoswich detector for each energy layer in real-time.

Normalisation The uncertainty of the normalisation factor to number of protons is also a major hurdle to the presented data, but is a circumstantial limitation of the dead time model and the dependence of detector gain with trigger rate. This provisional problem is expected to be solved with upgraded electronics.

Background. Significant background radiation due to scattered charged particles, neutrons and material activation is observed in the experiments, specially for high proton energies. The PGT method has proven robust for retrieving range shifts in most cases, but the pedestal present in the time histograms is still an important concern. A low signal to noise ratio is observed for the thin target measurements. For thicker targets, the background has a particular (not flat) time structure. Efforts have to be undertaken to either reduce physically the background, or to model and subtract it for minimising the bias on the retrieved range shift.

Detector orientation. For detectors placed downstream, the suppression of charged particles, e.g. by pulse shape discrimination, is advisable to reduce the high relative background generated by scattered protons (as observed in the energy over time spectra). Nevertheless, an upstream positioning provides in principle a better performance, since the γ -ray time of flight to the detector extends the PGT spectrum and thus allows to resolve more details. In addition, the inherent fast neutron background is lower in backward direction (Gunzert-Marx et al., 2004). The drawback is that a high percentage of the measured γ -rays stem from the front face of the target rather than from the Bragg peak position due to a different solid angle coverage. In cases where the accumulated statistics are low, this may be a limitation if a reconstruction of the particle range based on the trailing edge of the PGT spectra is attempted.

Throughput. The measurements described in this chapter of the thesis are made with a pencil beam current between 10 and 100 pA, and a duration of 5 to 7 min. Concretely for a representative case, namely the irradiation of a full PMMA with 160 MeV proton energy, the acquisition lasts 6.5 min and the delivered charge is 23 nC, corresponding to 1.4×10^{11} protons and a beam current of 59 pA. Assuming an isotropic prompt γ -ray yield of 0.16 as in (Golnik et al., 2014), the emission rate of prompt γ -rays with energies higher than 1 MeV is $59 \times 10^6 \gamma/s$. The solid angle covered by the L0 detector at 30 cm distance from the ring center is $d\Omega/\Omega = 1.8 \times 10^{-3}$, the minimum detection efficiency is $\epsilon_D \sim 0.58$ (Berger et al., 2010) and the γ -ray attenuation inside the target is of the order of 45 % (Hubbell and Seltzer, 2004). The resulting overall efficiency $\epsilon_{p\gamma}$ is $\sim 10^{-4}$ (detected γ -rays per proton) and the measured detector trigger rate is 33 kcps. In the particular acquisition system, as the

3 Prompt gamma-ray timing

dynamic dead time is 34 %, the throughput rate is 22 kcps and the total number of registered events is 8.5×10^6 . Thus, the dynamic efficiency is $\epsilon_{p\gamma}^* \sim 7 \times 10^{-5}$ (registered γ -rays per proton). Note that background contributions are dismissed for this calculation.

Besides the bunch time spread, detector throughput is the critical parameter for PGT and has to be addressed for obtaining a reliable range measurement in real-time and in vivo. The electronics required to cope with high count rates up to 1 Mcps without detector overload are under development.

Statistics. What would be the differences in a clinical treatment plan at an IBA C230 machine compared to this experiment? Concerning a realistic 2 Gy PBS irradiation fraction with $\sim 10^{10}$ protons (in total) delivered to a small area of the brain in 873 spots, the instantaneous current at nozzle exit during single spot delivery is about 2 nA, i.e. $\sim 10^{10}$ p/s (Perali et al., 2014). A typical pencil beam spot is thus delivered within a few milliseconds. Note that the overall treatment fraction duration includes the times necessary for magnet sweeping between the spots and for energy switching among the layers, that are dependent on the actual treatment plan. Therefore, the rate estimates are based on proton beams of 2 nA peak current measured at nozzle exit. Considering the L0 detector setup described above without dead time effects ($\epsilon_{p\gamma} \sim 10^{-4}$), the resulting acquisition rate is $\lesssim 1$ Mcps (no overload expected with upgraded electronics), i.e. 500 kcps/nA. The planned number of protons per spot is $\leq 2 \times 10^7$ for $\sim 75\%$ of the spots. In other words, $\lesssim 2000$ γ -rays are measured for each raster point, so that the analysis of the PGT spectrum spot by spot seems not realistic due to insufficient statistics. Rather, one should collect data from several detectors or accumulate γ -rays from neighbour spots in a single spectrum.

Can this qualitative statement be quantified? The statistics necessary for detecting a range shift with 2 mm precision in a PGT spectrum depending on beam current and proton range has been analysed in (Golnik et al., 2014) based on the theoretical error of distribution momenta. Equivalent conclusions could apply here for 100 and 160 MeV proton energies. In the case of low bunch time spread (230 MeV protons), one may want to retrieve a range difference based on the shift of the falling edge (see fig. 3.10), which corresponds to the Bragg peak region, instead of on the mean value or the width of the distribution. What is the minimum number of γ -rays in the PGT spectrum for detecting a range shift in this case? There is no general answer for this question, since the detector orientation, target attenuation and amount of background may play a significant role on the shape of the falling edge.

Alternatively, a statistical analysis is performed based on experimental data of the L0 detector for 230 MeV protons and three particular target configurations: (a) a full homogeneous PMMA phantom, (b) a 5 mm air cavity inside it, and (c) a 20 mm bone insert in place of the cavity.

The original histograms (complete measurements) have around 7×10^6 entries each. Once the region of interest (the fall-off) inside the three PGT spectra is defined, the trailing edge

deviation is calculated by finding the virtual time shift on (a) that minimises the weighted χ^2 test between the (a)-(b) histograms for the cavity or (a)-(c) for the bone insert. These χ^2 tests are performed for four different statistical sample sizes (random subsets of the whole measurement): 10^6 , 10^5 , 10^4 and 10^3 histogram entries (prompt γ -rays plus background). Assuming for simplicity the aforementioned efficiency $\epsilon_{p\gamma} \sim 10^{-4}$, these virtual measurements would correspond approximately to an irradiation with 10^{10} , 10^9 , 10^8 and 10^7 protons, respectively. For each case, 100 subsets of equal sample size are selected randomly in order to determine the average time shift and the standard deviation.

Fig. 3.18 shows the complete statistical study. As expected, the reduction of sample size (number of protons) degrades the shape of the PGT spectra. Statistical noise hampers the identification by eye of the shift of the falling edge the lower the number of protons. On the basis of the χ^2 numerical analysis (bottom right plot of fig. 3.18), 10^8 protons seem to be the threshold for determining a 5 mm shift of the falling edge in a single spot. Below this boundary, namely the region enclosing most of the clinical spots, the statistical deviation is too high, as illustrated by the overlapping of the coloured uncertainty areas. Over this boundary, looking at the error bars, a range shift down to 2 mm can be identified with 10^{10} protons. It is worth remembering that these considerations apply for a particularly low bunch time spread scenario (230 MeV) at the C230, a single detector in upstream orientation and selected target configurations.

How could the collected statistics be increased? One may enlarge the detector volume at the price of developing electronics that sustain a higher throughput. One could also sum up data from several detectors or from neighbour spots to recover statistics, or consider a downstream detector, that maximises the solid angle at the Bragg peak. More sophisticated numerical analysis including the whole histogram for the shift retrieval instead of just a region of interest is also advisable. For example, in the χ^2 tests, useful information like the difference in the γ -ray production at the location of the heterogeneity, which is still visible in the bottom left plot of fig. 3.18, is wasted. There is undoubtedly room for improvement.

An opposite approach, which would affect clinical workflow and planning, is to deliver a benchmark spot, namely the raster point of the plan with the highest number of protons, which corresponds usually to the distal region. The rationale is to detect with confidence (along the selected incidence direction) potential range shifts due to anatomy changes between treatment fractions. The number of protons of the richest spot depends on each particular tumour location and treatment planning software, but it is not uncommon to have at least one spot with $\geq 10^8$ protons, see (Smeets et al., 2012, fig. 19). One could deliver this benchmark spot immediately at the beginning of the treatment and check the acquired PGT spectrum. If no deviations are observed, one would consecutively repeat this step for all spots of the distal layer to cover other irradiation areas. If the results comply with the expectations, one could then deliver all remaining spots of the plan. Hence, just the spot order delivery but not the dosimetry is affected.

Another option would be to double the detector size and halve the instantaneous clinical

3 Prompt gamma-ray timing

current (for all spots) to keep the count rate at an acceptable level, but multiply the detection efficiency $\epsilon_{p\gamma}$ by a factor of two. For the particular treatment plan considered above (10^{10} protons at 10^{10} p/s), the actual irradiation time of the small area of the brain lasts about one second. This irradiation time is relatively small compared to the global delivery time (~ 15 s), with a significant dead time due to magnet sweeping and change of energy layers. Hence, halving the beam current would not increase significantly the treatment duration in the WPE treatment facility. Still, this option raises some concerns about the use of beam currents not tested in the commissioning phase of the machine and routine quality assurance.

A further strategy, which combines the two last, is to deliver at treatment beginning the spot with the highest number of protons of the plan, e.g. 10^8 protons, with a very low beam current (one proton per bunch, around 1 s irradiation at 2 pA), and measure the passage of every proton with a beam hodoscope. The added value is that the effect of bunch time spread is suppressed for any beam energy, as each detected prompt γ -ray can be correlated to the primary proton. The collected statistics can also be maximised, since the lower beam current allows the use of larger detectors. Obviously, this is the most precise method from the physical point of view. From the clinical side, it implies only a slight change in the treatment planning, as it is anyway usual to deliver three so called *tuning* spots at the beginning of the plan with a short duration; if no failure is detected, the rest of the plan is delivered. From the technical point of view, this strategy may not be accepted, as it requires cyclotron beam currents far below the ones the machine supplies in usual conditions, so that extraordinary fine-tuning of the accelerator is required by an experienced operator.

Quantification. For the quantitative retrieval of the range, several strategies have been proposed and illustrated. Forward calculation allows to directly compare distribution momenta of experimental PGT spectra with expectation values according to a given model, cf. figs. 3.9 (right) and 3.12 (left). Backward calculation has the advantage that no spatial emission profile is assumed. It provides a first impression of the actual depth-dose profile for 230 MeV protons and allows a comparison in the spatial instead of the time dimension, cf. fig. 3.11 (right) and 3.12 (right). However, the time spread limits this approach, and a deconvolution with the system time response is a non-trivial and ill-posed transformation. The parametric reconstruction of the proton range, cf. figs. 3.15 and 3.16, is a promising way for simple target configurations. It could be extended to multiple parameters, for example f and h for the single cavity experiment. It exploits the full shape of the PGT spectrum and not only the mean value or width. In fact, the integral or curve height plays also a major role and adds further information (transversal dimension) about the distance from detector to emission region. It may be interesting to apply this procedure in a low-statistic scenario like fig. 3.18 (bottom left). The integral of the spectrum is an indicator (further ingredient) of the proton range, provided that the electronics provide an accurate normalisation and dead time correction factor. This approach is more robust than looking just at the shift of the falling edge.

In any of the three variants, a good knowledge of the tissue composition (stopping power)

is required. For the forward calculation and parametric reconstruction, an underlying model is needed to compute the expected spatial emission profile. To provide a realistic one, extensive simulation and modelling studies (out of scope) are mandatory. More realistic PGT modelling should consider effects like energy-resolved emission profiles, detector sensitivity for complex geometries, background subtraction and non-Gaussian micro bunch time structure.

Stopping power PGT spectra at 230 MeV (low bunch time spread scenario) have an essential difference with respect to the profiles measured with a knife-edge slit camera. In the latter case, the horizontal axis corresponds to the spatial position; in the first case, to a time point. As the time scale is not linearly correlated with the spatial scale, the PGT spectra do not provide a proportional image of the γ -ray emission but rather a stretched one. In the analogy of optics, a slit camera would be an orthoscopic lens, whereas the PGT camera would be a partially distorting lens. To correct the introduced aberration and obtain a depth profile, an inverse transformation is needed as intermediate step, cf. fig. 3.11. However, this calibration depends on the accurate knowledge of the stopping power of the traversed tissue (Golnik et al., 2014). One may then argue that no method for detecting range uncertainties should depend on their most common source: the variation of the tissue composition (stopping power) between clinical fractions. The absence of a daily patient imaging prevents a recalibration of the time to space relationship for each fraction. Does this mean that the PGT approach is useless?

Let us put it the other way round and calculate a PGT spectrum according to the treatment plan expectations (and uncertainties). If, unluckily, the assumed anatomy is inaccurate, the reference PGT profile will be biased. As a consequence, an overshoot of e.g. 5 mm may occur. The measured PGT profile will change with respect to the expected one due to its dependence on the spatial emission profile, but also on the stopping power itself (simultaneous dependency). Due to the unawareness on the exact anatomy and the bias introduced on the reference spectrum, one may not be able to quantify with utmost accuracy the actual range deviation. But the differences (in shape or momenta) between the reference and the measured spectra are expected to be blamed (with enough confidence) on e.g. a shift between 3 mm up to 7 mm. In other words, the PGT method could serve as real-time safety assurance for detecting severe deviations rather than accurate range measurements. This strategy is also applicable for lower proton energies (larger bunch time spread).

In any case, even for an ideal prompt γ -ray camera that reproduces the spatial emission profile faithfully (without distortions) and with perfect counting statistics, the amplitude of the actual range shift is biased by the treatment plan expectations. The reason is that the correlation of prompt γ -ray yield to particle range depends on the assumed tissue composition. Still, measurements that reveal significant differences with respect to biased reference spectra are reliable indicators that something is not going on as planned.

Last, the statement about the dependence of PGI on the stopping power is just qualitative.

3 Prompt gamma-ray timing

It might be that the uncertainties in tissue composition are small or have only little effect on the reconstructed range, so that it would not be mandatory to look for alternative methods or increase the precision of the stopping power characterisation. To answer this question quantitatively, sensitivity studies about the range measurement error due to stopping power uncertainties are required. The expense to be paid (or effort to be taken) for the modelling algorithms has to be assessed.

Outlook towards the clinics. At this stage, the experimental results do not allow a comparison of the PGT method with other more developed techniques as e.g. the knife-edge slit camera, which is able to image millimetre shifts at clinical current intensities and anthropomorphic phantoms (Perali et al., 2014; Priegnitz et al., 2015). The PGT method is far beneath in the ladder of clinical translation, and one can think of many limiting scenarios in which its applicability is questionable or yet unproven. However, some trends and qualitative aspects are already observed in this work, which encourage the hope of a quantitative retrieval of the range based on the PGT method. Whereas a spatial precision comparable to other methods cannot be claimed, there are reasons to believe that the much lower expense and footprint of this technology may boost its applicability and spread in the clinics, and thus deserves further investigations.

Thanks to its real-time range assessment capability, PGT has the potential to be translated into clinical practice as a fast handle to stop a running treatment with significant deviations during the clinical fraction. The workflow for detecting severe range shifts could look like follows:

- A realistic spatial emission profile is simulated according to the treatment plan.
- The expected timing profile is calculated based on the detector model and patient data.
- PGT spectra are measured during the clinical fraction and corrected for bunch drifts (with respect to the previous treatment session) by a phase monitor.
- The center of gravity of the modelled and measured PGT spectra is compared in real-time.
- If the difference exceeds a clinically critical value, the treatment can be interrupted and the source of error analysed or corrected in upcoming treatment fractions.

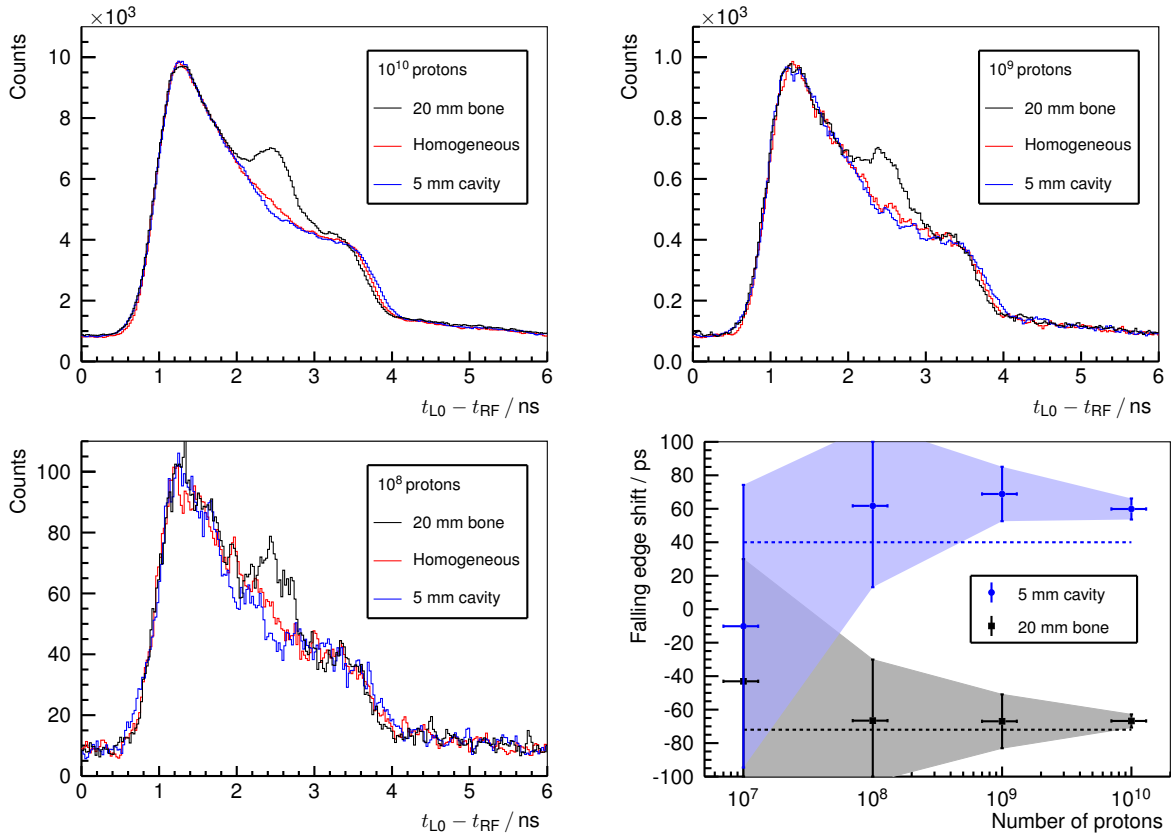


Figure 3.18: Top row and bottom left plot: PGT spectra of the L0 detector at $\alpha = 140^\circ$, $d = 30.0$ cm, for 230 MeV protons. The homogeneous case (red curve) corresponds to a full PMMA target (400 mm). A heterogeneous slice is placed inside the full PMMA target at $f = 169$ mm ; $h = 5$ mm (air cavity - blue curve) or $f = 169$ mm ; $h = 20$ mm (bone insert - black curve), where f ; h are the (front face position; thickness) as described in fig. 3.3 (top). Energy threshold is 1 MeV. Spectra of top left figure are normalised to their respective maximum and shifted in time to match their leading edges at 50% of the rise. The obtained shift and scale factors are applied then for the top right and bottom left plots. A smoothing filter is applied on the histogram bin contents for visual enhancement (not used later in numerical analysis). The legend header contains the number of protons associated to each spectrum (assuming $\epsilon_{p\gamma} \sim 10^{-4}$). The graph with 10^7 protons is left out for compactness. Bottom right: shift of the falling edge (retrieved with the weighted χ^2 test) with respect to the homogeneous case depending on the number of protons. Experimental points are averaged over 100 samples of equal size (see text). The vertical error bars (and enclosing solid coloured area) are the standard deviation among the samples. The horizontal error bars are set to 30% of the number of protons. The dashed lines depict the expected shift of the trailing edge according to the simBox model: (40 ± 1) ps for a 5 mm overshoot due to the cavity and (-72 ± 1) ps for a ~ 8 mm undershoot due to the bone insert.

3.7 Conclusions

In vivo range verification in real-time is a must for improving the outcome of ion beam therapy. The prompt γ -rays produced in nuclear interactions are reliable signatures for reconstructing the depth-dose profile, provided that the tissue composition is well known. The prompt γ -ray timing method aims at assessing the range based on a simple detector setup without mechanical collimation.

This section of the thesis describes the first test of the PGT method at a clinical proton accelerator with different phantoms and detectors. The bunch time spread is characterised for several energies and the robustness of the method concerning background and bunch stability is investigated. For 10^{10} protons (230 MeV energy) and a single detector, a particle range difference of two millimetres is identified in predefined heterogeneous targets based on the distinctness of the timing distributions. For 10^8 irradiated protons, a five millimetre range shift is retrievable by means of numerical analysis. The experimental results also prove that PGT spectra comprise very detailed information on γ -ray emission along the track when the bunch time spread is low.

The PGT method appears to be feasible in a clinical scenario with a pencil beam if following intermediate steps concerning hardware, software and procedure are addressed to counteract the encountered limitations:

- Addition of a bunch phase monitor which measures the long-term drift with respect to the accelerator RF, as well as the bunch timewise shape for each treatment fraction. The monitor can also correlate the crossing time of the protons through the beam exit window with respect to the RF signal for each energy layer.
- A much higher detector and data acquisition throughput to cope with the γ -ray rate expected in an actual clinical treatment fraction.
- An accurate time spectrum and background modelling, and numerical analysis or even iterative reconstruction algorithms for obtaining a quantitative measurement of the particle range.

Experiments with improved detectors and electronics, proton bunch monitor, realistic currents, PBS and the use of anthropomorphic phantoms are the next steps towards clinical translation.

In conclusion, the overall experimental results underline the potential of the prompt γ -ray timing method for range assessment in a clinical pencil beam and reassure this novel approach as a promising alternative in the field of in vivo dosimetry.

4 Discussion

4.1 Detector load, event throughput and spot duration

Prompt γ -rays are adequate signatures for range verification: they are emitted immediately during beam delivery, exit the patient with moderate attenuation and their distribution correlates to the dose released by the protons through ionisation processes. There are enough γ -rays produced during beam delivery to obtain a statistically significant measurement of their distribution. Where lies then the problem?

Despite having a huge amount of γ -rays, there is no realistic way to detect them all. First, one would need 4π and very thick detectors covering the whole treatment room. But the main concern is that, in a clinical scenario like the C230 accelerator (Hueso González et al., 2015b), prompt γ -rays are produced in a very high rate $\dot{N}_\gamma \sim 10^9 \text{ s}^{-1}$ (too close to each other). Conventional detectors located close to the patient and the associated electronics cannot cope with such high fluxes. This forces the use of smaller detectors or the increase of the distance to the beam axis.

In principle, this workaround may appear satisfying in spite of reducing the system sensitivity. However, if one considers realistic treatment plans in PBS, where the range has to be verified spot by spot, one encounters that the number of protons per spot is rather small: $\lesssim 10^8$. The beam current is kept constant in most cases, so that \dot{N}_γ remains the same; the number of protons delivered per spot is proportional to the spot duration T_{spot} . If one is forced to put the detector too far away, the covered solid angle may be too low and one would not collect enough prompt γ -rays to draw a statistically significant conclusion on the particle range. In other words, how close has the detector to be located (without interfering with the patient) to gather enough γ -rays per spot? Can the crystal sustain that load? Is it possible to obtain an estimate of the range spot-wise or at least for the strongest (longest) spots, see (Smeets et al., 2012, fig. 19)? Is it necessary to develop dedicated high-rate electronics?

Three different values should be clearly distinguished: the detector load \dot{N}_{load} (γ -rays interacting in the detector per unit time), the trigger rate \dot{N}_{trig} (those γ -rays above a specified signal threshold) and the event throughput \dot{N}_{through} (those trigger events processed by the data acquisition). In any case, $\dot{N}_{\text{load}} \geq \dot{N}_{\text{trig}} \geq \dot{N}_{\text{through}}$. The limit on \dot{N}_{load} is given by the tolerable pile-up for the particular crystal (and PMT). \dot{N}_{trig} is conditioned by the energy threshold set in the hardware. \dot{N}_{through} has an upper limit that depends on the electronics dead time. For high trigger rates, $\dot{N}_{\text{through}} \ll \dot{N}_{\text{trig}}$.

4 Discussion

Detector load (\dot{N}_{load}), event throughput (\dot{N}_{through}) and spot duration (T_{spot}) are crucial parameters in the clinical field. Note that a key constraint for T_{spot} is the instantaneous beam current (peak current). It can be up to one order of magnitude higher than the average current throughout the fraction due to dead time between spots (magnet sweeping, synchrotron filling, energy change). The duty cycle depends on the type of accelerator. In clinical irradiations, a high beam current is preferred in order to minimise the treatment fraction duration (and the probability of patient misalignment via movement).

In many range verification systems, as Compton cameras, this aspect has not yet been discussed in depth in associated publications. However, it is of paramount importance for the electronics design when trying to apply research prototypes to clinical systems (Smeets, 2012). It should be addressed already at early research stages, to avoid developing very complex and expensive systems that fail at the last point of the translation chain. In this section, some approximate estimates of the detector trigger rate and events recorded per spot are provided, particularised for the beam parameters at the C230 cyclotron. It is the only clinical accelerator investigated in this thesis, and the instantaneous beam current deployed in clinical routine is 2 nA at nozzle exit, cf. table 4.1. Several benchmark detectors at 25 cm distance are selected, cf. table 4.2.

The goal is just to calculate a rough (reasonable) order of magnitude for a realistic scenario, keeping in mind that the real value \dot{N}_{trig} may be wrong by a factor of two. Accurate estimates should rely on MC simulations including the γ -ray energy spectrum and detector response. At the end of the story, the true limit is set by the maximum event throughput \dot{N}_{through} (at least in the case of PGT) rather than by the γ -ray flux \dot{N}_{γ} or \dot{N}_{trig} . Provided that \dot{N}_{load} is acceptable, the decisive point is the factor $N = \dot{N}_{\text{through}} \times T_{\text{spot}}$, which does not depend on the mentioned inaccuracies. It defines the number N of collected events per spot and thus the capability of statistically significant range verification. As mentioned in section 3.6, one may think of strategies to reduce the instantaneous beam current so that T_{spot} is longer. The detector can be put closer (so that \dot{N}_{through} is kept equal to the normal case) and the gathered statistics are increased.

It is worth noting that the physical limit $1/(10\tau)$ calculated in table 4.2 refers to the detector load. Whereas some scintillation crystals are fast enough to sustain $\dot{N}_{\text{load}} = 3 \text{ Mcps}$, it is not conventional to read out, process and store data at this speed in order to obtain real-time results ($\dot{N}_{\text{through}} \ll \dot{N}_{\text{load}}$). Furthermore, the dependency of PMT gain on factors such as temperature and detector load is an important concern (Stein et al., 2015). In the case of PGT, the aim is to use commercial electronics that sustain up to $\dot{N}_{\text{through}} \sim 1 \text{ Mcps}$ (1 μs dead time) and incorporate gain stabilisation. $N \sim 8 \times 10^3$ events are expected to be acquired per spot. Fast crystals have to be selected to cope with up to $\dot{N}_{\text{through}} \sim 5 \text{ Mcps}$, as the trigger rate above 1 MeV does not include the significant low-energy background and the prominent 511 keV γ -ray line from material activation.

In the case of the Cc, the problem is one dimension more complicated, as coincidences instead of single events are needed. For example, the CZT1-BGO1 setup (Kormoll et al.,

2013) has a low coincident efficiency. The thin CZT1, which is a good choice to reduce multiple interaction processes within the scatterer, leads to a strong asymmetry in the detector rate with respect to the much thicker absorber (BGO1), see table 4.2. Moreover, not all photons N interacting with the scatterer reach the absorber (restricted solid angle), and those that reach them are not fully absorbed in most cases. As a consequence, the number of valid coincidences M for the Cc may be one or two orders of magnitude smaller than the single events at the scatterer, i.e. $M = k_\epsilon N$. It is assumed, based on (Rohling, 2015, p. 66), that roughly $k_\epsilon = 2\%$ of the latter events generate valid coincidences. This setup would lead to a coincidence rate of 1000 cps and thus to just $M_{\text{CZT1,BGO1}} = 8$ valid events for the distal spot. Even increasing the number or size of detectors, it seems not realistic to obtain a range verification spot by spot with the current setup and realistic clinical currents (at the C230 accelerator). The observation that detector load, throughput and spot duration are a major concern in the PGI Cc approach is in accordance to (Polf et al., 2015), where beam currents far below 2 nA are used. To circumvent the pile-up problem with usual currents, one might be tempted to use thin detectors (low efficiency $\epsilon_D \ll 1$) in both stages of the camera. But this does not solve the problem of low coincident efficiency, which is proportional (at first order approximation) to ϵ_D^2 , and of the insufficient statistics per spot.

The BbCc setup, comprising BGO4 as scatterer and BGO1 as absorber, tries to break with simple means the aforementioned trigger rate asymmetry between stages of the CZT1-BGO1 setup. By using a very thick and dense scatterer, the single detector rate is comparable, the incoherent scattering efficiency is higher – proportional to the material areal density, cf. section 2.1 –, at the price of higher probability of multiple interaction processes. Overall, the efficiency is maximised with respect to the CZT1-BGO1 setup. Even though the energy resolution is worse or there is a higher probability of random coincidences, the gathered statistics are one order of magnitude higher for the BbCc setup, cf. table 4.2. Assuming for simplicity that the same factor $k_\epsilon = 2\%$ applies for both cameras, in accordance with table 2.5, the coincidence rate yields 16 kcps and $M_{\text{BbCc}} = 130$ Compton cones per distal spot are collected. It may be of greater significance to have a large number of events $M_{\text{BbCc}} = 130$ with moderate information than only $M_{\text{CZT1,BGO1}} = 8$ very accurate Compton cones. In any case, Compton events may have a high information density about the γ -ray directionality, but the low amount of these golden events with either setup and the expense (concerning electronics and detectors) question the applicability of Compton cameras for prompt γ -ray imaging in the medical field.

The PGT approach goes deeper inside this philosophy: a single event contains relatively low information about the γ -ray origin (smeared out), but no coincidences are needed, so that the valid events $M = N$, i.e. $k_\epsilon = 100\%$. Statistics are thus maximised and significant conclusions can be drawn based on distribution momenta (Golnik et al., 2014). Taking into account the constraints in spot length T_{spot} and clinical current (table 4.1), it seems better to obtain many events with low precision than a few of them with very high accuracy. Idem for passively collimated cameras (no coincidence condition), where the load \dot{N}_{load} and throughput \dot{N}_{through} rather than the collimator itself are the factors limiting the collected statistics.

Table 4.1: Beam parameters, radiation production rates and detector setup in a realistic treatment scenario.

Parameter	Value
Current at nozzle exit during spot	2 nA
Proton flux at nozzle exit	$1.25 \times 10^{10} \text{ s}^{-1}$
Protons @ distal spot	10^8
Distal spot duration T_{spot}	8 ms
Prompt γ -ray yield	~ 0.16
γ -ray emission rate \dot{N}_{γ}	$2.0 \times 10^9 \text{ s}^{-1}$
γ -rays @ distal spot	1.6×10^7
Attenuation in phantom	$\sim 45 \%$
Detector distance to beam axis	25 cm

Note: estimates are based on (Hueso González et al., 2015b). Distal spot refers to the raster point in the treatment plan corresponding to the irradiation of the distal edge. It is not uncommon for the strongest spot to contain close to 10^8 protons (Smeets et al., 2012, fig. 19). The isotropic prompt γ -ray yield refers to photons above 1 MeV and is extracted from (Golnik et al., 2014) for 160 MeV protons on a PMMA target.

Table 4.2: Rough estimates of single trigger rate for different PGI benchmark detectors according to a realistic clinical scenario.

Detector	Size	$d\Omega/\Omega$	ρ	ϵ_{D}	$\epsilon_{\text{P}\gamma}$	\dot{N}_{trig}	Events	$1/(10\tau)$
CZT1	$2.0 \times 2.0 \times 0.5 \text{ cm}^3$	5.1×10^{-4}	5.78 g/cm^3	9 %	4.3×10^{-6}	53 kcps	400	330 kcps
BGO4	$3.5 \times 3.8 \times 3.0 \text{ cm}^3$	1.3×10^{-3}	7.13 g/cm^3	56 %	6.6×10^{-5}	0.8 Mcps	7000	330 kcps
BGO1	$5.3 \times 5.3 \times 2.0 \text{ cm}^3$	2.8×10^{-3}	7.13 g/cm^3	42 %	1.0×10^{-4}	1.3 Mcps	10000	330 kcps
L0	$\varnothing 2'' \times 2''$	2.6×10^{-3}	5.06 g/cm^3	58 %	1.3×10^{-4}	1.6 Mcps	13000	2.9 Mcps
LYSO	$0.4 \times 10.0 \times 3.2 \text{ cm}^3$	5.1×10^{-4}	7.10 g/cm^3	57 %	2.5×10^{-4}	0.3 Mcps	2500	2.4 Mcps

Note: the particular beam parameters and detector setup are described in table 4.1. The covered solid angle $d\Omega/\Omega$ is calculated with eq. 3.10, taking an average effective radius in the case of rectangular crystals. ρ is the mass density of the crystal. The detection efficiency ϵ_{D} per incident photon takes into account the X-ray attenuation coefficient at an energy of 5 MeV (Hubbell and Seltzer, 2004) and the crystal depth (assuming straight photon incidence). $\epsilon_{\text{P}\gamma}$ is the number of prompt γ -rays interacting with the detector per incident proton, which depends on the prompt γ -ray yield, covered solid angle, attenuation factor and detection efficiency. \dot{N}_{trig} refers to the single detector trigger rate during beam delivery (instantaneous current, not averaged over the treatment fraction). Events alludes to the number of prompt γ -rays measured by the detector for a typical distal spot (10^8 protons), dismissing dead time effects. τ is the crystal decay time (or mean drift time for CZT1) and the quotient $1/(10\tau)$ is an estimate of the maximum detector load with manageable pile-up ($\sim 25\%$). CZT1 is the CdZnTe cross strip detector described in (Hueso González et al., 2014); the fact that the active volume is smaller if the trigger is on the anode signal is dismissed. BGO4 and BGO1 are the block detectors introduced in subsection 2.4.4, whereas L0 is the LaBr₃ scintillation detector described in table 3.1. LYSO stands for lutetium-yttrium oxyorthosilicate ($\text{Lu}_{2(1-x)}\text{Y}_{2x}\text{SiO}_5:\text{Ce}$) and refers to a single crystal slab of the IBA slit camera (Perali et al., 2014).

4.2 Comparison of PGI systems

The capabilities and requirements of the Cc and PGT systems for PGI are summarised in table 4.3. These are compared to the IBA slit camera (as reference).

Table 4.3: Capabilities and technical requirements of PGI systems for range verification in proton therapy.

Capabilities	Cc	PGT	Slit camera
Applicability in proton PBS	?	Yes	Yes
3D reconstruction	Yes	?	?
Potentially quantitative	Yes	Yes	Yes
Requirements			
Energy spectroscopy	Yes	No	No
Spatial resolution	Yes	No	Yes
Time resolution	Yes	Yes	No
Electronic channels	~ 1000	~ 5	~ 50
Data processing complexity	Huge	Little	Medium
Reconstruction algorithm	Complex	Medium	Simple

Note: the Cc, the PGT method and the IBA slit camera are compared in terms of capabilities, detector requirements, electronics and data processing.

In principle, a Cc is more powerful than the PGT method, as it can provide 2D or even 3D images instead of just 1D. Also, PGT events are smeared out strongly by the bunch time spread at clinically relevant energies. In other words, a (true) Compton cone contains more information than a single timing event. Furthermore, for the Cc, the reconstruction of the prompt γ -ray emission density is independent on the assumed stopping power, whereas the PGT approach depends on a priori assumptions of the tissue composition. Still, even for the Cc, an ideal imaging of the prompt γ -ray distribution is not enough: the correlation with the dose deposition and particle range is needed, a transformation that depends also on the assumed tissue.

There are two main factors that hint at the likelier applicability of the PGT method in a clinical scenario over the Cc approach:

- The number of electronic channels, detector price and complexity is much higher for the Cc.
- The efficiency factor $k_{\epsilon}(\text{Cc}) = 2\%$ is almost two orders of magnitude smaller than $k_{\epsilon}(\text{PGT}) = 100\%$. Even if the information per event is larger in the case of the Cc, the low amount of statistics per spot is a critical point.

In some scientific discussions, it is argued that a Cc is able to provide accurate 3D images and detect potential range deviations despite low statistics thanks to the MLEM reconstruction algorithm, which accumulates the data from all spots. However, this reasoning is misleading if one attempts to detect local range shifts (small cavity close to the nominal particle

4 Discussion

range and affecting just one beam spot) instead of global ones (patient misalignment or large cavity at the beginning of the beam path). For the first type, the information is given by the missing γ -rays inside the cavity and the excess beyond it (compared to the homogeneous case) for the spot under consideration. If the event density (valid coincidences detected per differential volume) is low and the cavity is small, too few γ -rays will stem from the overshoot region and the camera will not be sensitive to this deviation. For the second type, the shift can be detected because all γ -rays from all spots are coming from a different direction (angle) with respect to the original case. However, if only the identification of global shifts based on the center of gravity of the images is achievable with a Cc, it loses one of its main attractions, and other methods like PGT with less expense and the same outcome are advisable.

Anyway, one may think about the combination of both methods to exploit their respective strengths. For example, a Cc camera incorporating PGT information would be the analogous of a PET camera with time of flight information. On the other hand, for standalone PGT, the combination of several timing detectors at different angles could balance or cancel the dependence on the stopping power (Pausch et al., 2015) and boost the performance of the method. In any case, for the treatment of tumours in the abdominal or thoracic region, it is important to obtain a measurement spot by spot, to detect (or compensate for) time-wise range deviations due to (periodic) organ motion. These are expected to be large in the case of lung cancer due to the strong tissue heterogeneity.

As discussed in section 3.6, the expectation is to detect with a single PGT detector 5 mm range deviation for the distal spots, those with the largest number of protons. In principle, this would allow just a partial reduction of the safety margins applied currently in treatment plans, cf. fig. 1.3. Increase of number of detectors or setup optimisation aside, it might be claimed that the effort is not worth enough for obtaining such moderate precision (or margin shrinkage).

At the current stage of the research, to some extent, it is adventurous to say that any PGI camera is able to provide trustworthy estimators of the dose released in tissue by a proton beam in a clinically realistic scenario. The safety margins have not been modified after years of research. The hope for the future implementation of a range verification PGI device is that the sensitivity on patient anatomy is not critical. Nevertheless, even taking into account all uncertainties, such an apparatus would still serve as real-time safety assurance system. If there is, unluckily, a significant beam overshoot or undershoot, the deviation with respect to the treatment plan can be detected and the treatment interrupted, or a correction applied in upcoming therapy sessions. Safety margins may be also reduced after further investigations and in accordance with experienced clinicians.

4.3 Summary

Background. Accelerated protons are excellent candidates for treating several types of tumours. Such charged particles stop at a defined depth, where their ionisation density is maximum. As the dose deposit beyond this distal edge is very low, proton therapy minimises the damage to normal tissue compared to photon therapy. Nonetheless, inherent range uncertainties cast doubts on the irradiation of tumours close to organs at risk and lead to the application of conservative safety margins. This constrains significantly the potential benefits of proton over photon therapy and limits its ultimate aspirations.

Motivation. Prompt γ -rays, a by-product of the irradiation that is correlated to the dose deposition, are reliable signatures for the detection of range deviations and even for three-dimensional in vivo dosimetry. In this work, two methods for Prompt Gamma-ray Imaging (PGI) are investigated: the Compton camera (Cc) and the Prompt Gamma-ray Timing (PGT). Their applicability in a clinical scenario is discussed and compared. The first method aspires to reconstruct the prompt γ -ray emission density map based on an iterative imaging algorithm and multiple position sensitive γ -ray detectors. These are arranged in scatterer and absorber plane. The second method has been recently proposed as an alternative to collimated PGI systems and relies on timing spectroscopy with a single monolithic detector. The detection times of prompt γ -rays encode essential information about the depth-dose profile as a consequence of the measurable transit time of ions through matter.

Materials and methods. At Helmholtz-Zentrum Dresden-Rossendorf (HZDR) and Onco-Ray, detector components are characterised in realistic radiation environments as a step towards a clinical Cc. Conventional block detectors deployed in commercial Positron Emission Tomography (PET) scanners, made of Cerium-doped lutetium oxyorthosilicate - $\text{Lu}_2\text{SiO}_5:\text{Ce}$ (LSO) or Bismuth Germanium Oxide - $\text{Bi}_4\text{Ge}_3\text{O}_{12}$ (BGO) scintillators, are suitable candidates for the absorber of a Cc due to their high density and absorption efficiency with respect to the prompt γ -ray energy range (several MeV). LSO and BGO block detectors are compared experimentally in clinically relevant radiation fields in terms of energy, spatial and time resolution. On a different note, two BGO block detectors (from PET scanners), arranged as the BGO block Compton camera (BbCc), are deployed for simple imaging tests with high energy prompt γ -rays produced in homogeneous Plexiglas targets by a proton pencil beam. The rationale is to maximise the detection efficiency in the scatterer plane despite a moderate energy resolution. Target shifts, increase of the target thickness and beam energy variation experiments are conducted. Concerning the PGT concept, in a collaboration among Onco-Ray, HZDR and IBA, the first test at a clinical proton accelerator (Westdeutsches Protonentherapiezentrum Essen) with several detectors and heterogeneous phantoms is performed. The sensitivity of the method to range shifts is investigated, the robustness against background and stability of the beam bunch time profile is explored, and the bunch time spread is characterised for different proton energies.

Results. With respect to the material choice for the absorber of the Cc, the BGO scintillator closes the gap with respect to the brighter LSO. The reason behind is the high energies of prompt γ -rays compared to the PET scenario, which increase significantly the energy, spatial and time resolution of BGO. Regarding the BbCc, shifts of a point-like radioactive source are correctly detected, line sources are reconstructed, and one centimetre proton range deviations are identified based on the evident changes of the back projection images. Concerning the PGT experiments, for clinically relevant doses, range differences of five millimetres in defined heterogeneous targets are identified by numerical comparison of the spectrum shape. For higher statistics, range shifts down to two millimetres are detectable. Experimental data are well reproduced by analytical modelling.

Conclusions. The Cc and the PGT are ambitious approaches for range verification in proton therapy based on PGI. Intensive detector characterisation and tests in clinical facilities are mandatory for developing robust prototypes, since the energy range of prompt γ -rays spans over the MeV region, not used traditionally in medical applications. Regarding the material choice for the Cc: notwithstanding the overall superiority of LSO, BGO catches up in the field of PGI. It can be considered as a competitive alternative to LSO for the absorber plane due to its lower price, higher photoabsorption efficiency, and the lack of intrinsic radioactivity. The results concerning the BbCc, obtained with relatively simple means, highlight the potential application of Compton cameras for high energy prompt γ -ray imaging. Nevertheless, technical constraints like the low statistics collected per pencil beam spot (if clinical currents are used) question their applicability as a real-time and in vivo range verification method in proton therapy. The PGT is an alternative approach, which may have faster translation into clinical practice due to its lower price and higher efficiency. A proton bunch monitor, higher detector throughput and quantitative range retrieval are the upcoming steps towards a clinically applicable prototype, that may detect significant range deviations for the strongest beam spots. The experimental results emphasise the prospects of this straightforward verification method at a clinical pencil beam and settle this novel approach as a promising alternative in the field of in vivo dosimetry.

4.4 Zusammenfassung

Hintergrund. Beschleunigte Protonen sind ausgezeichnete Kandidaten für die Behandlung von diversen Tumorarten. Diese geladenen Teilchen stoppen in einer bestimmten Tiefe, bei der die Ionisierungsdichte maximal ist. Da die deponierte Dosis hinter der distalen Kante sehr klein ist, minimiert die Protonentherapie den Schaden an normalem Gewebe verglichen mit der Photonentherapie. Inhärente Reichweitenunsicherheiten stellen jedoch die Bestrahlung von Tumoren in der Nähe von Risikoorganen in Frage und führen zur Anwendung von konservativen Sicherheitssäumen. Dadurch werden die potentiellen Vorteile der Protonen gegenüber der Photonentherapie sowie ihre letzten Ziele eingeschränkt.

Fragestellung. Prompte γ -Strahlung, ein Nebenprodukt der Bestrahlung, welche mit der Dosisdeposition korreliert, ist eine zuverlässige Signatur um Reichweitenunterschiede zu detektieren und könnte sogar für eine dreidimensionale in vivo Dosimetrie genutzt werden. In dieser Arbeit werden zwei Methoden für Prompt Gamma-ray Imaging (PGI) erforscht: die Compton-Kamera (CK) und das Prompt Gamma-ray Timing (PGT)-Konzept. Des Weiteren soll deren Anwendbarkeit im klinischen Szenario diskutiert und verglichen werden. Die erste Methode strebt nach der Rekonstruktion der Emissionsdichtenverteilung der prompten γ -Strahlung und basiert auf einem iterativen Bildgebungsalgorithmus sowie auf mehreren positionsempfindlichen Detektoren. Diese werden in eine Streuer- und Absorberebene eingeteilt. Die zweite Methode ist vor Kurzem als eine Alternative zu kollimierten PGI Systemen vorgeschlagen worden, und beruht auf dem Prinzip der Zeitspektroskopie mit einem einzelnen monolithischen Detektor. Die Detektionszeiten der prompten γ -Strahlen beinhalten entscheidende Informationen über das Tiefendosisprofil aufgrund der messbaren Durchgangszeit von Ionen durch Materie.

Material und Methode. Am Helmholtz-Zentrum Dresden-Rossendorf (HZDR) und OncoRay werden Detektorkomponenten in realistischen Strahlungsumgebungen als ein Schritt zur klinischen CK charakterisiert. Konventionelle Blockdetektoren, welche in kommerziellen Positronen-Emissions-Tomographie (PET)-Scannern zum Einsatz kommen und auf Cer dotiertem Lutetiumoxyorthosilikat - $\text{Lu}_2\text{SiO}_5:\text{Ce}$ (LSO) oder Bismutgermanat - $\text{Bi}_4\text{Ge}_3\text{O}_{12}$ (BGO) Szintillatoren basieren, sind geeignete Kandidaten für den Absorber einer CK wegen der hohen Dichte und Absorptionseffizienz im Energiebereich von prompten γ -Strahlen (mehrere MeV). LSO- und BGO-Blockdetektoren werden in klinisch relevanten Strahlungsfeldern in Bezug auf Energie-, Orts- und Zeitauflösung verglichen. Weiterhin werden zwei BGO-Blockdetektoren (von PET-Scannern), angeordnet als BGO Block Compton-Kamera (BBCK), benutzt, um die Bildgebung von hochenergetischen prompten γ -Strahlen zu untersuchen, die in homogenen Plexiglas-Targets durch einen Protonen-Bleistiftstrahl emittiert werden. Die Motivation hierfür ist, die Detektionseffizienz der Streuerebene zu maximieren, wobei jedoch die Energieauflösung vernachlässigt wird. Targetverschiebungen, sowie Änderungen der Targetdicke und der Teilchenenergie werden untersucht. In einer Kollaboration zwischen OncoRay, HZDR and IBA, wird der erste Test des PGT-Konzepts an einem klini-

schen Protonenbeschleuniger (Westdeutsches Protonentherapiezentrum Essen) mit mehreren Detektoren und heterogenen Phantomen durchgeführt. Die Sensitivität der Methode hinsichtlich Reichweitenveränderungen wird erforscht. Des Weiteren wird der Einfluss von Untergrund und Stabilität des Zeitprofils des Strahlenbündels untersucht, sowie die Zeitverschmierung des Bündels für verschiedene Protonenenergien charakterisiert.

Ergebnisse. Für die Materialauswahl für den Absorber der CK ergibt sich, dass sich BGO dem lichtstärkeren LSO Szintillator angleicht. Der Grund dafür sind die höheren Energien der prompten γ -Strahlung im Vergleich zum PET Szenario, welche die Energie-, Orts- und Zeitauflösung von BGO stark verbessern. Anhand von offensichtlichen Änderungen der Rückprojektionsbilder zeigt sich, dass mit der BBCK Verschiebungen einer punktförmigen radioaktiven Quelle erfolgreich detektiert, Linienquellen rekonstruiert und Verschiebungen der Protonenreichweite um einen Zentimeter identifiziert werden. Für die PGT-Experimente können mit einem einzigen Detektor Reichweitenunterschiede von fünf Millimetern für definierte heterogene Targets bei klinisch relevanten Dosen detektiert werden. Dies wird durch den numerischen Vergleich der Spektrumform ermöglicht. Bei größerer Ereigniszahl können Reichweitenunterschiede von bis zu zwei Millimetern detektiert werden. Die experimentellen Daten werden durch analytische Modellierung wiedergegeben.

Schlussfolgerung. Die CK und das PGT-Konzept sind ambitionierte Ansätze zur Verifizierung der Reichweite in der Protonentherapie basierend auf PGI. Intensive Detektorcharakterisierung und Tests an klinischen Einrichtungen sind Pflicht für die Entwicklung geeigneter Prototypen, da der Energiebereich prompter γ -Strahlung sich über mehrere MeV erstreckt, was nicht dem Normbereich der traditionellen medizinischen Anwendungen entspricht. Im Bezug auf die Materialauswahl der CK wird ersichtlich, dass BGO trotz der allgemeinen Überlegenheit von LSO für die Anwendung im Bereich PGI aufholt. Wegen des niedrigeren Preises, der höheren Photoabsorptionseffizienz und der nicht vorhandenen Eigenaktivität erscheint BGO als eine konkurrenzfähige Alternative für die Absorberebene der CK im Vergleich zu LSO. Die Ergebnisse der BBCK, welche mit relativ einfachen Mitteln gewonnen werden, heben die potentielle Anwendung von Compton-Kameras für die Bildgebung prompter hochenergetischer γ -Strahlen hervor. Trotzdem stellen technische Beschränkungen wie die mangelnde Anzahl von Messereignissen pro Bestrahlungspunkt (falls klinische Ströme genutzt werden) die Anwendbarkeit der CK als Echtzeit- und in vivo Reichweitenverifikationsmethode in der Protonentherapie in Frage. Die PGT-Methode ist ein alternativer Ansatz, welcher aufgrund der geringeren Kosten und der höheren Effizienz eine schnellere Umsetzung in die klinische Praxis haben könnte. Ein Protonenbunchmonitor, höherer Detektordurchsatz und eine quantitative Reichweitenrekonstruktion sind die weiteren Schritte in Richtung eines klinisch anwendbaren Prototyps, der signifikante Reichweitenunterschiede für die stärksten Bestrahlungspunkte detektieren könnte. Die experimentellen Ergebnisse unterstreichen das Potential dieser Reichweitenverifikationsmethode an einem klinischen Bleistiftstrahl und lassen diesen neuartigen Ansatz als eine vielversprechende Alternative auf dem Gebiet der in vivo Dosimetrie erscheinen.

Bibliography

- Abril I, de Vera P, Garcia-Molina R, Kyriakou I, and Emfietzoglou D. 2015. Lateral spread of dose distribution by therapeutic proton beams in liquid water. *Nucl Inst & Meth in Phys Res B*, 352:176–180. URL <http://dx.doi.org/10.1016/j.nimb.2014.11.100>.
- Albertini F, Hug EB, and Lomax AJ. 2011. Is it necessary to plan with safety margins for actively scanned proton therapy? *Phys Med Biol*, 56(14):4399. URL <http://dx.doi.org/10.1088/0031-9155/56/14/011>.
- Amaldi U and Kraft G. 2005. Radiotherapy with beams of carbon ions. *Rep Prog Phys*, 68(8):1861. URL <http://dx.doi.org/10.1088/0034-4885/68/8/R04>.
- Andreo P. 2009. On the clinical spatial resolution achievable with protons and heavier charged particle radiotherapy beams. *Phys Med Biol*, 54(11):N205. URL <http://dx.doi.org/10.1088/0031-9155/54/11/N01>.
- Assmann W, Kellnberger S, Reinhardt S, Lehrack S, Edlich A, Thirolf PG, Moser M, Dollinger G, Omar M, Ntziachristos V, and Parodi K. 2015. Ionoacoustic characterization of the proton Bragg peak with submillimeter accuracy. *Med Phys*, 42(2):567–574. URL <http://dx.doi.org/10.1118/1.4905047>.
- ASTRO. 2014. Proton beam therapy: Model Policy. URL <https://www.astro.org/protonmp>.
- Bailey D, Townsend D, Valk P, and Maisey M, eds. 2005. *Physics and Instrumentation in PET*, 13–39. Springer London. URL http://dx.doi.org/10.1007/1-84628-007-9_2.
- Balcerzyk M, Moszyński M, Kapusta M, Wolski D, Pawelke J, and Melcher C. 2000. YSO, LSO, GSO and LGSO. A study of energy resolution and nonproportionality. *IEEE Trans Nucl Sci*, 47(4):1319–1323. URL <http://dx.doi.org/10.1109/23.872971>.
- Bekelman JE and Hahn SM. 2014. Reference Pricing With Evidence Development: A Way Forward for Proton Therapy. *J Clin Oncol*, 32(15):1540–1542. URL <http://dx.doi.org/10.1200/JCO.2014.55.6613>.
- Ben Bouallègue F, Crouzet J, and Mariano-Goulart D. 2013. A heuristic statistical stopping rule for iterative reconstruction in emission tomography. *Ann Nucl Med*, 27(1):84–95. URL <http://dx.doi.org/10.1007/s12149-012-0657-5>.
- Berger M, Coursey J, Zucker M, and Chang J. 2005. ESTAR, PSTAR, and ASTAR: Computer Programs for Calculating Stopping-Power and Range Tables for Electrons, Protons, and Helium Ions. NIST. URL <http://physics.nist.gov/Star>.
- Berger M, Hubbell J, and J Chang SS, Coursey J, Sukumar R, Zucker D, and Olsen K. 2010.

Bibliography

- XCOM: Photon Cross Section Database, NIST Standard Reference Database 8 (XGAM). NIST. URL <http://www.nist.gov/pml/data/xcom>.
- Bethe H. 1930. Zur Theorie des Durchgangs schneller Korpuskularstrahlen durch Materie. *Ann Phys*, 397(3):325–400. URL <http://dx.doi.org/10.1002/andp.19303970303>.
- Biegun AK, Seravalli E, Lopes PC, Rinaldi I, Pinto M, Oxley DC, Dendooven P, Verhaegen F, Parodi K, Crespo P, and Schaart DR. 2012. Time-of-flight neutron rejection to improve prompt gamma imaging for proton range verification: a simulation study. *Phys Med Biol*, 57(20):6429. URL <http://dx.doi.org/10.1088/0031-9155/57/20/6429>.
- Brandenburg S, Ostendorf R, Hofstee M, Kiewiet H, and Beijers H. 2007. The irradiation facility at the AGOR cyclotron. *Nucl Instrum Methods Phys Res B*, 261(1–2):82–85. URL <http://dx.doi.org/10.1016/j.nimb.2007.04.304>.
- Brun R and Rademakers F. 1997. ROOT - An object oriented data analysis framework. *Nucl Instrum Methods Phys Res A*, 389(1–2):81–86. URL [http://dx.doi.org/10.1016/S0168-9002\(97\)00048-X](http://dx.doi.org/10.1016/S0168-9002(97)00048-X).
- Cambráia Lopes P, Pinto M, Simoes H, Biegun A, Dendooven P, Oxley D, Parodi K, Schaart D, and Crespo P. 2012. Optimization of collimator designs for real-time proton range verification by measuring prompt gamma rays. In *IEEE Nucl Sci Symp Conf Rec*, 3864–3870. URL <http://dx.doi.org/10.1109/NSSMIC.2012.6551886>.
- Chatziioannou A, Bao Q, and Karakatsanis N. 2008. System sensitivity in preclinical small animal imaging. In *Proc IEEE Int Symp Biomed Imaging*, 1417–1420. URL <http://dx.doi.org/10.1109/ISBI.2008.4541272>.
- Clasie B, Depauw N, Fransen M, Gomà C, Panahandeh HR, Seco J, Flanz JB, and Kooy HM. 2012. Golden beam data for proton pencil-beam scanning. *Phys Med Biol*, 57(5):1147. URL <http://dx.doi.org/10.1088/0031-9155/57/5/1147>.
- Compton AH. 1923. A Quantum Theory of the Scattering of X-rays by Light Elements. *Phys Rev*, 21(5):483–502. URL <http://dx.doi.org/10.1103/PhysRev.21.483>.
- Cree M and Bones P. 1994. Towards direct reconstruction from a gamma camera based on Compton scattering. *IEEE Trans Med Imaging*, 13(2):398–407. URL <http://dx.doi.org/10.1109/42.293932>.
- Crespo P. 2006. Optimization of in-beam Positron Emission Tomography for monitoring heavy ion tumor therapy. PhD thesis, Technische Universität Dresden. URL <http://nbn-resolving.de/urn:nbn:de:bsz:d120-qucosa-28512>.
- Cui S, Vandenbroucke A, Bieniosek M, and Levin C. 2013. General spatial distortion correction method for solid-state position sensitive detectors in PET. In *IEEE Nucl Sci Symp Conf Rec*, volume M03-6. URL <http://dx.doi.org/10.1109/NSSMIC.2013.6829029>.
- Deasy J. 1994. ICRU Report 49, Stopping Powers and Ranges for Protons and Alpha Particles. *Med Phys*, 21(5):709–710. URL <http://dx.doi.org/10.1118/1.597176>.

- Derenzo S, Weber M, Moses W, and Dujardin C. 2000. Measurements of the intrinsic rise times of common inorganic scintillators. *IEEE Trans Nucl Sci*, 47(3):860–864. URL <http://dx.doi.org/10.1109/23.856531>.
- Dorenbos P, de Haas J, and van Eijk C. 1995. Non-proportionality in the scintillation response and the energy resolution obtainable with scintillation crystals. *IEEE Trans Nucl Sci*, 42(6):2190–2202. URL <http://dx.doi.org/10.1109/23.489415>.
- Everett D, Fleming J, Todd R, and Nightingale J. 1977. Gamma-radiation imaging system based on the Compton effect. *P I Electr Eng*, 124(11):995. URL <http://dx.doi.org/10.1049/piee.1977.0203>.
- Fiedler F. 2008. Anwendung des in-beam PET Therapiemonitorings auf Präzisionsbestrahlungen mit Helium-Ionen. PhD thesis, Technische Universität Dresden. URL <http://nbn-resolving.de/urn:nbn:de:bsz:14-ds-1206441845447-47490>.
- Freeman T. 2012. Will protons gradually replace photons? *Medical Physics Web*, August(22). URL <http://medicalphysicsweb.org/cws/article/research/50584>.
- Freeman T. 2015. Proton therapy: randomized trials or model-based selection? *Medical Physics Web*, June(23). URL <http://medicalphysicsweb.org/cws/article/opinion/61592>.
- Gektin A, Shiran N, Belsky A, and Vasil'ev A. 2012. Luminescence fundamental limits for alkali halide scintillators. In *3d SUCCESS International Scientific Workshop*, 64. URL <http://www.success.kharkov.ua/events/halle/oral-gektin.pdf>.
- Gensheimer MF, Yock TI, Liebsch NJ, Sharp GC, Paganetti H, Madan N, Grant PE, and Bortfeld T. 2010. In Vivo Proton Beam Range Verification Using Spine MRI Changes. *Int J Radiat Oncol Biol Phys*, 78(1):268–275. URL <http://dx.doi.org/10.1016/j.ijrobp.2009.11.060>.
- Goitein M and Jermann M. 2003. The Relative Costs of Proton and X-ray Radiation Therapy. *Clin Oncol*, 15(1):S37–S50. URL <http://dx.doi.org/10.1053/clon.2002.0174>.
- Golnik C, Hueso González F, Müller A, Dendooven P, Enghardt W, Fiedler F, Kormoll T, Römer KE, Petzoldt J, Wagner A, and Pausch G. 2014. Range assessment in particle therapy based on prompt γ -ray timing measurements. *Phys Med Biol*, 59(18):5399. URL <http://dx.doi.org/10.1088/0031-9155/59/18/5399>.
- Grün R, Friedrich T, Krämer M, Zink K, Durante M, Engenhardt-Cabillic R, and Scholz M. 2013. Physical and biological factors determining the effective proton range. *Med Phys*, 40(11). URL <http://dx.doi.org/10.1118/1.4824321>.
- Gueth P, Dauvergne D, Freud N, Létang JM, Ray C, Testa E, and Sarrut D. 2013. Machine learning-based patient specific prompt-gamma dose monitoring in proton therapy. *Phys Med Biol*, 58(13):4563. URL <http://dx.doi.org/10.1088/0031-9155/58/13/4563>.
- Gunzert-Marx K, Schardt D, and Simon RS. 2004. Fast neutrons produced by nuclear fragmentation in treatment irradiations with ^{12}C beam. *Radiat Prot Dosimetry*, 110(1-4):595–

Bibliography

600. URL <http://dx.doi.org/10.1093/rpd/nch138>.
- Helmbrecht S. 2015. Partikeltherapie-PET – Optimierung der Datenverarbeitung für die klinische Anwendung. PhD thesis, Technische Universität Dresden. URL <http://nbn-resolving.de/urn:nbn:de:bsz:d120-qucosa-161261>.
- Henriquet P, Testa E, Chevallier M, Dauvergne D, Dedes G, Freud N, Krimmer J, Létang JM, Ray C, Richard MH, and Sauli F. 2012. Interaction vertex imaging (IVI) for carbon ion therapy monitoring: a feasibility study. *Phys Med Biol*, 57(14):4655. URL <http://dx.doi.org/10.1088/0031-9155/57/14/4655>.
- Herbach C, Gueorguiev A, Kong Y, Lentering R, Pausch G, Plettner C, and Stein J. 2009. Concept study of a two-plane Compton camera designed for location and nuclide identification of remote radiation sources. In *IEEE Nucl Sci Symp Conf Rec*, 909–911. URL <http://dx.doi.org/10.1109/NSSMIC.2009.5401560>.
- Hubbell JH and Seltzer SM. 2004. Tables of X-Ray Mass Attenuation Coefficients and Mass Energy-Absorption Coefficients from 1 keV to 20 MeV for Elements Z = 1 to 92 and 48 Additional Substances of Dosimetric Interest. NIST. URL <http://www.nist.gov/pml/data/xraycoef>.
- Hueso González F. 2012. Inter-crystal scatter in positron emission tomography: Identification techniques and effects on reconstructed images for AX-PET demonstrator. Master thesis, Universitat de València. URL <http://hdl.handle.net/10550/43308>.
- Hueso González F, Biegun AK, Dendooven P, Enghardt W, Fiedler F, Golnik C, Heidel K, Kormoll T, Petzoldt J, Römer KE, Schwengner R, Wagner A, and Pausch G. 2015a. Comparison of LSO and BGO block detectors for prompt gamma imaging in ion beam therapy. *J Instrum*, 10(9):P09015. URL <http://dx.doi.org/10.1088/1748-0221/10/09/p09015>.
- Hueso González F, Enghardt W, Fiedler F, Golnik C, Janssens G, Petzoldt J, Prieels D, Priegnitz M, Römer KE, Smeets J, Vander Stappen F, Wagner A, and Pausch G. 2015b. First test of the prompt gamma ray timing method with heterogeneous targets at a clinical proton therapy facility. *Phys Med Biol*, 60(16):6247. URL <http://dx.doi.org/10.1088/0031-9155/60/16/6247>.
- Hueso González F, Golnik C, Berthel M, Dreyer A, Enghardt W, Fiedler F, Heidel K, Kormoll T, Rohling H, Schöne S, Schwengner R, Wagner A, and Pausch G. 2014. Test of Compton camera components for prompt gamma imaging at the ELBE bremsstrahlung beam. *J Instrum*, 9(05):P05002. URL <http://dx.doi.org/10.1088/1748-0221/9/05/P05002>.
- Humm JL, Rosenfeld A, and Del Guerra A. 2003. From PET detectors to PET scanners. *Eur J Nucl Med Mol Imaging*, 30(11):1574–1597. URL <http://dx.doi.org/10.1007/s00259-003-1266-2>.
- Janssen F, Landry G, Lopes PC, Dedes G, Smeets J, Schaart DR, Parodi K, and Verhaegen F. 2014. Factors influencing the accuracy of beam range estimation in proton therapy using prompt gamma emission. *Phys Med Biol*, 59(15):4427. URL <http://dx.doi.org/10>.

- 1088/0031-9155/59/15/4427.
- Jermann M. 2015. Particle Therapy Statistics in 2014. *Int J Part Ther*, 2(1):50–54. URL <http://dx.doi.org/10.14338/IJPT-15-00013>.
- Kabuki S, Ueno K, Kurosawa S, Iwaki S, Kubo H, Miuchi K, Fujii Y, Kim D, Kim J, Kohara R, Miyazaki O, Sakae T, Shirahata T, Takayanagi T, Terunuma T, Tsukahara Y, Yamamoto E, Yasuoka K, and Tanimori T. 2009. Study on the use of electron-tracking Compton gamma-ray camera to monitor the therapeutic proton dose distribution in real time. In *IEEE Nucl Sci Symp Conf Rec*, volume J05-13, 2437–2440. URL <http://dx.doi.org/10.1109/NSSMIC.2009.5402130>.
- Kim CH, Park JH, Seo H, and Lee HR. 2012. Erratum: “Gamma electron vertex imaging and application to beam range verification in proton therapy” [*Med. Phys.*39(2), 1001–1005 (2012)]. *Med Phys*, 39(10):6523–6524. URL <http://dx.doi.org/10.1118/1.4749930>.
- Kim D, Yim H, and Kim JW. 2009. Pinhole Camera Measurements of Prompt Gamma-rays for Detection of Beam Range Variation in Proton Therapy. *J Korean Phys Soc*, 55(4):1673–1676. URL <http://dx.doi.org/10.3938/jkps.55.1673>.
- Klein O and Nishina Y. 1929. Über die Streuung von Strahlung durch freie Elektronen nach der neuen relativistischen Quantendynamik von Dirac. *Z Phys*, 52(11-12):853–868. URL <http://dx.doi.org/10.1007/BF01366453>.
- Knopf AC and Lomax A. 2013. In vivo proton range verification: a review. *Phys Med Biol*, 58(15):R131. URL <http://dx.doi.org/10.1088/0031-9155/58/15/R131>.
- Kormoll T. 2012. A Compton Camera for In-vivo Dosimetry in Ion-beam Radiotherapy. PhD thesis, Technische Universität Dresden. URL <http://nbn-resolving.de/urn:nbn:de:bsz:14-qucosa-107368>.
- Kormoll T, Fiedler F, Schöne S, Wüstemann J, Zuber K, and Enghardt W. 2011. A Compton imager for in-vivo dosimetry of proton beams - A design study. *Nucl Instrum Methods Phys Res A*, 626-627(0):114–119. URL <http://dx.doi.org/10.1016/j.nima.2010.10.031>.
- Kormoll T, Golnik C, Akhmadaliev S, Bemmerer D, Borany Jv, Fiedler F, Hueso González F, Heidel K, Kempe M, Rohling H, Schmidt K, Schone S, Wagner L, and Pausch G. 2013. Compton Imaging in a High Energetic Photon Field. In *IEEE Nucl Sci Symp Conf Rec*, volume M21-11, 1–3. URL <http://dx.doi.org/10.1109/NSSMIC.2013.6829302>.
- Kozlovsky B, Murphy RJ, and Ramaty R. 2002. Nuclear Deexcitation Gamma-Ray Lines from Accelerated Particle Interactions. *Astrophys J Suppl Ser*, 141(2):523. URL <http://dx.doi.org/10.1086/340545>.
- Kraan AC. 2015. Range verification methods in particle therapy: underlying physics and Monte Carlo modelling. *Front Oncol*, 5(150). URL <http://dx.doi.org/10.3389/fonc.2015.00150>.
- Krieger H. 1998. *Strahlenphysik, Dosimetrie und Strahlenschutz*, volume 1, 112–162.

Bibliography

- Vieweg+Teubner Verlag. URL http://dx.doi.org/10.1007/978-3-663-11534-2_4.
- Krimmer J, Ley JL, Abellan C, Cachemiche JP, Caponetto L, Chen X, Dahoumane M, Dauvergne D, Freud N, Joly B, Lambert D, Lestand L, Létang J, Magne M, Mathez H, Maxim V, Montarou G, Morel C, Pinto M, Ray C, Reithinger V, Testa E, and Zoccarato Y. 2015. Development of a Compton camera for medical applications based on silicon strip and scintillation detectors. *Nucl Instrum Methods Phys Res A*, 787:98–101. URL <http://dx.doi.org/10.1016/j.nima.2014.11.042>.
- Kurosawa S, Kubo H, Ueno K, Kabuki S, Iwaki S, Takahashi M, Taniue K, Higashi N, Miuchi K, Tanimori T, Kim D, and Kim J. 2012. Prompt gamma detection for range verification in proton therapy. *Curr Appl Phys*, 12(2):364–368. URL <http://dx.doi.org/10.1016/j.cap.2011.07.027>.
- Lee E, Polf JC, Mackin DS, Beddar S, Dolney D, Ainsley C, Kassaei A, and Avery S. 2014. Study of the Angular Dependence of a Prompt Gamma Detector Response during Proton Radiation Therapy. *Int J Part Ther*, 1(3):731–744. URL <http://dx.doi.org/10.14338/IJPT-14-00012.1>.
- Lee HR, Park JH, Kim CH, and Min CH. 2012. Design optimization of a 2D prompt-gamma measurement system for proton dose verification. *J Korean Phys Soc*, 61(2):239–242. URL <http://dx.doi.org/10.3938/jkps.61.239>.
- Llosá G, Cabello J, Callier S, Gillam J, Lacasta C, Rafecas M, Raux L, Solaz C, Stankova V, de La Taille C, Trovato M, and Barrio J. 2013. First Compton telescope prototype based on continuous LaBr₃-SiPM detectors. *Nucl Instrum Methods Phys Res A*, 718(0):130–133. URL <http://dx.doi.org/10.1016/j.nima.2012.08.074>.
- Lojacono X. 2013. Image reconstruction for Compton camera with application to hadron-therapy. PhD thesis, INSA de Lyon. URL <https://tel.archives-ouvertes.fr/tel-01081066>.
- Lu HM. 2008. A point dose method for in vivo range verification in proton therapy. *Phys Med Biol*, 53(23):N415. URL <http://dx.doi.org/10.1088/0031-9155/53/23/N01>.
- Lu HM, Mann G, and Cascio E. 2010. Investigation of an implantable dosimeter for single-point water equivalent path length verification in proton therapy. *Med Phys*, 37(11):5858–5866. URL <http://dx.doi.org/10.1118/1.3504609>.
- Mao R, Zhang L, and Zhu RY. 2011. LSO/LYSO Crystals for Future HEP Experiments. *J Phys Conf Ser*, 293(1):12004. URL <http://dx.doi.org/10.1088/1742-6596/293/1/012004>.
- Mao R, Zhang L, and Zhu RY. 2012. Crystals for the HHCAL Detector Concept. *J Phys Conf Ser*, 404(1):012029. URL <http://dx.doi.org/10.1088/1742-6596/404/1/012029>.
- Mattei I, Battistoni G, Bini F, Collamati F, Lucia ED, Durante M, Faccini R, Tessa CL, Marafini M, Piersanti L, Rovituso M, Rucinski A, Russomando A, Sarti A, Schuy C, Sciubba A, Camillocci ES, Toppi M, Traini G, Vanstalle M, Voena C, and Patera V. 2015. Prompt- γ production of 220 MeV/u ¹²C ions interacting with a PMMA target. *J Instrum*, 10(10):P10034. URL <http://dx.doi.org/10.1088/1748-0221/10/10/P10034>.

- McCleskey M, Kaye W, Mackin D, Beddar S, He Z, and Polf J. 2015. Evaluation of a multistage CdZnTe Compton camera for prompt γ imaging for proton therapy. *Nucl Instrum Methods Phys Res A*, 785(0):163–169. URL <http://dx.doi.org/10.1016/j.nima.2015.02.030>.
- Melcher CL. 2000. Scintillation crystals for PET. *J Nucl Med*, 41(6):1051–5. URL <http://www.ncbi.nlm.nih.gov/pubmed/10855634>.
- Min CH, Kim CH, Youn MY, and Kim JW. 2006. Prompt gamma measurements for locating the dose falloff region in the proton therapy. *Appl Phys Lett*, 89(18). URL <http://dx.doi.org/10.1063/1.2378561>.
- Mitin T and Zietman AL. 2014. Promise and Pitfalls of Heavy-Particle Therapy. *J Clin Oncol*, 32:2855–2863. URL <http://dx.doi.org/10.1200/JCO.2014.55.1945>.
- Moszyński M, Balcerzyk M, Czarnacki W, Kapusta M, Klamra W, Syntfeld A, and Szawlowski M. 2004. Intrinsic energy resolution and light yield nonproportionality of BGO. *IEEE Trans Nucl Sci*, 51(3):1074–1079. URL <http://dx.doi.org/10.1109/TNS.2004.829491>.
- Moszyński M, Gresset C, Vacher J, and Odru R. 1981. Timing properties of BGO scintillator. *Nucl Instrum Methods Phys Res*, 188(2):403–409. URL [http://dx.doi.org/10.1016/0029-554X\(81\)90521-8](http://dx.doi.org/10.1016/0029-554X(81)90521-8).
- Moteabbed M, España S, and Paganetti H. 2011. Monte Carlo patient study on the comparison of prompt gamma and PET imaging for range verification in proton therapy. *Phys Med Biol*, 56(4):1063. URL <http://dx.doi.org/10.1088/0031-9155/56/4/012>.
- Mumot M, Algranati C, Hartmann M, Schippers JM, Hug E, and Lomax AJ. 2010. Proton range verification using a range probe: definition of concept and initial analysis. *Phys Med Biol*, 55(16):4771. URL <http://dx.doi.org/10.1088/0031-9155/55/16/010>.
- Nagl M, Barbosa M, Vetter U, Correia J, and Hofsäss H. 2013. A new tool for the search of nuclides with properties suitable for nuclear solid state physics based on the Evaluated Nuclear Structure Data Files. *Nucl Instrum Methods Phys Res A*, 726(0):17–30. URL <http://dx.doi.org/10.1016/j.nima.2013.05.045>.
- Nassalski A, Kapusta M, Batsch T, Wolski D, Mockel D, Enghardt W, and Moszyński M. 2005. Comparative study of scintillators for PET/CT detectors. In *IEEE Nucl Sci Symp Conf Rec*, volume 5, 2823–2829. URL <http://dx.doi.org/10.1109/NSSMIC.2005.1596921>.
- Newhauser WD and Zhang R. 2015. The physics of proton therapy. *Phys Med Biol*, 60(8):R155. URL <http://dx.doi.org/10.1088/0031-9155/60/8/R155>.
- Ortega PG, Torres-Espallardo I, Cerutti F, Ferrari A, Gillam JE, Lacasta C, Llosá G, Oliver JF, Sala PR, Solevi P, and Rafecas M. 2015. Noise evaluation of Compton camera imaging for proton therapy. *Phys Med Biol*, 60(5):1845. URL <http://dx.doi.org/10.1088/0031-9155/60/5/1845>.
- Orton CG and Hendee WR, eds. 2008. *Controversies in Medical Physics: a Compendium of Point/Counterpoint Debates*, 110–123. American Association of Physicists in Medicine.

Bibliography

URL <https://www.aapm.org/pubs/books/PointCounterpointCompendium.pdf>.

Paganetti H. 2012. Range uncertainties in proton therapy and the role of Monte Carlo simulations. *Phys Med Biol*, 57(11):R99. URL <http://dx.doi.org/10.1088/0031-9155/57/11/R99>.

Paganetti H. 2014. Relative biological effectiveness (RBE) values for proton beam therapy. Variations as a function of biological endpoint, dose, and linear energy transfer. *Phys Med Biol*, 59(22):R419. URL <http://dx.doi.org/10.1088/0031-9155/59/22/R419>.

Parodi K, Enghardt W, and Haberer T. 2002. In-beam PET measurements of β^+ radioactivity induced by proton beams. *Phys Med Biol*, 47(1):21. URL <http://dx.doi.org/10.1088/0031-9155/47/1/302>.

Pausch G, Golnik C, Enghardt W, Janssens G, Prieels D, Smeets J, and Vander Stappen F. 2015. Method and apparatus for monitoring the range of a particle beam. URL <http://www.google.com/patents/US20150087882>. US Patent App. 14/491,743.

Payne S, Hunter S, Ahle L, Cherepy N, and Swanberg E. 2014. Nonproportionality of Scintillator Detectors. III. Temperature Dependence Studies. *IEEE Trans Nucl Sci*, 61(5):2771–2777. URL <http://dx.doi.org/10.1109/TNS.2014.2343572>.

PDG. 2012. Review of Particle Physics. *Phys Rev D*, 86(1):010001. URL <http://dx.doi.org/10.1103/PhysRevD.86.010001>.

Peeters A, Grutters JP, Pijls-Johannesma M, Reimoser S, Ruyscher DD, Severens JL, Joore MA, and Lambin P. 2010. How costly is particle therapy? Cost analysis of external beam radiotherapy with carbon-ions, protons and photons. *Radiother Oncol*, 95(1):45–53. URL <http://dx.doi.org/10.1016/j.radonc.2009.12.002>.

Perali I, Celani A, Bombelli L, Fiorini C, Camera F, Clementel E, Henrotin S, Janssens G, Prieels D, Roellinghoff F, Smeets J, Stichelbaut F, and Vander Stappen F. 2014. Prompt gamma imaging of proton pencil beams at clinical dose rate. *Phys Med Biol*, 59(19):5849. URL <http://dx.doi.org/10.1088/0031-9155/59/19/5849>.

Peterson SW, Robertson D, and Polf J. 2010. Optimizing a three-stage Compton camera for measuring prompt gamma rays emitted during proton radiotherapy. *Phys Med Biol*, 55(22):6841. URL <http://dx.doi.org/10.1088/0031-9155/55/22/015>.

Petzoldt J, Römer KE, Kormoll T, Berthel M, Dreyer A, Enghardt W, Fiedler F, Hueso-González F, Golnik C, Kirschke T, Wagner A, and Pausch G. 2014. Fast timing with BGO (and other scintillators) on digital silicon photomultipliers for Prompt Gamma Imaging. In *IEEE Nucl Sci Symp Conf Rec*, volume N48-4, 1–4. URL <http://dx.doi.org/10.1109/nssmic.2014.7431245>.

Pinto M, Bajard M, Brons S, Chevallier M, Dauvergne D, Dedes G, Rydt MD, Freud N, Krimmer J, Tessa CL, Létang JM, Parodi K, Pleskač R, Prieels D, Ray C, Rinaldi I, Roellinghoff F, Schardt D, Testa E, and Testa M. 2015. Absolute prompt-gamma yield measurements for ion beam therapy monitoring. *Phys Med Biol*, 60(2):565. URL <http://dx.doi.org/10.1088/0031-9155/60/2/565>.

- Pinto M, Dauvergne D, Freud N, Krimmer J, Letang JM, Ray C, Roellinghoff F, and Testa E. 2014. Design optimisation of a TOF-based collimated camera prototype for online hadrontherapy monitoring. *Phys Med Biol*, 59(24):7653. URL <http://dx.doi.org/10.1088/0031-9155/59/24/7653>.
- Polf JC, Avery S, Mackin DS, and Beddar S. 2015. Imaging of prompt gamma rays emitted during delivery of clinical proton beams with a Compton camera: feasibility studies for range verification. *Phys Med Biol*, 60(18):7085. URL <http://dx.doi.org/10.1088/0031-9155/60/18/7085>.
- Polf JC, Panthi R, Mackin DS, McCleskey M, Saastamoinen A, Roeder BT, and Beddar S. 2013. Measurement of characteristic prompt gamma rays emitted from oxygen and carbon in tissue-equivalent samples during proton beam irradiation. *Phys Med Biol*, 58(17):5821. URL <http://dx.doi.org/10.1088/0031-9155/58/17/5821>.
- Priegnitz M, Helmbrecht S, Janssens G, Perali I, Smeets J, Vander Stappen F, Sterpin E, and Fiedler F. 2015. Measurement of prompt gamma profiles in inhomogeneous targets with a knife-edge slit camera during proton irradiation. *Phys Med Biol*, 60(12):4849. URL <http://dx.doi.org/10.1088/0031-9155/60/12/4849>.
- PTCOG. 2014. Patient statistics and facilities under operation. Particle Therapy Co-Operative Group. URL <http://www.ptcog.ch>.
- Ramirez R, Wong WH, Kim S, Baghaei H, Li H, Wang Y, Zhang Y, Liu S, and Liu J. 2005. A comparison of BGO, GSO, MLS, LGSO, LYSO and LSO scintillation materials for high-spatial-resolution animal PET detectors. In *IEEE Nucl Sci Symp Conf Rec*, volume 5, 2835–2839. URL <http://dx.doi.org/10.1109/NSSMIC.2005.159692>.
- Ramirez RA, Zhang Y, Liu S, Li H, Baghaei H, An S, Wang C, Jan ML, and Wong WH. 2009. A Lower-Cost High-Resolution LYSO Detector Development for Positron Emission Mammography (PEM). *IEEE Trans Nucl Sci*, 56(5):2621–2627. URL <http://dx.doi.org/10.1109/TNS.2009.2030193>.
- Richard MH. 2012. Design study of a Compton camera for prompt- γ imaging during ion beam therapy. PhD thesis, Université Claude Bernard Lyon 1. URL <https://tel.archives-ouvertes.fr/tel-00934715>.
- Robert C, Dedes G, Battistoni G, Böhlen TT, Buvat I, Cerutti F, Chin MPW, Ferrari A, Gueth P, Kurz C, Lestand L, Mairani A, Montarou G, Nicolini R, Ortega PG, Parodi K, Prezado Y, Sala PR, Sarrut D, and Testa E. 2013. Distributions of secondary particles in proton and carbon-ion therapy: a comparison between GATE/Geant4 and FLUKA Monte Carlo codes. *Phys Med Biol*, 58(9):2879. URL <http://dx.doi.org/10.1088/0031-9155/58/9/2879>.
- Robertson D, Polf JC, Peterson SW, Gillin MT, and Beddar S. 2011. Material efficiency studies for a Compton camera designed to measure characteristic prompt gamma rays emitted during proton beam radiotherapy. *Phys Med Biol*, 56(10):3047. URL <http://dx.doi.org/10.1088/0031-9155/56/10/010>.

Bibliography

- Rohling H. 2015. Simulation studies for the in-vivo dose verification of particle therapy. PhD thesis, Technische Universität Dresden. URL <http://nbn-resolving.de/urn:nbn:de:bsz:d120-qucosa-175213>.
- Ryan C, Clayton E, Griffin W, Sie S, and Cousens D. 1988. SNIP, a statistics-sensitive background treatment for the quantitative analysis of PIXE spectra in geoscience applications. *Nucl Instrum Methods Phys Res B*, 34(3):396–402. URL [http://dx.doi.org/10.1016/0168-583X\(88\)90063-8](http://dx.doi.org/10.1016/0168-583X(88)90063-8).
- Römer KE, Pausch G, Bemmerer D, Berthel M, Dreyer A, Golnik C, Hueso González F, Kormoll T, Petzoldt J, Rohling H, Thirof P, Wagner A, Wagner L, Weinberger D, and Fiedler F. 2015. Characterization of scintillator crystals for usage as prompt gamma monitors in particle therapy. *J Instrum*, 10(10):P10033. URL <http://dx.doi.org/10.1088/1748-0221/10/10/P10033>.
- Röntgen WC. 1896. On a new kind of rays. *Science*, 3(59):227–231. URL <http://dx.doi.org/10.1126/science.3.59.227>.
- Schardt D, Elsässer T, and Schulz-Ertner D. 2010. Heavy-ion tumor therapy: Physical and radiobiological benefits. *Rev Mod Phys*, 82(1):383–425. URL <http://dx.doi.org/10.1103/RevModPhys.82.383>.
- Schumann A, Petzoldt J, Dendooven P, Enghardt W, Golnik C, Hueso González F, Kormoll T, Pausch G, Römer KE, and Fiedler F. 2015. Simulation and experimental verification of prompt gamma-ray emissions during proton irradiation. *Phys Med Biol*, 60(10):4197. URL <http://dx.doi.org/10.1088/0031-9155/60/10/4197>.
- Schutte F. 1973. On the beam control of an isochronous cyclotron. PhD thesis, Technische Hogeschool Eindhoven. URL <http://dx.doi.org/10.6100/IR108802>.
- Schwengner R, Beyer R, Dönauf F, Grosse E, Hartmann A, Junghans A, Mallion S, Rusev G, Schilling K, Schulze W, and Wagner A. 2005. The photon-scattering facility at the superconducting electron accelerator ELBE. *Nucl Instrum Methods Phys Res A*, 555(1–2):211–219. URL <http://dx.doi.org/10.1016/j.nima.2005.09.024>.
- Seo H, Park JH, Ushakov A, Kim CH, Kim JK, Lee JH, Lee CS, and Lee JS. 2011. Experimental performance of double-scattering Compton camera with anthropomorphic phantom. *J Instrum*, 6(01):C01024. URL <http://dx.doi.org/10.1088/1748-0221/6/01/C01024>.
- Seo KS, Kim CH, and Kim JW. 2006. Comparison of Titanium Hydride (TiH₂) and Paraffin as Neutron Moderator Material in a Prompt Gamma Scanning System. *J Korean Phys Soc*, 48(4):855. URL http://www.kps.or.kr/jkps/abstract_view.asp?articleid=CB6536D4-BA6B-4C17-A954-7B0A6A2566B7&globalmenu=3&localmenu=10.
- Shelyuto VA. 1989. Exact analytic results for the solid angle in systems with axial symmetry. *Z Angew Math Phys*, 40(4):608–612. URL <http://dx.doi.org/10.1007/BF00944811>.
- Shepp L and Vardi Y. 1982. Maximum Likelihood Reconstruction for Emission Tomo-

- graphy. *IEEE Trans Med Imaging*, 1(2):113–122. URL <http://dx.doi.org/10.1109/TMI.1982.4307558>.
- Shute G and Baxter A. 1966. Angular correlations for $^{12}\text{C}(p,p'\gamma)^{12}\text{C}$. *Nucl Phys*, 83(2):460–480. URL [http://dx.doi.org/10.1016/0029-5582\(66\)90584-0](http://dx.doi.org/10.1016/0029-5582(66)90584-0).
- Smeets J. 2012. Prompt gamma imaging with a slit camera for real time range control in particle therapy. PhD thesis, Université Claude Bernard Lyon 1. URL <http://theses.ulb.ac.be/ETD-db/collection/available/ULBetd-10182012-123741/unrestricted/Thesis.pdf>.
- Smeets J, Roellinghoff F, Prieels D, Stichelbaut F, Benilov A, Busca P, Fiorini C, Peloso R, Basilavecchia M, Frizzi T, Dehaes JC, and Dubus A. 2012. Prompt gamma imaging with a slit camera for real-time range control in proton therapy. *Phys Med Biol*, 57(11):3371. URL <http://dx.doi.org/10.1088/0031-9155/57/11/3371>.
- Stein J, Kreuels A, Kong Y, Lentering R, Ruhnau K, Scherwinski F, and Wolf A. 2015. Experiment and modeling of scintillation photon-counting and current measurement for PMT gain stabilization. *Nucl Instrum Methods Phys Res A*, 782(0):20–27. URL <http://dx.doi.org/10.1016/j.nima.2015.01.101>.
- Stonger K and Johnson M. 2004. Optimal calibration of PET Crystal position maps using Gaussian mixture models. *IEEE Trans Nucl Sci*, 51(1):85–90. URL <http://dx.doi.org/10.1109/TNS.2004.823334>.
- Styczynski JR. 2009. Assessment of the use of prompt gamma emission for proton therapy range verification. PhD thesis, Massachusetts Institute of Technology. URL <http://hdl.handle.net/1721.1/54468>.
- Szczesniak T, Kapusta M, Moszyński M, Grodzicka M, Szawlowski M, Wolski D, Baszak J, and Zhang N. 2013. MPPC Arrays in PET Detectors With LSO and BGO Scintillators. *IEEE Trans Nucl Sci*, 60(3):1533–1540. URL <http://dx.doi.org/10.1109/TNS.2013.2251002>.
- Testa E, Bajard M, Chevallier M, Dauvergne D, Le Foulher F, Freud N, Létang JM, Poizat JC, Ray C, and Testa M. 2008. Monitoring the Bragg peak location of 73MeV/u carbon ions by means of prompt γ -ray measurements. *Appl Phys Lett*, 93(9). URL <http://dx.doi.org/10.1063/1.2975841>.
- Testa M. 2010. Charged particle therapy, ion range verification, prompt radiation. PhD thesis, Université Claude Bernard - Lyon I. URL <https://tel.archives-ouvertes.fr/tel-00566188>.
- Testa M, Min CH, Verburg JM, Schümann J, Lu HM, and Paganetti H. 2014. Range verification of passively scattered proton beams based on prompt gamma time patterns. *Phys Med Biol*, 59(15):4181. URL <http://dx.doi.org/10.1088/0031-9155/59/15/4181>.
- Thirolf P, Lang C, Aldawood S, vd Kolff H, Maier L, Schaart D, and Parodi K. 2014. Development of a Compton Camera for Online Range Monitoring of Laser-Accelerated Proton Beams via Prompt-Gamma Detection. *EPJ Web of Conferences*, 66(11036). URL <http://dx.doi.org/10.1051/epjconf/20146611036>.

Bibliography

- Verburg JM, Riley K, Bortfeld T, and Seco J. 2013. Energy- and time-resolved detection of prompt gamma-rays for proton range verification. *Phys Med Biol*, 58(20):L37. URL <http://dx.doi.org/10.1088/0031-9155/58/20/L37>.
- Verburg JM and Seco J. 2014. Proton range verification through prompt gamma-ray spectroscopy. *Phys Med Biol*, 59(23):7089. URL <http://dx.doi.org/10.1088/0031-9155/59/23/7089>.
- Verburg JM, Shih HA, and Seco J. 2012. Simulation of prompt gamma-ray emission during proton radiotherapy. *Phys Med Biol*, 57(17):5459. URL <http://dx.doi.org/10.1088/0031-9155/57/17/5459>.
- Verburg JM, Testa M, and Seco J. 2015. Range verification of passively scattered proton beams using prompt gamma-ray detection. *Phys Med Biol*, 60(3):1019. URL <http://dx.doi.org/10.1088/0031-9155/60/3/1019>.
- Weber S, Christ D, Kurzeja M, Engels R, Kemmerling G, and Halling H. 2003. Comparison of LuYAP, LSO, and BGO as scintillators for high resolution PET detectors. *IEEE Trans Nucl Sci*, 50(5):1370–1372. URL <http://dx.doi.org/10.1109/TNS.2003.817952>.
- Wei Q, Li X, Ma T, Wang S, Dai T, Fan P, Yunhan Y, Jin Y, and Liu Y. 2013. A neighborhood standard deviation based algorithm for generating PET crystal position maps. In *IEEE Nucl Sci Symp Conf Rec*, volume M18-45. URL <http://dx.doi.org/10.1109/NSSMIC.2013.6829273>.
- Wilkinson DH. 1952. The Phoswich – A Multiple Phosphor. *Rev Sci Instrum*, 23(8):414–417. URL <http://dx.doi.org/10.1063/1.1746324>.
- Wilson RR. 1946. Radiological use of fast protons. *Radiology*, 47(5):487. URL <http://dx.doi.org/10.1148/47.5.487>.
- Yamaguchi M, Torikai K, Kawachi N, Shimada H, Satoh T, Nagao Y, Fujimaki S, Kokubun M, Watanabe S, Takahashi T, Arakawa K, Kamiya T, and Nakano T. 2012. Beam range estimation by measuring bremsstrahlung. *Phys Med Biol*, 57(10):2843. URL <http://dx.doi.org/10.1088/0031-9155/57/10/2843>.
- Yao R, Ma T, and Shao Y. 2007. Effects of LSO detector intrinsic radioactivity on SPECT imaging. In *IEEE Nucl Sci Symp Conf Rec*, volume M11-67. URL <http://dx.doi.org/10.1109/NSSMIC.2007.4437110>.
- Zhang L, Mao R, Wang S, Yang F, and Zhu RY. 2012. A study on radiation hardness of BGO crystals. In *IEEE Nucl Sci Symp Conf Rec*, 361–364. URL <http://dx.doi.org/10.1109/NSSMIC.2012.6551126>.
- Zhu RY. 2012. Fast Crystals for Forward Calorimeter Upgrade at HL-LHC. In *CMS Forward Calorimetry Taskforce Meeting*. URL http://www.hep.caltech.edu/~zhu/talks/ryz_120627_crystals.pdf.

Acknowledgement

I want to thank Prof. Dr. Wolfgang Enghardt for choosing me for the PhD position at OncoRay and the supervision of this dissertation. It has been a remarkable personal and professional experience these three years in the beautiful city of Dresden. I am grateful to Dr. Fine Fiedler for his steady confidence on me. I am indebted to Dr. Guntram Pausch for all his guidance, his great kindness, experience and his infinite teachings on nuclear experimental physics. I thank Prof. Dr. Manjit Dosanjh and the whole ENTERVISION collaboration for all training courses, conferences, meetings and discussions. It was a privilege for me to take part in this Marie Curie action.

I thank also Akhmadaliev S, Bemmerer D, Berthel M, Biegun AK, Borany Jv, Dendooven P, Dreyer A, Hartmann A, Heidel K, Helmbrecht S, Iltzsche M, Janssens G, Junghans A, Kempe M, Kormoll T, Laso-García A, Prieels D, Priegnitz M, Rohling H, Schmidt K, Schellhammer S, Schöne S, Schumann A, Schwengner R, Smeets J, Sobiella M, Vander Stappen F, Wagner A, Wagner L, and Weinberger D for the excellent assistance, corrections and scientific discussions, as well as the crews of the ELBE, AGOR, WPE and UPTD accelerators for stable operations and their support. I also acknowledge the work of the open source software community, which has made possible and easy a straightforward programming of data acquisition, analysis, image processing, and the writing of this dissertation.

I like to thank especially Christian Golnik, for being my mentor when I arrived to Germany and introducing me in the mysteries of detectors and electronics. I could not have had a better teacher. Thanks also to Johannes Petzoldt, Katja Ellen Römer and Theresa Werner for their friendliness and never-ending support, and for waiting always until Spanish lunchtime five minutes more. I do not forget my WG and all my international friends, which help to make from Dresden a new home.

This work is supported by the German Federal Ministry of Education and Research (BMBF-03Z1NN12) and by the European Commission within the Seventh Framework Program through ENTERVISION (FP7, grant agreement number 264552). Some experiments are also supported by the European Commission through ENVISION (FP7 grant agreement number 241851) and IA-ENSAR (FP7, contract N. RII3-CT-2010-262010)

*Para mis amigos,
esos pocos valientes
que sobrellevan con alegría mis defectos.*

*Para Ita e Ito,
para mi abuela Begoña y abuelo Jaime,
para mis tíos y primos,
para mis padrinos Maite y Yaco,
para mis padres Marián y José Luis,
para mis hermanos Jaime y Andrés,
para Cécile, Antoni y Charlotte,
porque de esta obra sois parte también.*

Technische Universität Dresden
Medizinische Fakultät Carl Gustav Carus
Promotionsordnung vom 24. Juli 2011

Erklärungen zur Eröffnung des Promotionsverfahrens

1. Hiermit versichere ich, dass ich die vorliegende Arbeit ohne unzulässige Hilfe Dritter und ohne Benutzung anderer als der angegebenen Hilfsmittel angefertigt habe; die aus fremden Quellen direkt oder indirekt übernommenen Gedanken sind als solche kenntlich gemacht.
2. Bei der Auswahl und Auswertung des Materials sowie bei der Herstellung des Manuskripts habe ich Unterstützungsleistungen von folgenden Personen erhalten: Prof. Dr. W. Enghardt, Dr. G. Pausch und C. Golnik.
3. Weitere Personen waren an der geistigen Herstellung der vorliegenden Arbeit nicht beteiligt. Insbesondere habe ich nicht die Hilfe eines kommerziellen Promotionsberaters in Anspruch genommen. Dritte haben von mir weder unmittelbar noch mittelbar geldwerte Leistungen für Arbeiten erhalten, die im Zusammenhang mit dem Inhalt der vorgelegten Dissertation stehen.
4. Die Arbeit wurde bisher weder im Inland noch im Ausland in gleicher oder ähnlicher Form einer anderen Prüfungsbehörde vorgelegt.
5. Die Inhalte dieser Dissertation wurden in folgender Form veröffentlicht:
 - Hueso González F, Golnik C, Berthel M, Dreyer A, Enghardt W, Fiedler F, Heidel K, Kormoll T, Rohling H, Schöne S, Schwengner R, Wagner A, and Pausch G. 2014. Test of Compton camera components for prompt gamma imaging at the ELBE bremsstrahlung beam. *J Instrum*, 9(05):P05002. URL <http://dx.doi.org/10.1088/1748-0221/9/05/P05002>
 - Hueso González F, Biegun AK, Dendooven P, Enghardt W, Fiedler F, Golnik C, Heidel K, Kormoll T, Petzoldt J, Römer KE, Schwengner R, Wagner A, and Pausch G. 2015a. Comparison of LSO and BGO block detectors for prompt gamma imaging in ion beam therapy. *J Instrum*, 10(9):P09015. URL <http://dx.doi.org/10.1088/1748-0221/10/09/p09015>
 - Hueso González F, Enghardt W, Fiedler F, Golnik C, Janssens G, Petzoldt J, Prieels D, Priegnitz M, Römer KE, Smeets J, Vander Stappen F, Wagner A, and Pausch G. 2015b. First test of the prompt gamma ray timing method with heterogeneous targets at a clinical proton therapy facility. *Phys Med Biol*, 60(16):6247. URL <http://dx.doi.org/10.1088/0031-9155/60/16/6247>

6. Ich bestätige, dass es keine zurückliegenden erfolglosen Promotionsverfahren gab.
7. Ich bestätige, dass ich die Promotionsordnung der Medizinischen Fakultät Carl Gustav Carus der Technischen Universität Dresden anerkenne.
8. Ich habe die Zitierrichtlinien für Dissertationen an der Medizinischen Fakultät der Technischen Universität Dresden zur Kenntnis genommen und befolgt.

Dresden, 9. Dezember 2015

Hiermit bestätige ich die Einhaltung der folgenden aktuellen gesetzlichen Vorgaben im Rahmen meiner Dissertation (Nicht angekreuzte Punkte sind für meine Dissertation nicht relevant.)

- das zustimmende Votum der Ethikkommission bei Klinischen Studien, epidemiologischen Untersuchungen mit Personenbezug oder Sachverhalten, die das Medizinproduktegesetz betreffen
- die Einhaltung der Bestimmungen des Tierschutzgesetzes
- die Einhaltung des Gentechnikgesetzes
- die Einhaltung von Datenschutzbestimmungen der Medizinischen Fakultät und des Universitätsklinikums Carl Gustav Carus.

Dresden, 9. Dezember 2015